DUDLEY KNOX LIBRARY
NAVAL POSTGRADUATE SCHOOL
MONTEREY CA 93943-5101

Attitude Control of an Underwater Vehicle Subjected to Waves

by

CHRISTOPHER JOHN WILLY

B. S. Systems Engineering, United States Naval Academy (1981)
Submitted in partial fulfillment of the requirements for the degrees of

OCEAN ENGINEER

at the

MASSACHUSETTS INSTITUTE OF TECHNOLOGY

and the

WOODS HOLE OCEANOGRAPHIC INSTITUTION

and

MASTER OF SCIENCE IN MECHANICAL ENGINEERING

at the

MASSACHUSETTS INSTITUTE OF TECHNOLOGY

September 1994

© 1994 Christopher J. Willy. All rights reserved.

The author hereby grants to MIT and WHOI permission to reproduce and to distribute publicly paper and electronic copies of this thesis document in whole or in part.

Thesis
W6343

DUDLEY KNOX LIBRARY
NAVAL POSTGRADUATE SCHOOL
MONTEREY CA 93943-5101

Attitude Control of an Underwater Vehicle Subjected to Waves

by

Christopher John Willy

Submitted to the Massachusetts Institute of Technology and
Woods Hole Oceanographic Institution
Joint Program in Oceanographic Engineering
in August, 1994, in partial fulfillment of the
requirements for the degrees of

OCEAN ENGINEER
and
MASTER OF SCIENCE IN MECHANICAL ENGINEERING

Abstract

This paper presents a method for estimating the spectra of water wave disturbances on five of the six axes of a stationary, slender body underwater vehicle in an inertia dominated wave force regime, both in head seas and in beam seas. Inertia dominated wave forces are typical of those encountered by a 21 inch diameter, torpedo shaped underwater vehicle operating in coastal waters and sea state 2. Strip theory is used to develop transfer function phase and magnitude between surface water waves and the slender body pitch, heave, and surge forces and moment for the vehicle in head seas, and for pitch, heave, yaw, and sway forces and moments in beam seas. Experiments are conducted which verify this method of transfer function calculation, and demonstrate the effects of vehicle forward motion in the head seas case. Using known sea spectra and linear time invariant systems theory allows for estimation of the water wave disturbance spectra for these forces and moments.

Application of sliding control techniques are then developed for the underwater vehicle longitudinal plane equations of motion. Computer simulations are used to demonstrate the dependence of underwater vehicle depth control upon the pitch control, and adaptive pitch control is shown to provide good performance in the presence of substantial parametric uncertainty. Pitch disturbance rejection properties of variations of the sliding controller are investigated. Both single frequency and stochastic disturbances are used, and the stochastic disturbance is developed using the results of the earlier investigation.

Thesis Supervisor: Dr. Dana R. Yoerger
Woods Hole Oceanographic Institution

Acknowledgements

The successful completion of this thesis was made possible through the support and encouragement of my family, friends and colleagues. Special appreciation is due

Dana Yoerger	my advisor, for his guidance, support, and unfailing encouragement during these past two years,
Michael Triantafyllou	for his frequently sought insight and advice,
Mike Hajosy	for his perceptive ideas and our continuous dialogue,
Dan Leader	for his friendship and example,
Dave Barrett	for his tremendous help and advice at the MIT tow tank,
My Parents	who have always encouraged me in my every endeavor,
My Children	Nichole, Megan, Michael and Diana, for their patience and understanding, and especially
Joan	my wife, who makes it all worthwhile.

The United States Navy is gratefully acknowledged for the graduate education opportunity provided. This research was sponsored in part by ONR Contract N00014-90-J-1912.

Table of Contents

Chapter 1 INTRODUCTION 13

1.1 Motivation 13

1.2 Research Objectives 14

1.3 Outline of Thesis 15

Chapter 2 WAVE DISTURBANCE 17

2.1 Linear Wave Results 17

2.1.1 Regular Waves 17

2.1.2 Statistical Description of Waves 19

2.2 Force Predictions 23

2.2.1 Load Regimes 23

2.2.2 Inertia Dominated Flow 26

2.2.2.1 Head Seas 26

2.2.2.2 Beam Seas 32

2.2.3 LTI Systems with Stochastic Inputs 38

Chapter 3 EXPERIMENTAL TESTING 41

3.1 Experimental Setup 41

3.1.1 Experimental Apparatus 41

3.1.2 AUV Model 43

3.2 Testing 44

3.2.1 Overview 44

3.2.2 Scaling Considerations....44
3.2.2.1 Wave Frequencies....44
3.2.2.2 AUV Speeds....46
3.2.3 Tests Conducted....48
3.3 Test Results....48
3.3.1 Raw Data....48
3.3.2 Signal Processing....51
3.3.3 Experimental Data vs. Theory....53
3.3.3.1 Stationary Model in Head Seas....53
3.3.3.2 Stationary Model in Beam Seas....61
3.3.3.3 Forward Moving Model in Head Seas....72
Chapter 4 AUV DYNAMICS....76
4.1 Equations of Motion....76
4.1.1 Coordinate Systems....76
4.1.2 Rigid Body Dynamics....80
4.1.3 Hydrodynamic Forces....82
4.1.4 Body Symmetry Considerations....85
4.2 Model Simplifications....87
Chapter 5 CONTROLLER DESIGN AND SIMULATIONS....90
5.1 Robust Sliding Control....91
5.1.1 Overview....91
5.1.2 Application to 21UUV Longitudinal Plane Equations....94
5.2 Adaptive Sliding Control....97
5.2.1 Application to 21UUV Pitch Equation....97
5.2.2 Adaptive Wave Disturbance Cancellation....99

5.3 Simulation Results 100

5.3.1 Additional Modeling Considerations 100

5.3.2 Depth Trajectory Following 103

5.3.3 Pitch Control in Regular Waves 119

5.3.4 Pitch Control in Random Waves 123

5.3.5 Summary 131

Chapter 6 CONCLUSIONS 133

6.1 Summary 133

6.2 Future Directions 136

Bibliography 137

List of Figures

Figure 1.1 21UUV Profile 14

Figure 2.1 ITTC Spectrum for Seas not Limited by Fetch 23

Figure 2.2 Load Regimes on a Vertical Cylinder 25

Figure 2.3 Body-Fixed Axis, Force and Moment Conventions for a UUV 27

Figure 2.4 Heave Force Transfer Function Magnitude for 21UUV in Head Seas....................31

Figure 2.5 Pitch Moment Transfer Function Magnitude for 21UUV in Head Seas 31

Figure 2.6 Surge Force Transfer Function Magnitude for 21UUV in Head Seas 32

Figure 2.7 Sway Force Transfer Function Magnitude for 21UUV in Beam Seas....................36

Figure 2.8 Heave Force Transfer Function Magnitude for 21UUV in Beam Seas....................36

Figure 2.9 Pitch Moment Transfer Function Magnitude for 21UUV in Beam Seas....................37

Figure 2.10 Yaw Moment Transfer Function Magnitude for 21UUV in Beam Seas 37

Figure 2.11 LTI System 38

Figure 2.12 Pitch Disturbance Spectrum for 21UUV in Head Seas....................40

Figure 2.13 Two Possible Time Realizations of Pitch Disturbance 40

Figure 3.1 Experimental Apparatus Setup....................42

Figure 3.2 21UUV Model Used in Testing 42

Figure 3.3a Sample of Surge Force and Roll Moment Raw Data....................49

Figure 3.3b Sample of Sway Force and Pitch Moment Raw Data....................50

Figure 3.3c Sample of Heave Force and Yaw Moment Raw Data....................50

Figure 3.3d Sample of Water Elevation Raw Data 51

Figure 3.4 Frequency Response of Filter 52

Figure 3.5 Two Samples of Unfiltered and Filtered Signals 53

Figure 3.6a Surge Force Transfer Function Magnitude for Shallow Model in Head Seas......55

Figure 3.6b Surge Force Transfer Function Phase for Shallow Model in Head Seas......55

Figure 3.7a Heave Force Transfer Function Magnitude for Shallow Model in Head Seas......56

Figure 3.7b Heave Force Transfer Function Phase for Shallow Model in Head Seas 56

Figure 3.8a Pitch Moment Transfer Function Magnitude for Shallow Model in Head Seas 57

Figure 3.8b Pitch Moment Transfer Function Phase for Shallow Model in Head Seas......57

Figure 3.9a Surge Force Transfer Function Magnitude for Deep Model in Head Seas......58

Figure 3.9b Surge Force Transfer Function Phase for Deep Model in Head Seas 58

Figure 3.10a Heave Force Transfer Function Magnitude for Deep Model in Head Seas 59

Figure 3.10b Heave Force Transfer Function Phase for Deep Model in Head Seas......59

Figure 3.11a Pitch Moment Transfer Function Magnitude for Deep Model in Head Seas 60

Figure 3.11b Pitch Moment Transfer Function Phase for Deep Model in Head Seas 60

Figure 3.12a Sway Force Transfer Function Magnitude for Shallow Model in Beam Seas 62

Figure 3.12b Sway Force Transfer Function Phase for Shallow Model in Beam Seas......62

Figure 3.13a Heave Force Transfer Function Magnitude for Shallow Model in Beam Seas 63

Figure 3.13b Heave Force Transfer Function Phase for Shallow Model in Beam Seas 63

Figure 3.14a Roll Moment Transfer Function Magnitude for Shallow Model in Beam Seas 64

Figure 3.14b Roll Moment Transfer Function Phase for Shallow Model in Beam Seas......64

Figure 3.15a Pitch Moment Transfer Function Magnitude for Shallow Model in Beam Seas 65

Figure 3.15b Pitch Moment Transfer Function Phase for Shallow Model in Beam Seas 65

Figure 3.16a Yaw Moment Transfer Function Magnitude for Shallow Model in Beam Seas 66

Figure 3.16b Yaw Moment Transfer Function Phase for Shallow Model in Beam Seas 66

Figure 3.17a Sway Force Transfer Function Magnitude for Deep Model in Beam Seas 67

Figure 3.17b Sway Force Transfer Function Phase for Deep Model in Beam Seas 67

Figure 3.18a Heave Force Transfer Function Magnitude for Deep Model in Beam Seas 68

Figure 3.18b Heave Force Transfer Function Phase for Deep Model in Beam Seas 68

Figure 3.19a Roll Moment Transfer Function Magnitude for Deep Model in Beam Seas 69

Figure 3.19b Roll Moment Transfer Function Phase for Deep Model in Beam Seas 69

Figure 3.20a Pitch Moment Transfer Function Magnitude for Deep Model in Beam Seas 70

Figure 3.20b Pitch Moment Transfer Function Phase for Deep Model in Beam Seas 70

Figure 3.21a Yaw Moment Transfer Function Magnitude for Deep Model in Beam Seas 71

Figure 3.21b Yaw Moment Transfer Function Phase for Deep Model in Beam Seas 71

Figure 3.22 Surge Force Transfer Function Magnitude for Model at 0.489 m/s in Head Seas 73

Figure 3.23 Heave Force Transfer Function Magnitude for Model at 0.489 m/s in Head Seas 73

Figure 3.24 Pitch Moment Transfer Function Magnitude for Model at 0.489 m/s in Head Seas 74

Figure 3.25 Surge Force Transfer Function Magnitude for Model at 0.733 m/s in Head Seas 74

Figure 3.26 Heave Force Transfer Function Magnitude for Model at 0.733 m/s in Head Seas 75
Figure 3.27 Pitch Moment Transfer Function Magnitude for Model at 0.733 m/s in Head Seas 75
Figure 4.1 The Euler Angles 77
Figure 5.1 Sternplane and Thruster Dynamics Model 101
Figure 5.2 21UUV Depth Trajectory with Robust Sliding Pitch Controller 105
Figure 5.3 21UUV Pitch Response During Depth Maneuver 106
Figure 5.4 21UUV Speed Response During Depth Maneuver 107
Figure 5.5 Robust Sliding Pitch Controller $k_{\theta eff}(t)$. 108
Figure 5.6 21UUV Depth Trajectory with Adaptive Sliding Pitch Control Law, $\Gamma = \mathbf{0}$ 109
Figure 5.7 21UUV Pitch Response with Adaptive Sliding Pitch Control Law, $\Gamma = \mathbf{0}$ 110
Figure 5.8 21UUV Depth Trajectory with Adaptive Sliding Pitch Control Law, $\Gamma = \Gamma_0$ 111
Figure 5.9 21UUV Pitch Response with Adaptive Sliding Pitch Control Law, $\Gamma = \Gamma_0$ 112
Figure 5.10 Adaptation of $\hat{\mathbf{a}}$ and s_θ with Φ_θ 113
Figure 5.11 21UUV Depth Trajectory with Adaptive Sliding Pitch Control Law, $\Gamma = \mathbf{0}$ 114
Figure 5.12 21UUV Pitch Response with Adaptive Sliding Pitch Control Law, $\Gamma = \mathbf{0}$ 115
Figure 5.13 21UUV Depth Trajectory with Adaptive Sliding Pitch Control Law, $\Gamma = \Gamma_0$ 116
Figure 5.14 21UUV Pitch Response with Adaptive Sliding Pitch Control Law, $\Gamma = \Gamma_0$ 117
Figure 5.15 Adaptation of $\hat{\mathbf{a}}$ and s_θ with Φ_θ 118
Figure 5.16 Adaptive Pitch Control Law with Single Frequency Disturbance, $\Gamma = \mathbf{0}$ 120
Figure 5.17 Adaptive Sliding Pitch Controller with Single Frequency Disturbance 121
Figure 5.18 Adaptation to a Single Frequency Disturbance by the Pitch Controller 122
Figure 5.19 Wave Disturbance Spectra 124
Figure 5.20 Possible Time Realizations for Pitch, Heave, and Surge Disturbance 125

Figure 5.21 Adaptive Sliding Pitch Control with Stochastic Disturbance 126

Figure 5.22 Adaptive Sliding Pitch Control with Stochastic Disturbance 127

Figure 5.23 Adaptive Sliding Pitch Control with Stochastic Disturbance 129

Figure 5.24 Adaptive Sliding Pitch Control with Stochastic Disturbance. 130

List of Tables

Table 3.1 Frequencies and Wavelengths Investigated During Testing..47

Table 3.2 Tow Speeds Investigated During Testing..47

Table 3.3 Summary of Tests Conducted...48

Table 4.1. SNAME Notation Used for Ocean Vehicles...79

Table 5.1 Nominal Body, Hydrodynamic, Controller and Actuator Parameters........................102

Chapter 1 INTRODUCTION

1.1 Motivation

Autonomous Underwater Vehicles (AUVs) have become increasingly useful tools in the exploration of the ocean depths, where the effects of surface waves are far removed from the operating region of the vehicle. As the range of missions for AUVs expands, so does the need to understand the disturbances which the vehicle will encounter in its enlarged theater of operation. While deep underwater, ocean currents may be the source of the predominant disturbance to the untethered AUV, the effect of gravity water waves becomes important when operating an AUV near the water's surface.

The Naval Undersea Warfare Center (NUWC) Division, Newport, Rhode Island, is currently developing an autonomous, 21 inch diameter "torpedo shaped" AUV, known as the 21UUV, for which near surface operations is envisioned in the future. The 21UUV shape, in the expected 301 inch long version, is shown in figure 1.1.

The Deep Submergence Laboratory at the Woods Hole Oceanographic Institution is involved in the research and development of the control algorithms for the vehicle, and an understanding of the expected environmental disturbances to the AUV will allow a more thorough evaluation of the effectiveness of the developed controllers. Also, future decisions concerning possible operating regions of the 21UUV must account for water surface conditions and the effect of waves when near surface missions are considered.

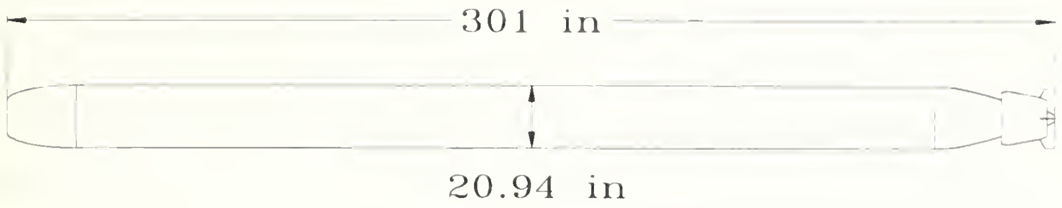

Figure 1.1 21UUV Profile

1.2 Research Objectives

In severe sea conditions, the destabilizing effect of surface waves on an AUV is expected to be the limiting factor when considering the upper boundary of useful operating depths available to the underwater vehicle. For example, with surface waves in deep water, one would expect the amplitude of water motion, and hence the effect of wave forces, to decay with increasing depth. Because there is a limit in its ability to stabilize itself, an AUV would have a ceiling to its effective operating regime. Therefore, one reasonable measure of an AUV controller is its performance in the presence of wave disturbances.

Before the disturbance rejection properties of any controller can be evaluated, the properties of the disturbance must be determined. Because the 21UUV shape is relatively simple, existing literature concerning the hydrodynamic forces on similar shaped bodies, i.e. cylinders, is abundant. Therefore the first objective of this thesis is to apply existing theory to develop a model for predicting the forces and moments caused by sea waves on a stationary, slender body AUV. Linear wave theory, hydrodynamic strip theory accounting for the precise contour of the 21UUV, and the stochastic description of the sea surface are to be used.

With any model, simplifications of the true physical processes result in model inaccuracies. While full scale testing of the yet to be built 21UUV is beyond the scope of this thesis, scale model testing in a wave tank is possible. Therefore, the second research objective is to conduct tests which either confirm the validity of the wave force and moment model, or provide empirical data which allows for the estimation of the hydrodynamic forces and moments on the AUV.

While a precursor of the 21UUV is currently undergoing sea trials which, in part, are being used to evaluate controller performance in still water and in steady currents, the testing of this vehicle in other than calm sea conditions is a future prospect. Hence, the third research objective is to develop a controller for the 21UUV using the same methodology as is expected to be used for the actual 21UUV controller, and by simulation, to evaluate the controller's performance in the presence of wave disturbances similar to that which might be encountered in practice. For simplification purposes, motion in the AUV's longitudinal plane alone is considered.

1.3 Outline of Thesis

Chapter 2 develops theory allowing for the estimation of wave disturbances on a stationary slender body AUV beneath the water's surface. Slender body strip theory and linear wave theory are used to develop a method for calculating the transfer function phase and magnitude between surface water waves and five of the six forces and moments expected for the submerged AUV, both in head and in beam seas. A spectral description of random water waves is presented, and using linear time invariant systems theory, a method for calculating the spectra of the wave disturbance is shown. Generating a time simulation of waves from their spectral representation is addressed.

Chapter 3 contains a description of the experimental testing performed on a scale model of the 21UUV to evaluate the transfer function representation of wave forces and moments presented in chapter 2. The experimental apparatus is detailed, as are the series of tests performed. Experimental data is compared to theoretical values and largely verifies the earlier developed theory. The effect on transfer function magnitude of vehicle forward motion in head seas is also investigated. Differences and similarities between the static and dynamic model cases are noted.

Chapter 4 details the general six degree of freedom equations of motion for an underwater vehicle. Model simplifications are made accounting for 21UUV body symmetry and assumptions concerning maintenance of the vehicle roll angle at 0 degrees. The resulting longitudinal plane equations used for subsequent discussion are presented.

Chapter 5 provides a method of applying sliding control techniques to the 21UUV in the longitudinal plane. Variations of the sliding controller are applied to the vehicle pitch axis, and are demonstrated in simulation as an integrated part of the pitch-depth-speed controller. Pitch disturbance rejection properties of the controllers is investigated through time simulations, and extensions to an adaptive sliding controller are made in an attempt to improve disturbance rejection properties.

Chapter 6 summarizes the results of the thesis and describes the direction of future research.

Chapter 2 WAVE DISTURBANCE

The results of linear wave theory provide a first order approximation to the motion of a body of water due to surface gravity waves. Some results from the theory are presented here, and then are used to develop a model of the stochastic disturbance which could be expected to affect an AUV operating near the surface of the ocean, where the wave effects are most prominent. This wave disturbance model will be compared to experimental results in a later chapter, and then used in AUV dynamic simulations, where the goal will be to reduce the effect of wave disturbances through the use of different control schemes.

2.1 Linear Wave Results

A more thorough discussion of these results can be found in (Newman 1977), or (Faltinsen 1990).

2.1.1 Regular Waves

For a single frequency water wave traveling in the direction measured by the angle α with respect to the Cartesian coordinate frame positive x direction, the free surface elevation above the mean free surface can be described by

$$\zeta = \zeta_a \sin(\omega t - kx\cos\alpha - ky\sin\alpha) \tag{2.1}$$

where ζ_a represents the surface wave amplitude (half the wave height), $\omega = \frac{2\pi}{T}$ is the circular frequency, T is the wave period, t is time, $k = \frac{2\pi}{\lambda}$ is the wave number, and λ is wavelength. Wave number, k, is related to circular frequency, ω, through the dispersion relation

$$\frac{\omega^2}{g} = k \tanh kh \tag{2.2}$$

where g is the acceleration of gravity, and h is the water depth (from mean free surface to ocean floor).

For a wave traveling from one water depth to another, ω remains constant, and the wave number, and therefore the wavelength are affected by the change in h.

Assuming from here on that $\alpha = 0$, a water particle's vertical motion, of amplitude ζ_a on the surface, decays with depth, z, where z is taken positive down, and is described by

$$\zeta = \zeta_a \frac{\sinh k(-z+h)}{\sinh kh} \sin(\omega t - kx) \tag{2.3}$$

while the water particle's horizontal motion is

$$\xi = -\zeta_a \frac{\cosh k(-z+h)}{\sinh kh} \cos(\omega t - kx) \tag{2.4}$$

The vertical velocity and acceleration fields are

$$w = \omega \zeta_a \frac{\sinh k(-z+h)}{\sinh kh} \cos(\omega t - kx) \tag{2.5}$$

$$a_3 = -\omega^2 \zeta_a \frac{\sinh k(-z+h)}{\sinh kh} \sin(\omega t - kx) \tag{2.6}$$

and the horizontal velocity and acceleration fields are

$$u = \omega \zeta_a \frac{\cosh k(-z+h)}{\sinh kh} \sin(\omega t - kx) \qquad (2.7)$$

$$a_1 = \omega^2 \zeta_a \frac{\cosh k(-z+h)}{\sinh kh} \cos(\omega t - kx) \qquad (2.8)$$

The dynamic pressure field in the water column is

$$p_D = \rho g \zeta_a \frac{\cosh k(-z+h)}{\cosh kh} \sin(\omega t - kx) \qquad (2.9)$$

where ρ is the water density and g is the acceleration of gravity.

2.1.2 Statistical Description of Waves

In practice, linear wave theory is used to simulate irregular seas by the superposition of a large number of regular waves (Faltinsen 1990). For a long crested, irregular sea with waves traveling in the positive x-direction, the sea surface elevation can be described

$$\zeta = \sum_{j=1}^{N} A_j \sin(\omega_j t - k_j x + \varepsilon_j) \qquad (2.10)$$

where A_j, ω_j, k_j, and ε_j are the wave amplitude, circular frequency, wave number, and random phase of the j-th wave component respectively, and N is the number of wave components used in the simulation. The random phase angles are uniformly distributed between 0 and 2π radians, and the wave number and circular frequency are related through the dispersion relation. Wave amplitude is related to the circular frequency through a single-sided wave amplitude spectrum, $S^+(\omega)$, and can be calculated from

$$A_j^2 = 2S^+(\omega_j)\Delta\omega \qquad (2.11)$$

Here, $\Delta\omega$ is the increment in ω used in the discrete approximation of the spectrum $S^{+}(\omega)$. In implementing equation (2.10), ω_j is chosen randomly and uniformly in the interval ω_i to $\omega_i + \Delta\omega = \omega_{i+1}$ to avoid the repetition of the expression after $2\pi/\Delta\omega$ seconds. It follows that the horizontal velocity and acceleration fields, and the vertical velocity and acceleration fields can be simulated in the same manner, as

$$u = \sum_{j=1}^{N} \omega_j A_j \frac{\cosh k_j(-z+h)}{\sinh k_j h} \sin(\omega_j t - k_j x + \varepsilon_j) \tag{2.12}$$

$$a_1 = \sum_{j=1}^{N} \omega_j^2 A_j \frac{\cosh k_j(-z+h)}{\sinh k_j h} \cos(\omega_j t - k_j x + \varepsilon_j) \tag{2.13}$$

$$w = \sum_{j=1}^{N} \omega_j A_j \frac{\sinh k_j(-z+h)}{\sinh k_j h} \cos(\omega_j t - k_j x + \varepsilon_j) \tag{2.14}$$

$$a_3 = \sum_{j=1}^{N} -\omega_j^2 A_j \frac{\sinh k_j(-z+h)}{\sinh k_j h} \sin(\omega_j t - k_j x + \varepsilon_j) \tag{2.15}$$

respectively, and that the dynamic pressure can be simulated by

$$p_D = \rho g \sum_{j=1}^{N} A_j \frac{\cosh k_j(-z+h)}{\cosh k_j h} \sin(\omega_j t - k_j x + \varepsilon_j) \tag{2.16}$$

The single-sided spectrum $S^{+}(\omega)$ is commonly used in Ocean Engineering applications, and is defined

$$S^{+}(\omega) = \begin{cases} \frac{1}{\pi} \int_{-\infty}^{\infty} \Psi_{\zeta\zeta}(\tau) e^{-j\omega\tau} d\tau & \omega \geq 0 \\ 0 & \omega < 0 \end{cases} \tag{2.17}$$

where

$$\begin{aligned}\Psi_{\zeta\zeta}(\tau) &= \lim_{T\to\infty}\frac{1}{2T}\int_{-T}^{T}\zeta(t)\,\zeta(t+\tau)\,dt \\ &= E\{\zeta(t)\,\zeta(t+\tau)\}\end{aligned} \tag{2.18}$$

is the sea surface elevation autocorrelation function. It can be recognized that $S^{+}(\omega)$ is related to the familiar definition of the power spectrum, $\Phi_{\zeta\zeta}(\omega)$ (the Fourier transform of the autocorrelation function) as

$$S^{+}(\omega) = \begin{cases}\frac{1}{\pi}\Phi_{\zeta\zeta}(\omega) & \omega \geq 0 \\ 0 & \omega < 0\end{cases} \tag{2.19}$$

$S^{+}(\omega)$ can be calculated in the method described above, that is, by first calculating the autocorrelation function of a set of wave data and then computing its Fourier transform. The assumption made is that sea waves can be described as a stationary random process over some short period of time on the order of a few hours. By curve fitting some function of frequency to the resulting empirical data, many oceanographers have compactly described the frequency content of their data by an empirical formula representing a continuous wave spectrum (St. Denis 1969).

The forms of the function used to curve fit wave record data to describe a spectrum are various. Bretschneider is credited with proposing the first easily usable two parameter spectrum representing seaways in all states of development (Chryssostomidis 1974). The 15th International Towing Tank Conference (ITTC) recommended a spectrum of the Bretschneider form as the standard international spectrum when information concerning typical sea spectra for

a specific region of the seas is not available. For seas not limited by fetch, the ITTC recommended Bretschneider spectrum has the form

$$S^{+}(\omega)=\frac{173\,H_{\frac{1}{3}}^{2}}{T_1^{4}\,\omega^{5}}\exp\left(\frac{-691}{T_1^{4}\,\omega^{4}}\right) \tag{2.20}$$

Here, T_1 is the average wave period, and $H_{\frac{1}{3}}$ is the significant wave height, defined as the average of the highest one third of all the waves (15th ITTC 1978).

The term "sea state" is commonly used to describe sea surface conditions ranging from glassy seas (sea state 0) to those encountered during hurricane conditions (sea state 9). Using data published in (Berteaux 1991) relating sea states to the two parameters above, the ITTC recommended spectrum for conditions spanning sea states 1 through 3 is depicted in figure 2.1. It can be seen that as the sea state becomes rougher, the spectrum becomes more peaked, and the modal frequency decreases. Also, the majority of the spectrum power is seen to be in frequencies below 3 rad/sec, even for the calmest of seas.

The ITTC recommended spectrum will be selected as the sample wave spectrum in all following discussion and simulations. While this spectrum may not be the best available model of the actual wave spectrum for a specific application, it is assumed to be sufficiently representative of the developed model wave spectra for the purpose of this discussion.

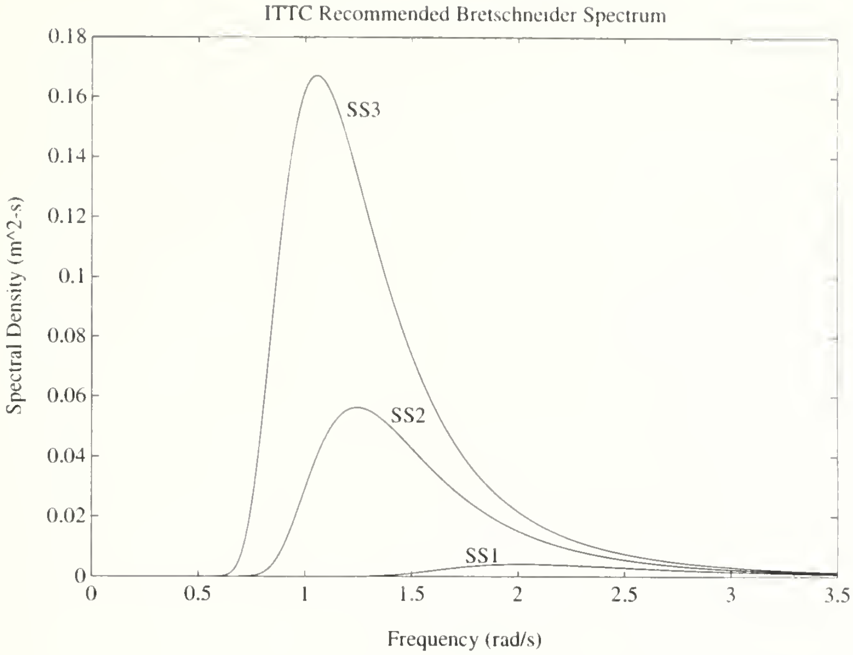

Figure 2.1 ITTC Spectrum for Seas not Limited by Fetch
and Conditions Ranging from Sea States 1 to 3

2.2 Force Predictions

2.2.1 Load Regimes

Morison was the first to propose that the horizontal force per unit length on a stationary vertical cylinder in waves can be written as

$$dF = \left(\rho\pi\tfrac{D^2}{4}C_M a_1 + \rho\tfrac{D}{2}C_D u\left|u\right|\right)dl \tag{2.21}$$

where ρ is the water density, D is the cylinder diameter, l is the cylinder length, a_1 and u are the horizontal acceleration and velocity of the water at the depth of the cylinder section, and C_M and C_D are coefficients which can be determined experimentally (Morison, et al 1950). It is seen that this formulation represents two types of forces on a submerged cylinder, the first term

representing an inertial force proportional to the acceleration of the water at the depth of interest, and a second, nonlinear drag term proportional to sign velocity times square velocity of the water at the depth of interest. In practice, C_M and C_D are dependent on several parameters such as the Reynolds and Keulegan Carpenter numbers of the flow, and the surface roughness of the cylinder.

It is therefore possible that in a particular type of flow that either the inertia or drag force is predominant. Such is the case for vertical pilings penetrating the water's surface, and it is known that the ratios of wavelength and waveheight to cylinder diameter are key parameters in predicting the load regime of the waves on the cylinder (Faltinsen 1990). Figure 2.2 depicts these load regimes.

For a stationary object in a simple harmonic oscillating flow, the time varying total force can then be expressed as

$$F_T = F_D \sin\omega t \left|\sin\omega t\right| + F_I \cos\omega t \tag{2.22}$$

where F_D and F_I represent the maxima of the drag and inertia force components, respectively. It can be shown that (Dean and Dalrymple 1984)

$$\left|F_T\right| = \begin{cases} F_I & 2F_D \le F_I \\ F_D + \dfrac{F_I^2}{4F_D} & 2F_D > F_I \end{cases} \tag{2.23}$$

The significance of equation (2.23) is that the maximum force on the body is not affected by additional drag force until the amplitude of the drag is at least one half that of the inertia force. For harmonic oscillating flows, such as that caused by regular waves, while even small amounts of drag may be important when considering the shape of the load function on a

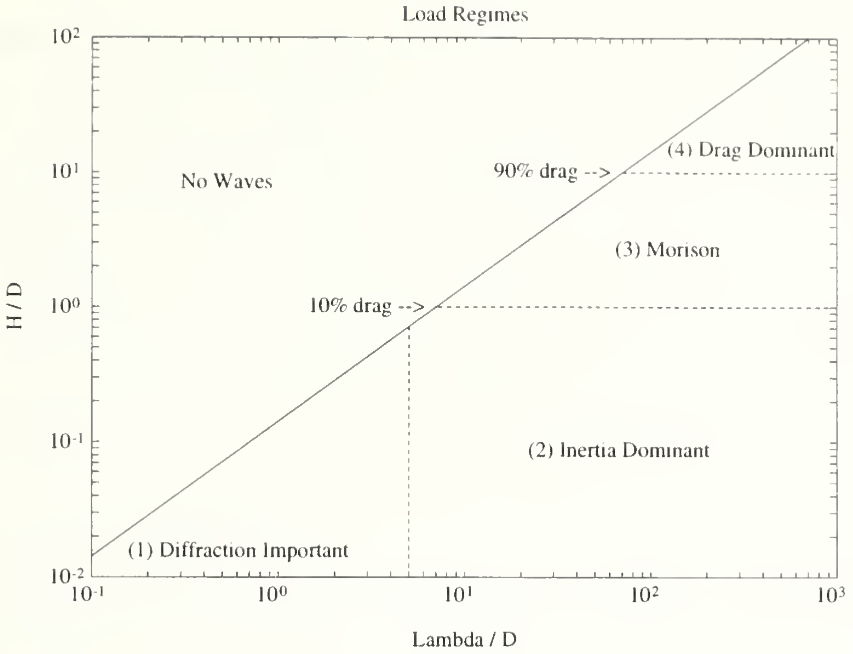

Figure 2.2 Load Regimes on a Vertical Cylinder
(Adapted from (Faltinsen 1990))

stationary body, the peak amplitude of the force is only affected when the drag component is greater than one half the inertia force. This implies that if the peak of the regular wave force is the main concern for a particular submerged body, considering figure 2.2, water particle motion with amplitude greater than 0.5 diameters, and perhaps up to 2.5 diameters would produce a peak force only as high as the peak force due to the inertia term from equation (2.22).

The same concepts discussed above will be used to predict the predominant forces on a stationary horizontal cylindrical body (the 21UUV) under waves. When waves cause the motion of a water particle at an AUV's depth to be of the order of one UUV diameter or less, it is expected that the predominant hydrodynamic force on the UUV due to the wave disturbance would be inertial in nature. Because an AUV may be deeply submerged, it is not the surface wave height to AUV diameter ratio which is of concern, but more appropriately twice the amplitude of water particle horizontal or vertical motion at the vehicle depth (which is analogous

to wave height) compared to the cylinder diameter. For instance, if yaw moment on the body is of concern, horizontal water motion tangent to the longitudinal (x) axis of the AUV should be considered as this is the flow which causes the yaw moment.

While the above analogy is approximate in nature, it provides a means to predict which hydrodynamic forces may be of concern when predicting the total load on a cylindrical AUV caused by waves. Experimental data will be presented in a later chapter which tests the validity of these arguments.

2.2.2 Inertia Dominated Flow

Figure 2.3 depicts the axes, force and moment conventions for an AUV used in this and subsequent discussions. The body-fixed axes are labeled x, y, and z, with forces X, Y, and Z positive in the corresponding positive axis direction, and moments K, M, and N are positive using the right hand rule.

For the long, streamlined body of the 21UUV, strip theory can be used to calculate the hydrodynamic forces and moments imposed on the stationary body by water flow perpendicular to the longitudinal axis of the body. Considered below are two body-to-wave orientations, both for the horizontal vehicle in an inertia dominated wave force regime. Strip theory is first applied to estimate the heave force, Z, the pitch moment, M, and the surge force, X, on the vehicle in direct head seas, where wave propagation is perpendicular to the AUV longitudinal axis. Then Y (sway force), Z, M, and N (yaw moment) are estimated for the vehicle in direct beam seas, i.e., when wave propagation is parallel to the vehicle longitudinal axis.

2.2.2.1 Head Seas

To better understand what to expect for Z and M on the AUV body under head seas, first considered is a right cylinder of constant diameter equal to the maximum diameter of the 21UUV,

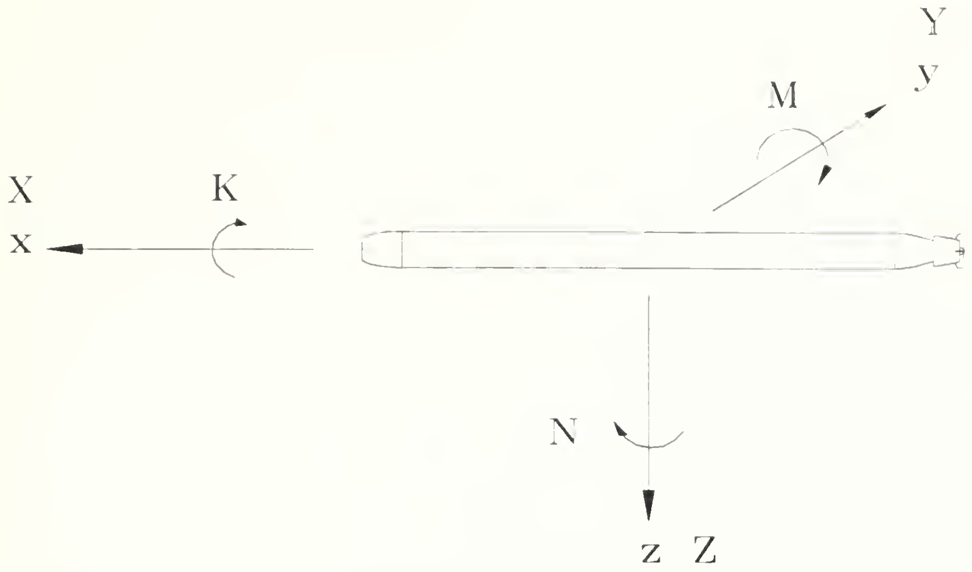

Figure 2.3 Body-Fixed Axis, Force and Moment Conventions for a UUV

and of the same length as the vehicle. Considering the nearly cylindrical shape of the 21UUV, this cylinder model allows for a closed-form solution which roughly approximates the more refined solution developed later using numerical methods and taking into account the precise body contour of the AUV.

The vertical force (positive downward) on a stationary horizontal cylinder of length L under waves traveling in the negative x direction in an inertia dominated force regime is calculated here using strip theory as

$$Z_H(t) = -\int_L K_{M3} a_3(x, z, t)\, dx \tag{2.24}$$

where $K_{M3} = \frac{1}{4}\pi\rho D^2 C_M$. To determine C_M, the Keulegan-Carpenter parameter is considered and is found for vertical water motion as

$$KC_v = w_m T / D \tag{2.25}$$

where

$$w_m = \omega\zeta_a \tfrac{\sinh k(-z+h)}{\sinh kh} \tag{2.26}$$

is the amplitude of the vertical velocity from equation (2.5), and T is the period of the harmonic wave. It is seen that

$$KC_v = 2\pi\zeta_m / D \tag{2.27}$$

where ζ_m is the maximum vertical displacement of the water particle from its neutral position. It is the assumption here that ζ_m/D, the "displacement" parameter, is 1 or less and that the resultant hydrodynamic force is inertia dominated with $C_M \cong 2$ (Dean and Dalrymple 1984).

Returning to equation (2.24), vertical water particle acceleration is taken at the centerline depth of the cylinder. Using linear wave theory and recalling that the wave is now traveling in the negative x direction, $a_3(x, z, t)$ taken from equation (2.6) can be expressed

$$a_3(x, z, t) = A_3(z)\sin(kx + \omega t) \tag{2.28}$$

Then, recalling that the force Z is taken positive down while the wave elevation is taken positive up,

$$\begin{aligned} Z_H(t) &= -K_{M3}A_3 \int_{-L/2}^{L/2} \sin(kx + \omega t)dx \\ &= -K_{M3}A_3 \tfrac{2}{k} \sin\tfrac{kL}{2} \sin(\omega t) \end{aligned} \tag{2.29}$$

and

$$|Z_H| = \left|K_{M3}A_3 \tfrac{2}{k} \sin\tfrac{kL}{2}\right| \tag{2.30}$$

Similarly, M about the mid-length position on the same stationary horizontal cylinder under the same waves is calculated using strip theory as

$$\begin{aligned} M_H(t) &= K_{M3}A_3 \int_{-L/2}^{L/2} x\sin(kx+\omega t)dx \\ &= \tfrac{K_{M3}A_3}{k^2}(2\sin\tfrac{kL}{2} - kL\cos\tfrac{kL}{2})\cos\omega t \end{aligned} \tag{2.31}$$

and

$$\left|M_H\right| = \left|\tfrac{K_{M3}A_3}{k^2}(2\sin\tfrac{kL}{2} - kL\cos\tfrac{kL}{2})\right| \tag{2.32}$$

The surge force, X, can be estimated by calculating the difference in force between the back and front ends of the cylinder due to the difference in the undisturbed dynamic pressure:

$$\begin{aligned} X_H(t) &= -\tfrac{1}{2}\pi\rho g D^2 \zeta_a \tfrac{\cosh k(-z+h)}{\cosh kh} \sin\tfrac{kL}{2}\cos(\omega t) \\ \left|X_H\right| &= \left|\tfrac{1}{2}\pi\rho g D^2 \zeta_a \tfrac{\cosh k(-z+h)}{\cosh kh} \sin\tfrac{kL}{2}\right| \end{aligned} \tag{2.33}$$

For a given AUV depth in the water column, the above formulation relates wave number, k, to the magnitude of Z, M, and X for unit amplitude surface waves. Since wave frequency is directly related to wave number by the dispersion relation (equation (2.2)), equations (2.29), (2.31), and (2.33) can be used to solve for the magnitude and phase of the transfer function from ζ_a to Z, M, and X.

For a more refined estimate of Z, M and X, the cylinder model of the 21UUV is abandoned and the precise body contour of the AUV is accounted for. Then, from equation (2.24),

$$Z_H(t) = -A_3 \int_{-L/2}^{L/2} K_{M3}(x)\sin(kx+\omega t)dx \tag{2.34}$$

where $K_{M3}(x)=\frac{1}{4}\rho\pi C_M D^2(x)$. $C_M \cong 2$ and constant is still assumed, and using numerical methods with a look-up table for *D(x)*, the amplitude of Z_H can be found for all ω and arbitrary phase. Similarly,

$$M_H(t)=A_3\int_{-L/2}^{L/2} x\,K_{M3}(x)\sin(kx+\omega t)dx \tag{2.35}$$

where the same method can be used to find the amplitude for M_H for all ω and arbitrary phase. Calculating X requires the integration of the dynamic pressure over the vehicle contour at both ends, namely

$$X_H(t)=2\pi\int_0^R p_D(x_{tail}(r))r\,dr-2\pi\int_0^R p_D(x_{nose}(r))r\,dr \tag{2.36}$$

As examples of the calculated transfer function magnitudes, figures 2.4, 2.5, and 2.6 compare predicted $|Z_H(\omega)|/|\zeta_a(\omega)|$, $|M_H(\omega)|/|\zeta_a(\omega)|$ and $|X_H(\omega)|/|\zeta_a(\omega)|$ for the 21UUV in head seas, 30 meter deep water and at various depths using the two methods described above.

Figures 2.4, 2.5, and 2.6 show decreased transfer function magnitudes with increased depth of the cylinder, as would be expected due to the decay of water motion with depth. Also observed in these figures is a shift of the peak of the magnitude of the transfer functions to lower frequencies with increased depth of the vehicle. This can be explained by realizing that higher frequency waves decay more rapidly with increasing depth in the water column than do lower frequency waves.

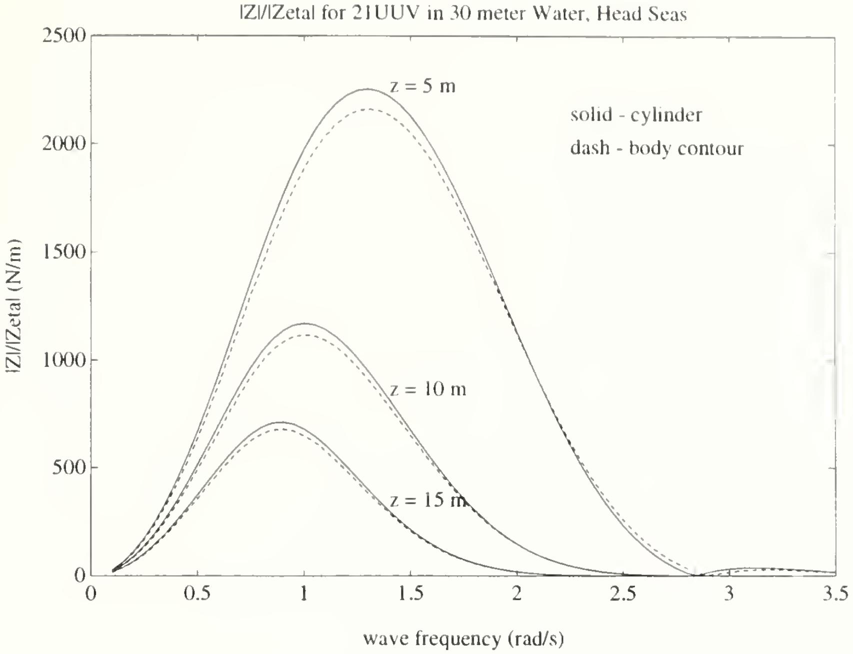

Figure 2.4 Heave Force Transfer Function Magnitude for 21UUV in Head Seas

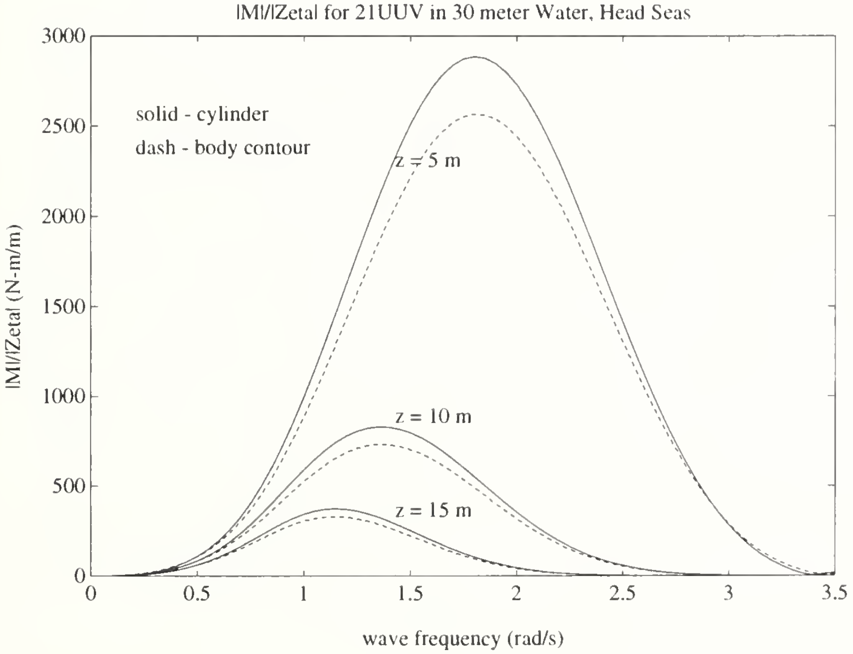

Figure 2.5 Pitch Moment Transfer Function Magnitude for 21UUV in Head Seas

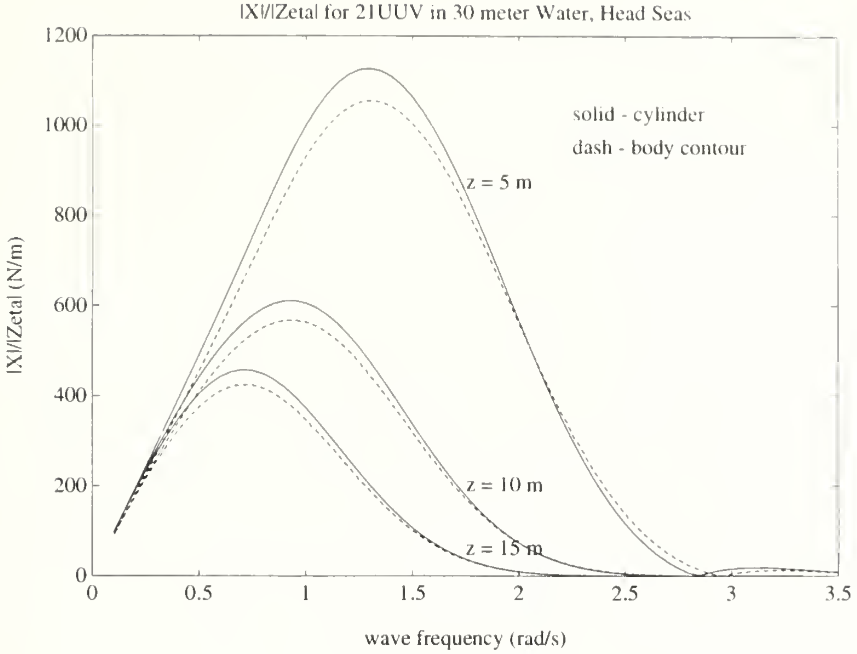

Figure 2.6 Surge Force Transfer Function Magnitude for 21UUV in Head Seas

2.2.2.2 Beam Seas

In left beam seas, the AUV longitudinal axis is considered to be rotated 90° from the incoming wave direction, and referring to figure 2.3, the regular wave propagation direction is taken in the positive y direction in the body-fixed coordinate system. Considering the range of wavelengths over the range of wave frequencies which are of interest, it is noted that $\lambda/D \geq 13$ for all wave frequencies below 3 rad/sec, and the approximation of uniform water acceleration across the diameter of the AUV is made. Strip theory then allows for the calculation of Y, Z, M, and N for the AUV in beam seas, while the roll moment, K, though expected to be of significance, cannot be reasonably calculated in this manner. Experimental methods best allow for determination of K in beam seas, and these will be explored in a later chapter.

Because Y and N are caused by horizontal water motion, the Keulegan-Carpenter number considered is that in the horizontal plane, namely

$$KC_h = 2\pi\xi_m/D \tag{2.37}$$

where

$$\xi_m = \zeta_a \frac{\cosh k(-z+h)}{\sinh kh} \tag{2.38}$$

Here the horizontal displacement parameter $\xi_m/D \le 1$ resulting in inertia dominated hydrodynamic forces and $C_M \cong 2$ is assumed.

Where the previously used cylinder model of the 21UUV can be used to calculate Y and Z, using this approach to calculate M and N would predict zero moment about the mid length position of the AUV, and therefore only the body contour method is used to calculate M and N in beam seas.

Using the two methods previously described,

$$Y_B(t) = A_2 K_{M2} L \cos\omega t \tag{2.39}$$

using the cylinder model of the body, or

$$Y_B(t) = A_2 \cos\omega t \int_{-L/2}^{L/2} K_{M2}(x)dx \tag{2.40}$$

using the body contour of the vehicle to calculate $K_{M2}(x)$. Here A_2 = A_1 and is taken from equation (2.8), $K_{M2} = K_{M3}$, and $K_{M2}(x) = K_{M3}(x)$ due to the symmetry of the vehicle. Similarly, Z is calculated

$$Z_B(t) = -A_3 K_{M3} L \sin\omega t \tag{2.41}$$

or

$$Z_B(t) = -A_3 \sin \omega t \int_{-L/2}^{L/2} K_{M3}(x)dx \tag{2.42}$$

for the cylinder model and body contour model, respectively.

The moments M and N are found from

$$M_B(t) = A_3 \sin \omega t \int_{-L/2}^{L/2} x\, K_{M3}(x)dx \tag{2.43}$$

and

$$N_B(t) = A_2 \cos \omega t \int_{-L/2}^{L/2} x\, K_{M2}(x)dx \tag{2.44}$$

respectively.

Figures 2.7 through 2.10 show examples of the calculated transfer function magnitudes for $|Y_B(\omega)|/|\zeta_a(\omega)|$, $|Z_B(\omega)|/|\zeta_a(\omega)|$, $|M_B(\omega)|/|\zeta_a(\omega)|$, and $|N_B(\omega)|/|\zeta_a(\omega)|$, respectively for the 21UUV in beam seas, 30 meter deep water and at various depths using the methods described above. Comparing figures 2.7 and 2.8, the transfer function magnitudes are identical for the Y and Z forces except at low frequencies where, because of the larger wavelength to water depth ratio, the water particle motion decays more rapidly with depth for the vertical motion than for horizontal water particle motion. The same can be said when comparing the M and N moments in figures 2.9 and 2.10. Because there is little fore-aft asymmetry in the 21UUV, the predicted pitch and yaw moments in beam seas are seen to be relatively small compared to the predicted pitch moment in head seas (figure 2.5). Finally, comparing Z_H in head seas versus Z_B in beam seas (figures 2.4 and 2.8), it is observed that at low frequencies, the magnitudes of the transfer

functions are identical. At higher frequencies where the wavelength is shorter and of the order of the vehicle length, $|Z_H|/|\zeta_a|$ is predictably smaller than $|Z_B|/|\zeta_a|$.

The application of strip theory in calculating forces and moments on an AUV in head and beam seas in an inertia dominated hydrodynamic force regime has allowed for the prediction of the transfer function from surface wave amplitude to forces and moments on the AUV. The standing assumption has been that water particle motion at the depth of the AUV is small enough so that nonlinear hydrodynamic form drag is insignificant when compared to the linear hydrodynamic inertia forces.

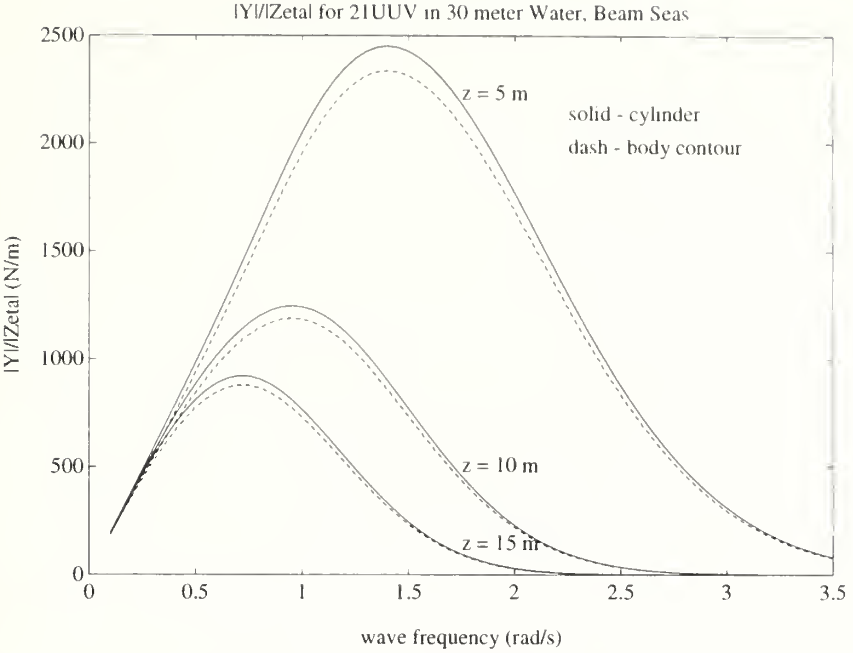

Figure 2.7 Sway Force Transfer Function Magnitude for 21UUV in Beam Seas

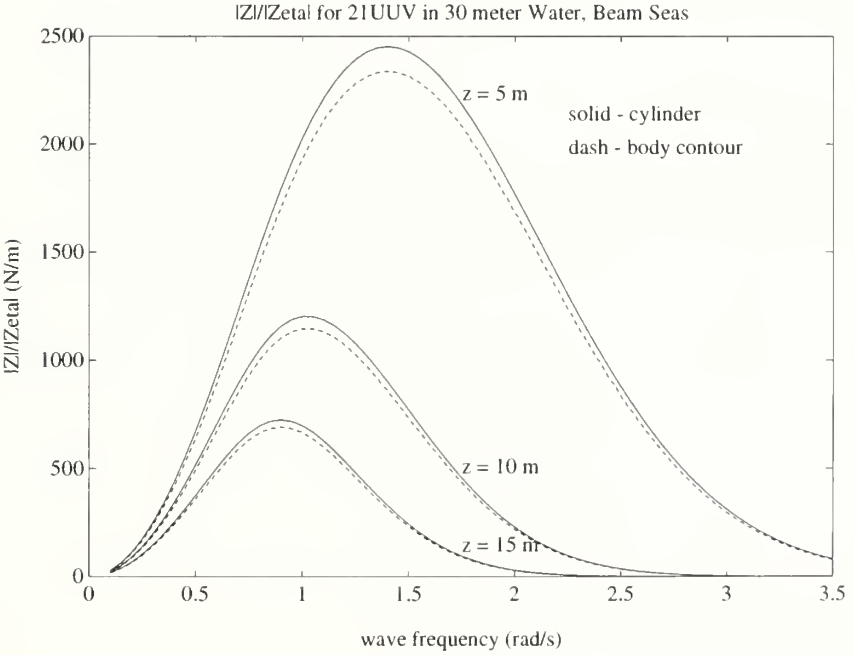

Figure 2.8 Heave Force Transfer Function Magnitude for 21UUV in Beam Seas

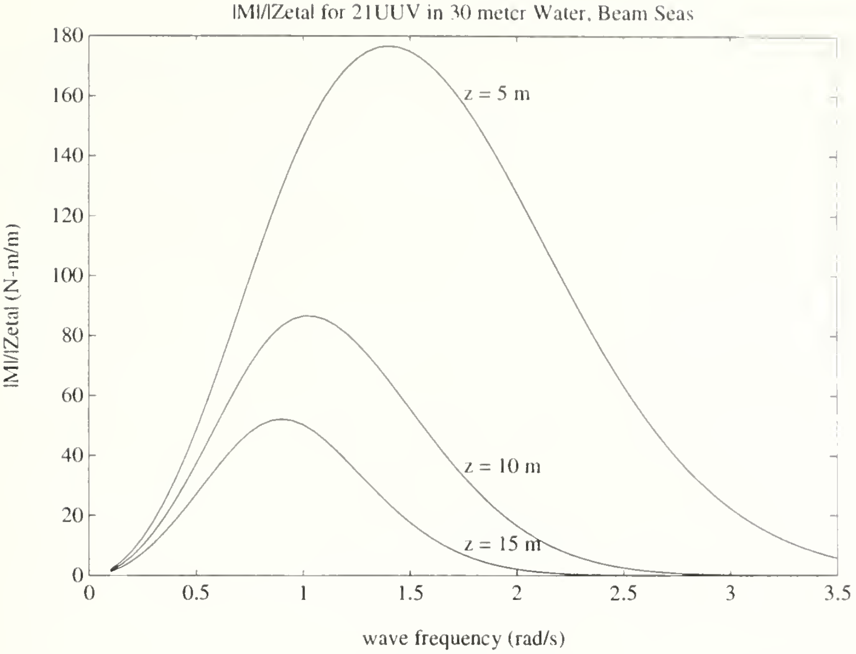

Figure 2.9 Pitch Moment Transfer Function Magnitude for 21UUV in Beam Seas

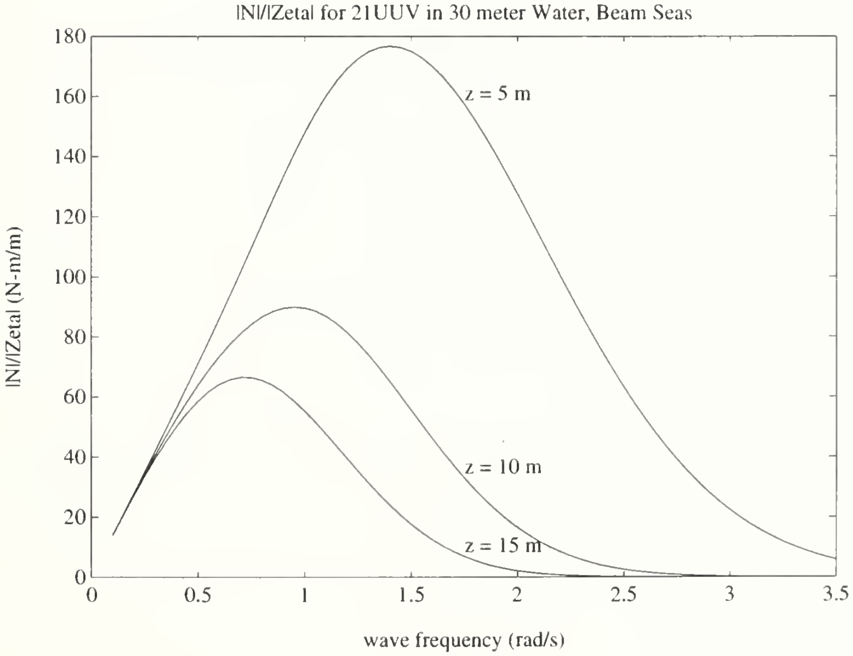

Figure 2.10 Yaw Moment Transfer Function Magnitude for 21UUV in Beam Seas

2.2.3 LTI Systems with Stochastic Inputs

Figure 2.11 depicts a linear time invariant (LTI) system with stable, proper transfer function G(s), input u(s), and output y(s), where $s = \left(\frac{d}{dt}\right)$ is the Laplace operator.

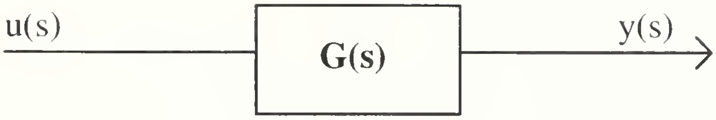

Figure 2.11 LTI System

Such systems have long been studied, and presented below is a well-known result which will be used in later discussions. For a thorough treatment of the subject of LTI systems with stochastic inputs, the reader can consult (Papoulis 1984), wherein the proof of the following result is contained.

For the system in figure 2.11, if u(t) is a known input, and G(t), the impulse response of the transfer function G(s) is known, then y(t) is known and can be expressed

$$y(t) = y(0) + \int_0^t u(\tau)G(t-\tau)d\tau \qquad (2.45)$$

Considering the case when u(t) is a stationary, random process with known power spectrum, then y(t) is also a stationary, random process. The power spectrum of y(t) can be calculated as

$$\Phi_{yy}(\omega) = |G(j\omega)|^2 \Phi_{uu}(\omega) \qquad (2.46)$$

where $|G(j\omega)|$ is the magnitude of the transfer function G(s) evaluated at $s = j\omega$. It follows then, that the single-sided spectrum of y(t), from equation (2.19) is

$$S^{+}_{yy}(\omega) = \begin{cases} \frac{1}{\pi}\Phi_{yy}(\omega) & \omega \geq 0 \\ 0 & \omega < 0 \end{cases} \tag{2.47}$$

The significance of the above result is that the previous discussion relating surface wave action to forces and moments on an AUV has been cast in such a framework. It can be seen that if the magnitude of the transfer functions between sea surface waves and forces and moments on an AUV are known, then the statistics of the forces and moments on the AUV body can be determined.

As an example, the pitch disturbance spectrum on the 21UUV in head seas and sea state 2 conditions are calculated for various depths of the vehicle and depicted in figure 2.12. In generating these spectra, the ITTC recommended Bretschneider wave amplitude spectrum for sea state 2 was used, as well as the body contour generated transfer function from wave amplitude to pitch disturbance depicted in figure 2.5.

Figure 2.13 depicts two possible time realizations of this pitch disturbance which are generated using the technique described in section 2.1.2 for generating time realizations of surface waves. The differences between the two realizations are due to the random phase used in each simulation. There are, of course, an infinite number of possible realizations of this pitch disturbance, each having the spectral representation depicted in figure 2.12.

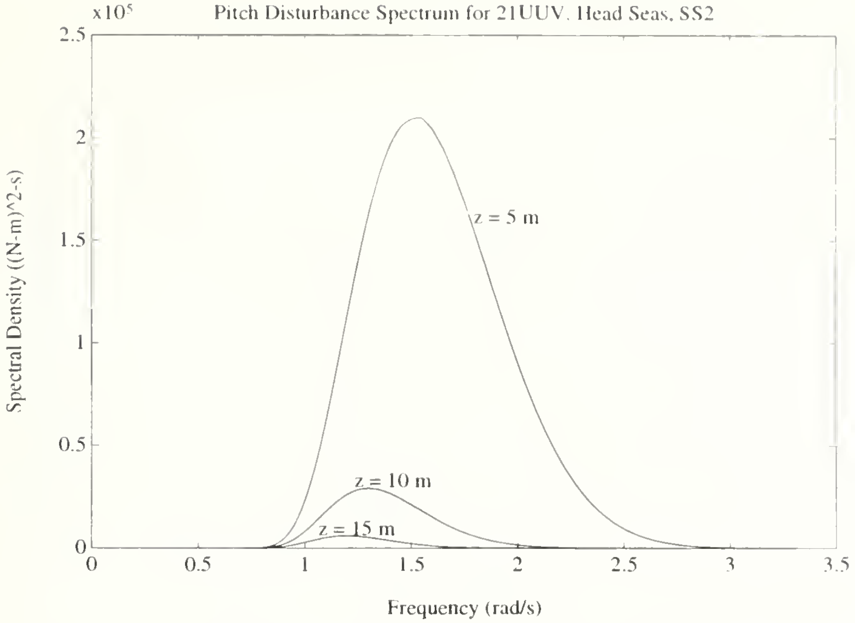

Figure 2.12 Pitch Disturbance Spectrum for 21UUV in Head Seas for Sea State 2 and at Various Depths

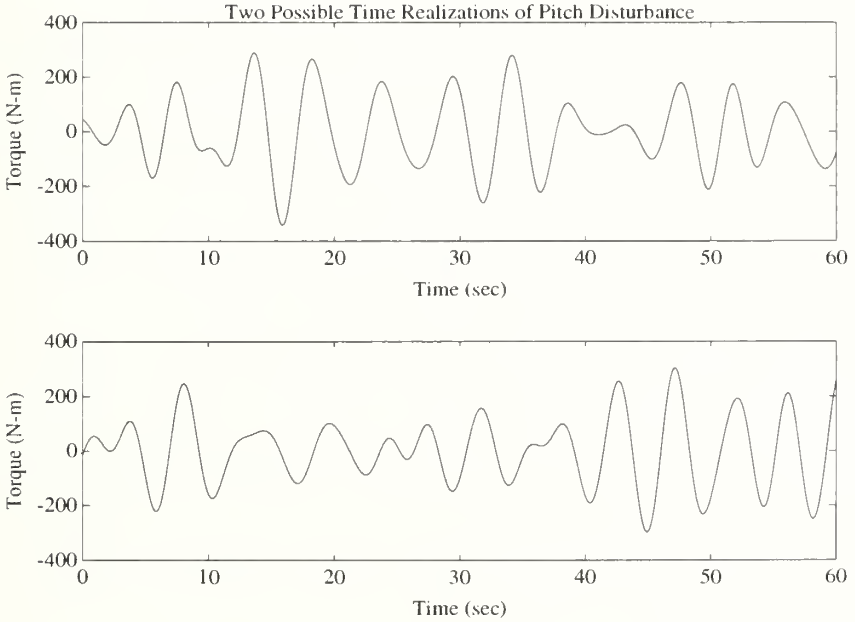

Figure 2.13 Two Possible Time Realizations of Pitch Disturbance to 21UUV in Head Seas, Sea State 2 and at 10 Meters Depth

Chapter 3 EXPERIMENTAL TESTING

In this chapter, experiments which test the theory of chapter 2 are discussed, and results of tests conducted on a 21UUV model are presented and compared with the earlier developed theory. While chapter 2 theory deals with forces on a stationary body, the wave forces on a forward moving AUV are also of interest as many AUV missions are conducted while the vehicle is moving with forward velocity. Also presented here, then, are experimental results of wave forces on a forward moving AUV model.

3.1 Experimental Setup

The experimental apparatus and AUV model are shown in figures 3.1 and 3.2.

3.1.1 Experimental Apparatus

The Massachusetts Institute of Technology's Ocean Engineering Testing Tank was used to conduct model testing. The tank has dimensions 110 feet (length) by 8 feet (width) by 4 feet (depth), is filled with fresh water, and is equipped with a wave maker and moving carriage.

The carriage assembly is suspended by rollers from a cylindrical beam fixed to the ceiling along the length of the tank. The carriage, on which a mast and AUV model were mounted, are capable of sliding the length of the tank, with the AUV model submerged in the tank water. Also affixed to the carriage assembly is a belt drive which can propel the carriage at speeds up to 2 meters per second along the beam. The speed of the carriage is controlled, and from a dead stop, the belt drive reaches a desired speed within 2 seconds of activation.

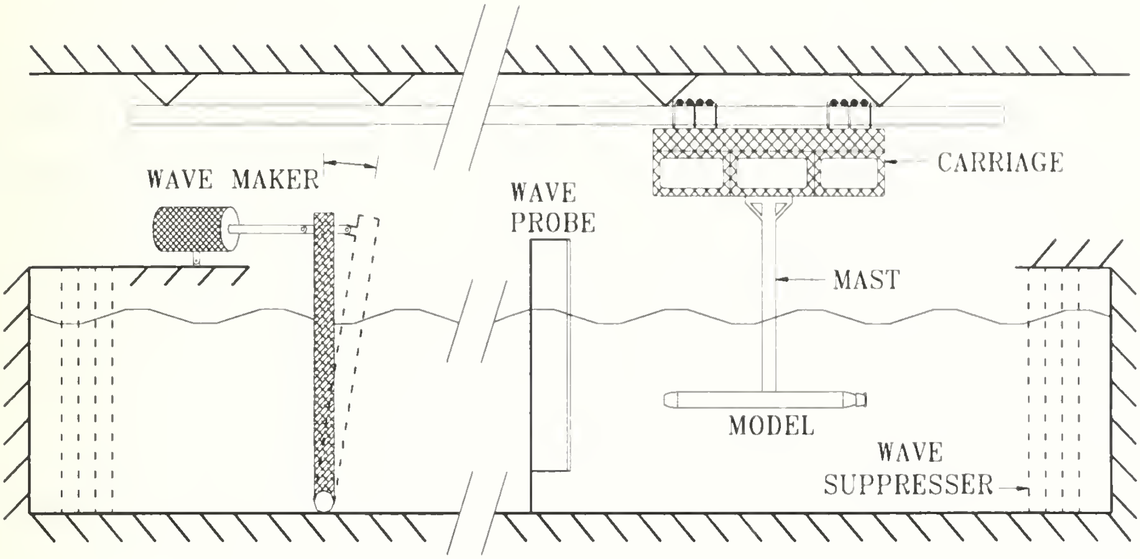
WAVE MAKER
WAVE PROBE
CARRIAGE
MAST
MODEL
WAVE SUPPRESSER

Figure 3.1 Experimental Apparatus Setup

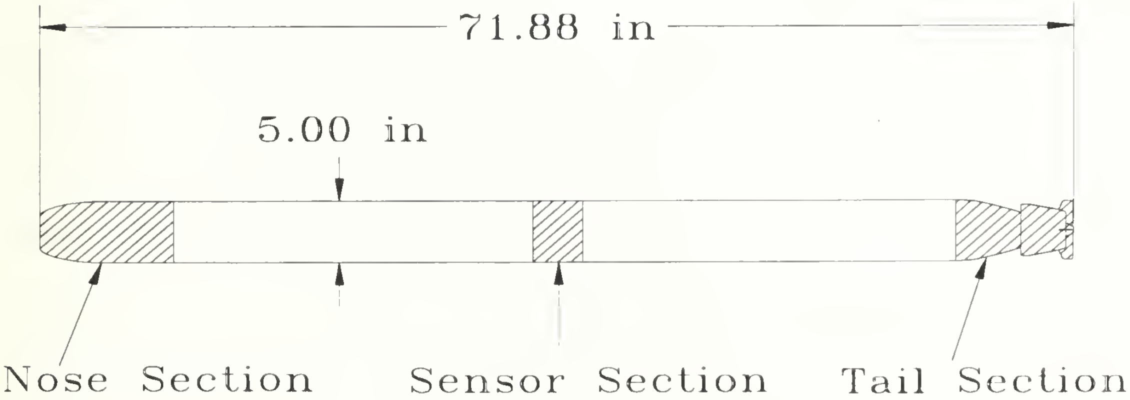
71.88 in
5.00 in
Nose Section
Sensor Section
Tail Section

Figure 3.2 21UUV Model Used in Testing

The wave maker, located near one end of the tank, consists of a rigid metal wall spanning the width and depth of the tank. The metal wall is allowed to pivot about its attachment to the bottom of the tank, and it is driven by a hydraulic actuator mounted at its top. Waves of frequencies between 0.2 Hz and 3.0 Hz can be generated. At the far end of the tank from the wave maker is densely packed plastic netting suspended in the water which acts as a wave suppresser. The suppresser absorbs much of the wave energy as it reaches the "beach" end of the tank, thus largely reducing the amount of reflected wave energy in the tank.

The wave probe used for measuring wave height uses two parallel copper wires separated by approximately one centimeter mounted on a stiff frame and positioned vertically in the water. A potential is applied between the two wires, and the varying resistance, resulting from the change in water level due to waves, is the means by which water elevation is measured. The wave probe was calibrated at the beginning and end of each data collection set.

3.1.2 AUV Model

The AUV test model was manufactured as a 1:4.188 scale model of the 301 inch long version of the 21UUV being developed at NUWC. The model body contour is precisely that of the 21UUV, including the contour of the tail section and fins. The model was constructed in 5 parts, and then assembled. The nose and tail sections were manufactured from PVC, while the two inner cylindrical sections were made from hollow cast acrylic tubing. The sensor section of the model, manufactured from 6061-t6 aluminum, housed a 6-axis strain gauge sensor which was mounted to the model at the sensor's bottom and to the rigid support mast at the sensor's top. As a result, the resultant hydrodynamic forces and moments on the AUV model were transmitted through the sensor to the rigid support mast, allowing for their measurement. The five sections assembled as depicted in figure 3.2 and resulted in a streamlined model of the full scale 21UUV.

The 6 axis strain gauge sensor was calibrated the first and last days of model testing.

During data collection, the sensor's 6 channels and the wave probe's 1 channel were simultaneously sampled at 30 hertz, with the data being recorded by a 386 personal computer.

3.2 Testing

3.2.1 Overview

Three series of tests were conducted: two series where the AUV model was kept stationary, and the third where the model was towed through the water with forward speed. In the first group of tests, the stationary model was oriented with its longitudinal axis perpendicular to the oncoming wave crests, i.e., as if in head seas. In the second series of tests, right beam seas were investigated and the stationary model was oriented with its longitudinal axis parallel to the oncoming wave crests. In the third series of tests, the model was towed with a fixed forward velocity counter to the direction of the wave propagation, simulating an AUV underway in head seas. For the tests involving a stationary model, the wave gauge was positioned to measure the water elevation at the mid-length position of the model, thus allowing for phase comparisons between the wave elevation and the forces and moments on the model.

The parameters varied during the course of the testing were:

(1) wave amplitude,

(2) wave frequency,

(3) AUV speed and orientation, and

(4) AUV depth

3.2.2 Scaling Considerations

3.2.2.1 Wave Frequencies

It is shown in chapter 2 that the ratio of wavelength to AUV length is a primary factor in the transfer function between the surface wave motion and the forces which affect the AUV. In addition, figure 2.1 depicts the range of wave frequencies over which the majority of wave energy is expected for a variety of sea conditions. Therefore, the frequencies of waves generated during the tests were chosen such that they produced a wavelength similar in scale to the model 21UUV length as full scale waves would produce relative to the full scale 21UUV length in a similarly scaled water depth.

An example clarifies the calculation:

Example of Wave Frequency Scaling

Given:

Wave tank depth	48 in (1.2192 m)
Scale of model	1:4.188
Full scale wave frequency (for example)	2 rad/sec
Full scale 21UUV length	301 in (7.6454 m)
Gravity	$9.806\ \mathrm{m/s^2}$

Calculation:

Full scale depth (model depth / scale)	5.106 m
Full scale wavelength (equation (2.2))	14.984 m
Model wavelength (scaled)	3.578 m
Model frequency (equation (2.2))	4.093 rad/sec

Table 3.1 contains the frequencies and wavelengths of waves (full scale and resulting model) used during testing. The 20 frequencies of full scale waves indicated in table 3.1 span the

range of frequencies expected of ocean waves as described by the ITTC recommended wave spectrum.

3.2.2.2 AUV Speeds

While conducting the tests during which the model AUV was towed, the Froude number of the full scale 21UUV was considered in determining the velocity at which to tow the model. Froude number similitude implies

$$\begin{aligned} Fr_{fs} &= \frac{U_{fs}}{\sqrt{gL_{fs}}} = \frac{U_m}{\sqrt{gL_m}} = Fr_m \\ U_m &= U_{fs}\sqrt{L_m / L_{fs}} \end{aligned} \tag{3.1}$$

where *fs* and *m* represent *full scale* and *model*, respectively. Data was collected at the two model tow speeds shown in table 3.2, and while higher tow speeds were considered, sensor load capacity precluded higher speed testing.

Full Scale		Model	
ω (rad/s)	λ (m)	λ (m)	ω (rad/s)
0.65	65.884	15.732	1.330
0.80	52.476	12.530	1.637
0.95	43.118	10.296	1.944
1.10	36.156	8.633	2.251
1.25	30.734	7.339	2.558
1.40	26.365	6.295	2.865
1.55	22.758	5.434	3.172
1.70	19.731	4.711	3.479
1.85	17.165	4.099	3.786
2.00	14.984	3.578	4.093
2.15	13.129	3.135	4.400
2.30	11.557	2.760	4.707
2.45	10.226	2.442	5.014
2.60	9.099	2.173	5.321
2.75	8.141	1.944	5.628
2.90	7.324	1.749	5.935
3.05	6.622	1.581	6.242
3.20	6.017	1.437	6.549
3.35	5.490	1.311	6.856
3.50	5.030	1.201	7.163

Table 3.1 Frequencies and Wavelengths Investigated During Testing

U_{fs} (m/s)	1.0	1.5
U_m (m/s)	0.489	0.733

Table 3.2 Tow Speeds Investigated During Testing

3.2.3 Tests Conducted

Table 3.3 summarizes the 320 trials conducted during the course of testing.

Wave to Model Aspect	Model Speed (m/s)	Model Centerline Depth (m)	Wave Amp per Frequency	# of Frequencies
Head	0	0.379	3	20
Head	0	0.787	3	20
Beam	0	0.379	3	20
Beam	0	0.787	3	20
Head	0.489	0.379	2	20
Head	0.733	0.379	2	20

Table 3.3 Summary of Tests Conducted

The 20 wave frequencies referred to in table 3.3 are those listed in table 3.1.

3.3 Test Results

3.3.1 Raw Data

The seven channels simultaneously recorded during each of the trials included the six axes from the sensor mounted inside the model body plus the wave gauge output. An example of the seven channels sampled (with force, torque, and wave amplitude conversions applied) during one test run is depicted in figures 3.3a through 3.3d. This particular sample produced three data points for the case of beam sea waves of 5.321 rad/s for the 0.379 meter deep model. As is

shown in figure 3.3, three wave amplitudes were generated during each trial when the model was held stationary. During tests in which the model was towed, wave amplitude was held constant during the course of each data run.

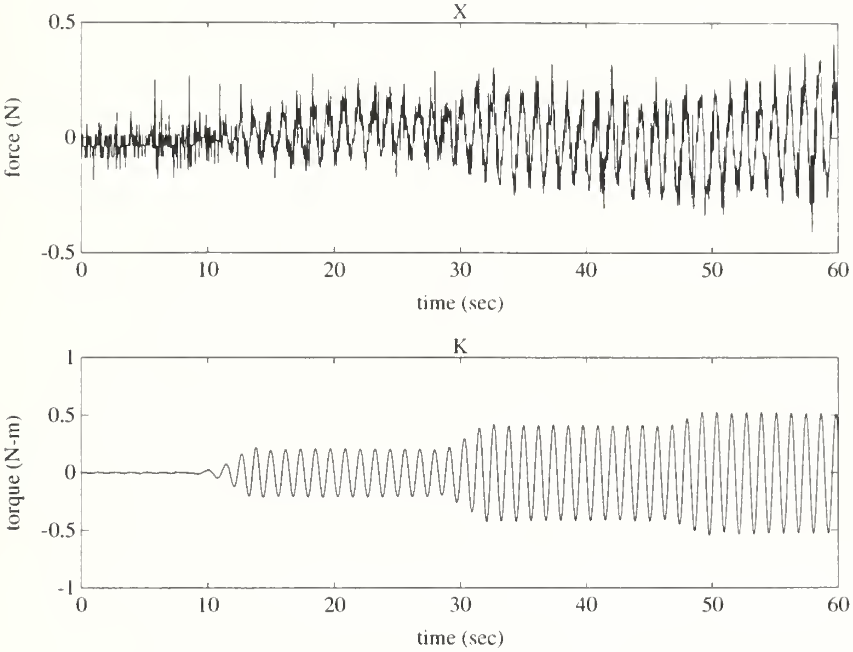

Figure 3.3a Sample of Surge Force and Roll Moment Raw Data. Beam sea effects are investigated here, and during this data collection run, wave amplitude was increased in three distinct steps as shown in figure 3.3d. While the amplitude of surge force, X, is only slightly larger than the sensor and A/D converter resolution, roll moment, K, more fully spans the sensor and A/D converter full range.

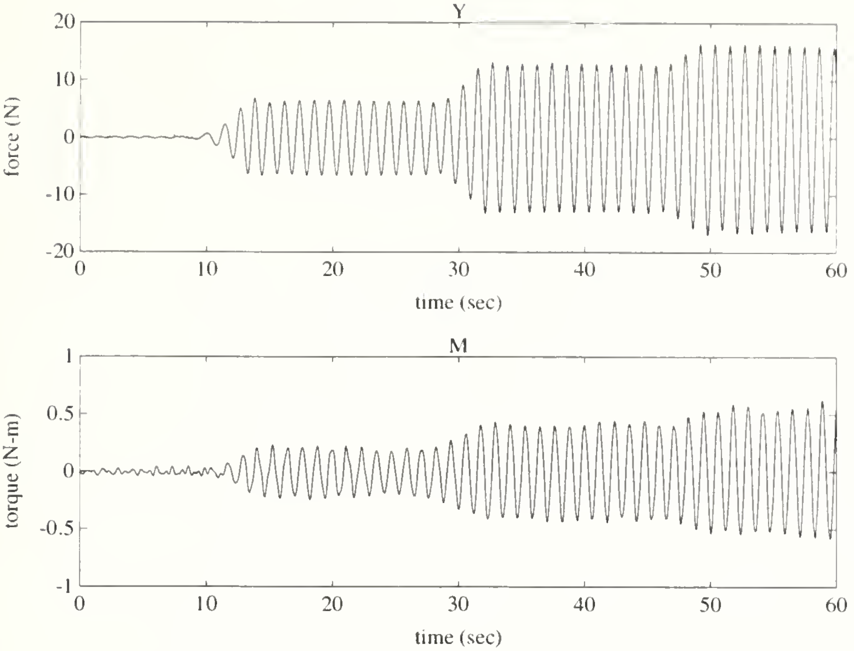

Figure 3.3b Sample of Sway Force and Pitch Moment Raw Data

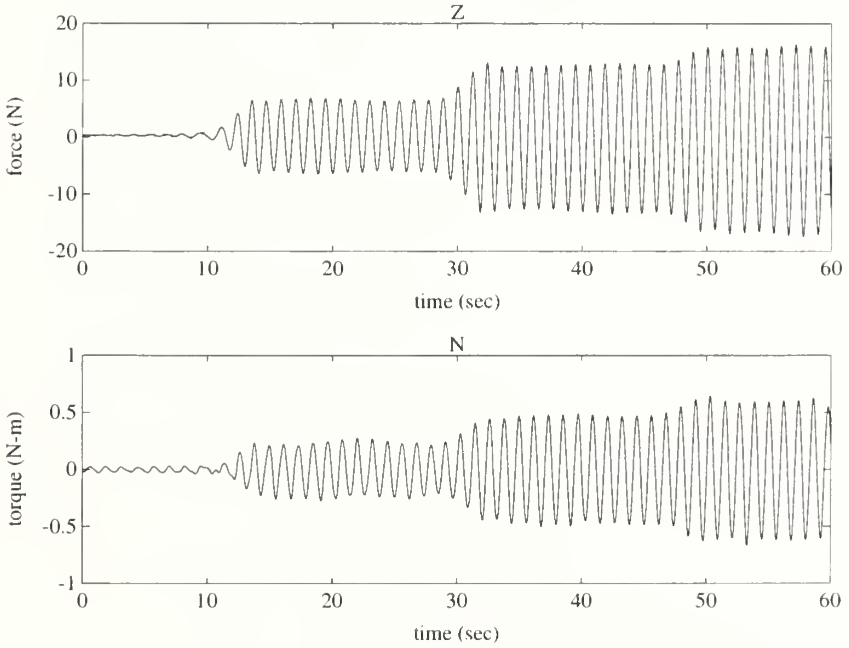

Figure 3.3c Sample of Heave Force and Yaw Moment Raw Data

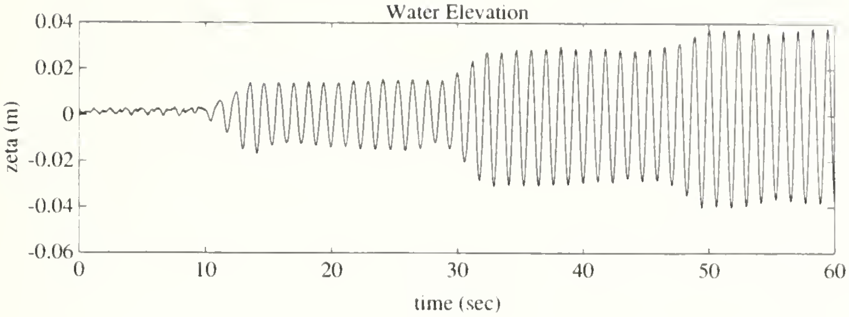

Figure 3.3d Sample of Water Elevation Raw Data

3.3.2 Signal Processing

The frequency of encounter between the model and waves is given in (Newman 1977) as

$$\omega_e = \omega_0 - kU\cos\theta \tag{3.2}$$

where ω_0 is the wave frequency, U is the forward speed of the model, and θ is the angle between the model x axis and the direction of wave travel. The highest frequency of encounter between the model and waves during testing was evaluated as 11.0 rad/s, or 1.75 Hz.

Prior to evaluating the amplitude of the signal coming from each of the seven channels, data from each channel was digitally filtered using a Chebyshev type II lowpass, stopband ripple filter (MATLAB 1992). The 9 pole filter had a cutoff frequency of 3.5 Hz and a stopband of negative 60 dB. A Bode plot of the filter frequency response is depicted in figure 3.4. The signals were first filtered in the forward, and then reverse directions to yield a zero phase shifted, filtered version of the output signals.

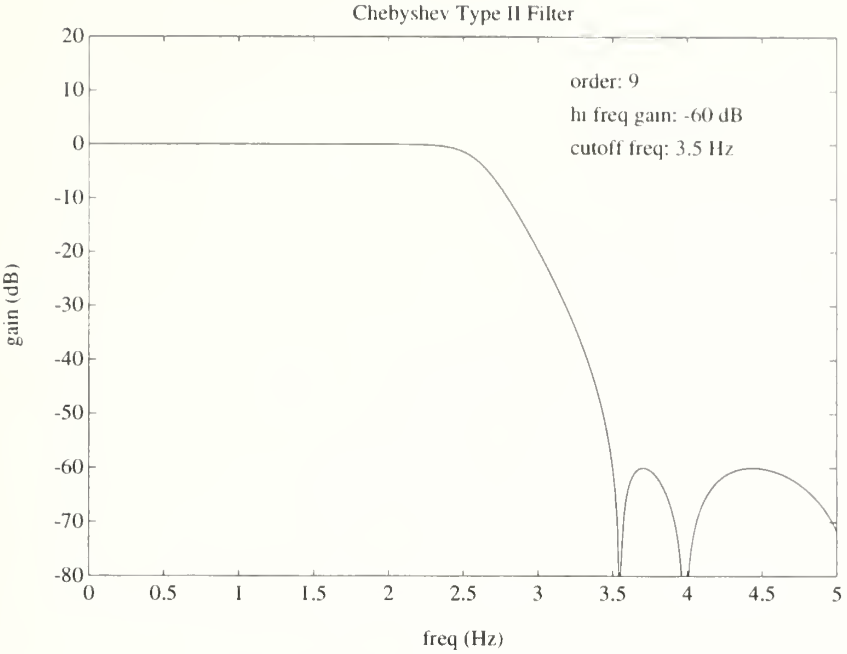

Figure 3.4 Frequency Response of Filter

Two examples of sampled and filtered signals (superimposed) are depicted in figure 3.5. The first of the two signals shown is the 35 to 45 second window of the Y force depicted in figure 3.3b. The second of the two signals shown is a 25 second window of the X force recorded while the model was being towed at 0.489 m/s under 2.251 rad/s waves. Filtering a low frequency and relatively noiseless signal such as Y in figure 3.5 leaves it virtually unchanged. The signal representing X in figure 3.5 has a significant level of high frequency carriage rumble noise superimposed upon it, and filtering a noisy signal such as this allowed better estimation of the amplitude of the wave induced hydrodynamic force.

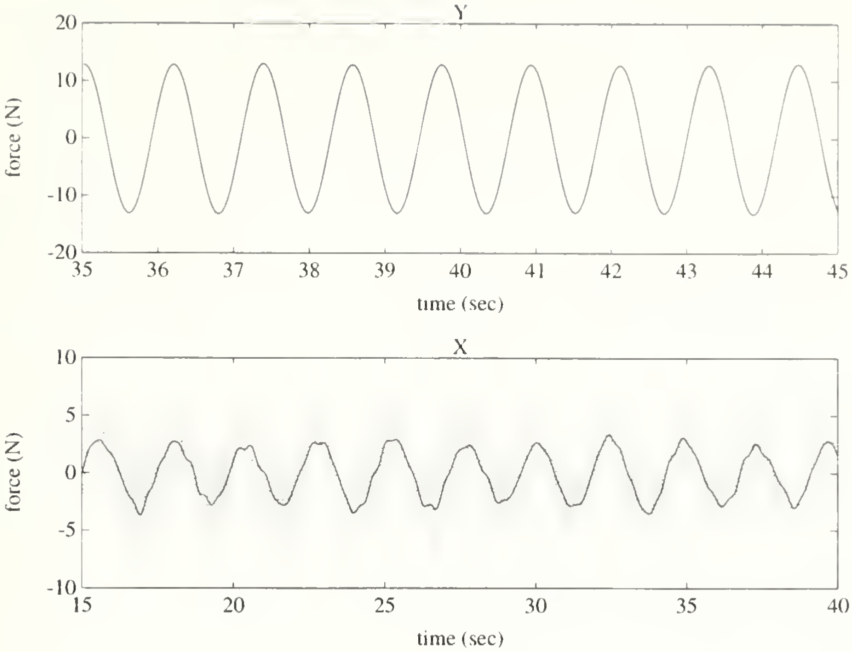

Figure 3.5 Two Samples of Unfiltered and Filtered Signals

3.3.3 Experimental Data vs. Theory

After the signals were filtered, amplitudes of the signals were determined and the ratios of force and torque to wave amplitude were calculated and plotted versus frequency. Additionally, the phase difference between the wave elevation sinusoid and force / torque signals were measured and plotted for the cases when the model was stationary. The vertical and horizontal displacement parameters were calculated for each test conducted and were found to be less than 0.4 in all cases, establishing the tests within the range of displacement parameters assumed in chapter 2.

3.3.3.1 Stationary Model in Head Seas

Figures 3.6 through 3.8 compare theoretical and experimental transfer function magnitude and phase information for X, Z, and M versus wave frequency for the model at a

centerline depth of 0.379 m. The theoretical curves were developed using the methods described in chapter 2 with the body contour of the model taken into account. Similarly, figures 3.9 through 3.11 compare the same transfer function magnitude and phase information for the model at a centerline depth of 0.787 m.

Resonance in the wave tank across its width at wave frequencies of 3.3 and 5 rad/s appear to cause erratic data near these frequencies during the course of testing, and the result is seen in the data presented here.

While the shallow and deep model data presented for the X and M transfer functions is well predicted by the theory both in phase and magnitude, the method used to predict the transfer function for Z fails to include a force component which accounts for the resultant vertical force when the water wavelength is the length of the model body. The predicted zero in X is observed at or near this frequency, as both figures 3.6 and 3.9 show in the magnitude and phase plots The phase of this unpredicted Z force is consistent with that which would be expected of vertical drag proportional to wave velocity in the aft section of the model body. The inclusion of such a drag component into the heave force model was investigated, and produced a far worse low frequency fit to the data than that presented in figures 3.7a and 3.10a. Because model accuracy is deemed more important at lower frequencies where the majority of wave spectral energy is expected, the previously developed model for heave force will be used in subsequent discussion.

It is seen that X, M and Z are all approximately linearly related to the wave amplitude $\zeta(\omega)$, thus allowing for their transfer function representation.

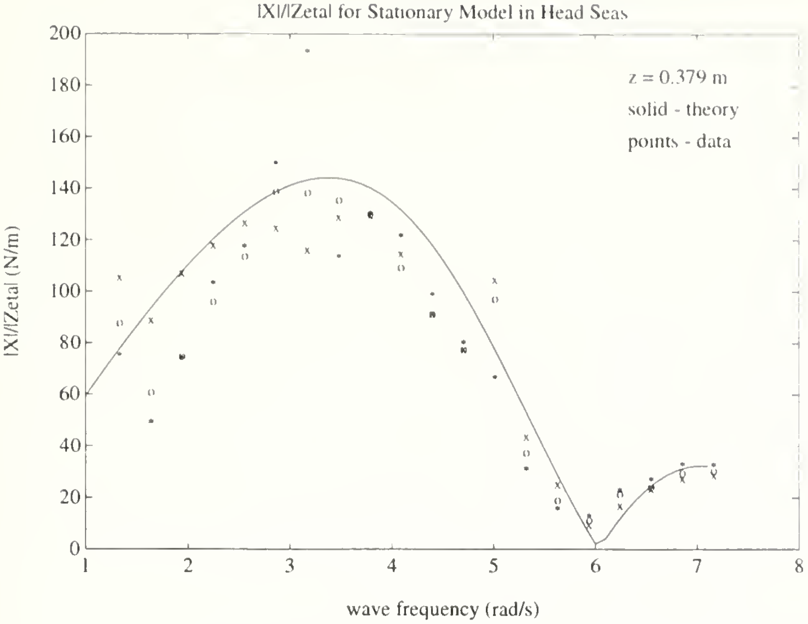

Figure 3.6a Surge Force Transfer Function Magnitude for Shallow Model in Head Seas

Note: The data points 'x', 'o', and '*' represent data taken from the model under waves of increasingly higher amplitudes, respectively.

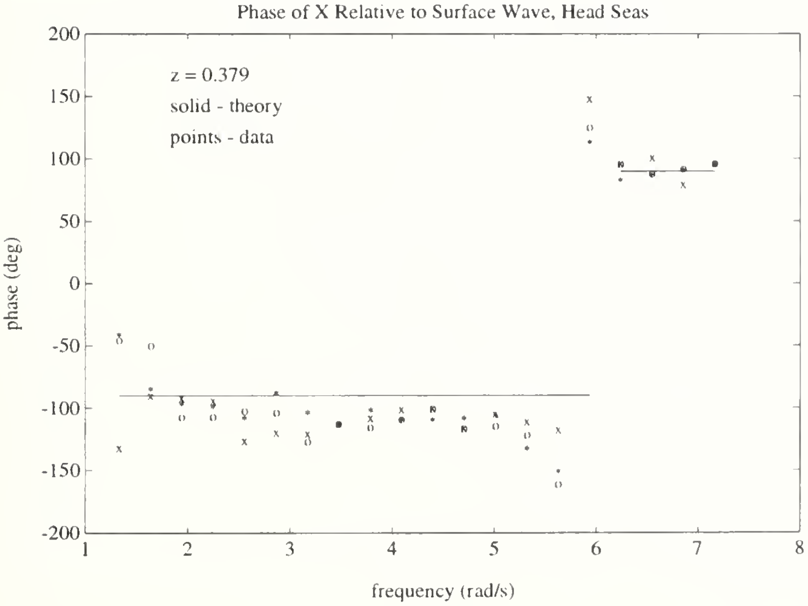

Figure 3.6b Surge Force Transfer Function Phase for Shallow Model in Head Seas

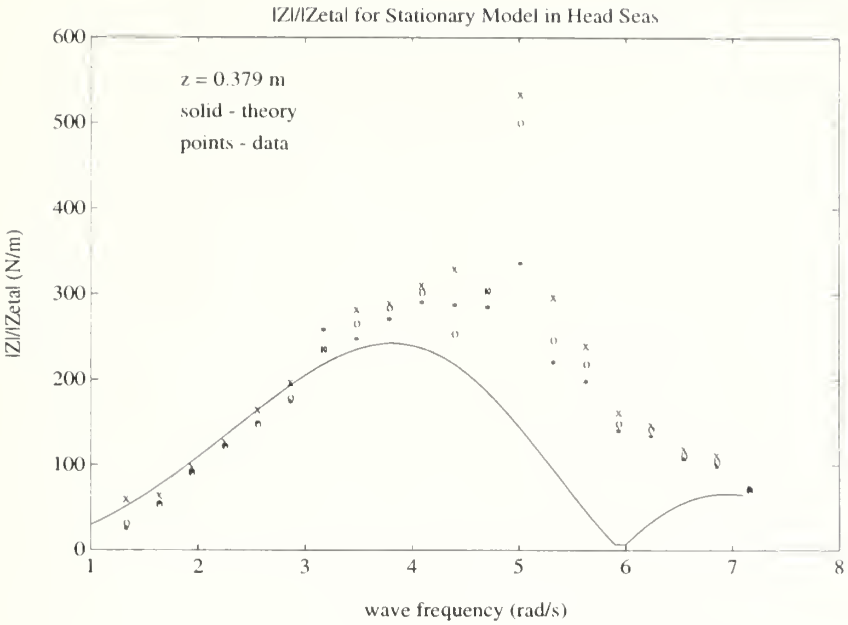

Figure 3.7a Heave Force Transfer Function Magnitude for Shallow Model in Head Seas. The erratic effect of wave tank resonance across its width at 5 rad/s is clearly seen.

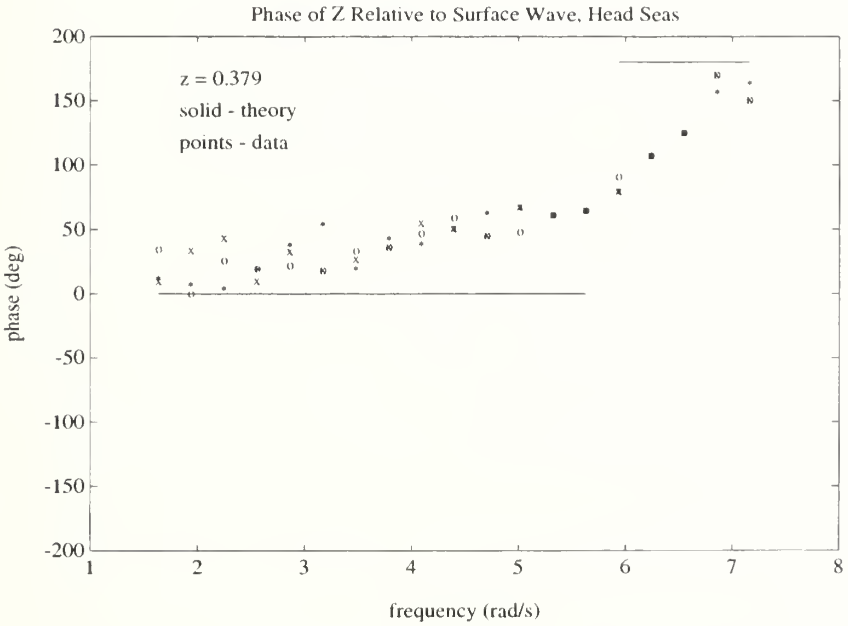

Figure 3.7b Heave Force Transfer Function Phase for Shallow Model in Head Seas

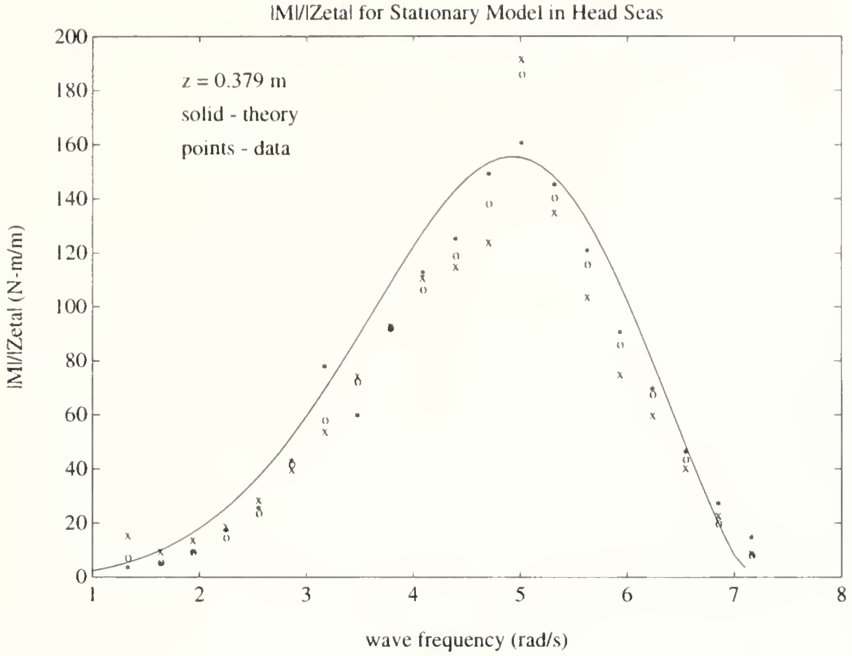

Figure 3.8a Pitch Moment Transfer Function Magnitude for Shallow Model in Head Seas. Again, the effect of wave tank resonance at 5 rad/sec is seen.

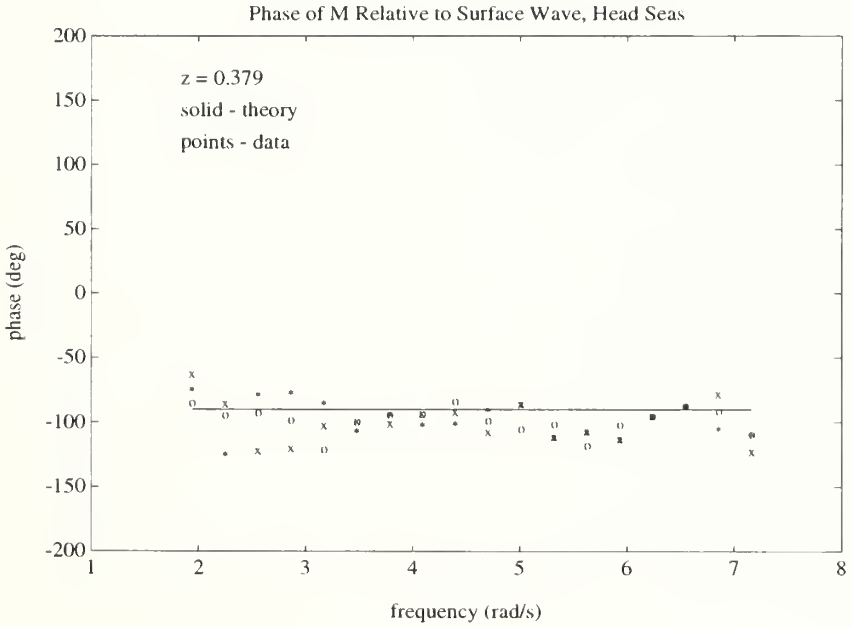

Figure 3.8b Pitch Moment Transfer Function Phase for Shallow Model in Head Seas

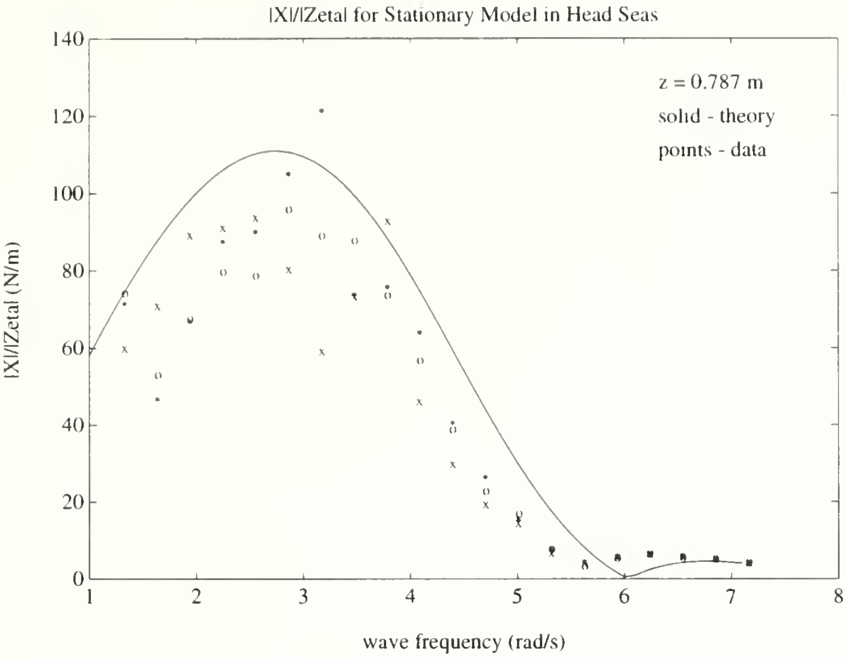

Figure 3.9a Surge Force Transfer Function Magnitude for Deep Model in Head Seas

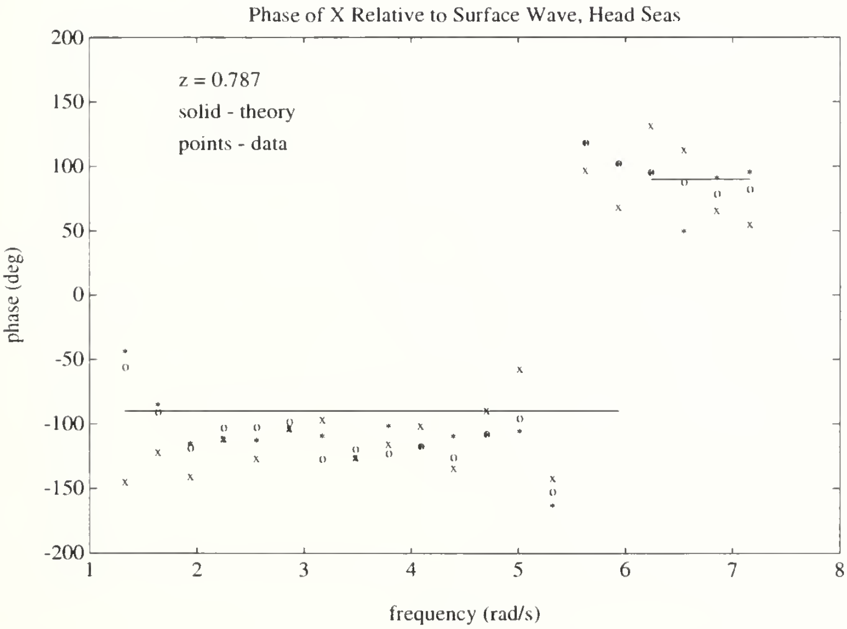

Figure 3.9b Surge Force Transfer Function Phase for Deep Model in Head Seas

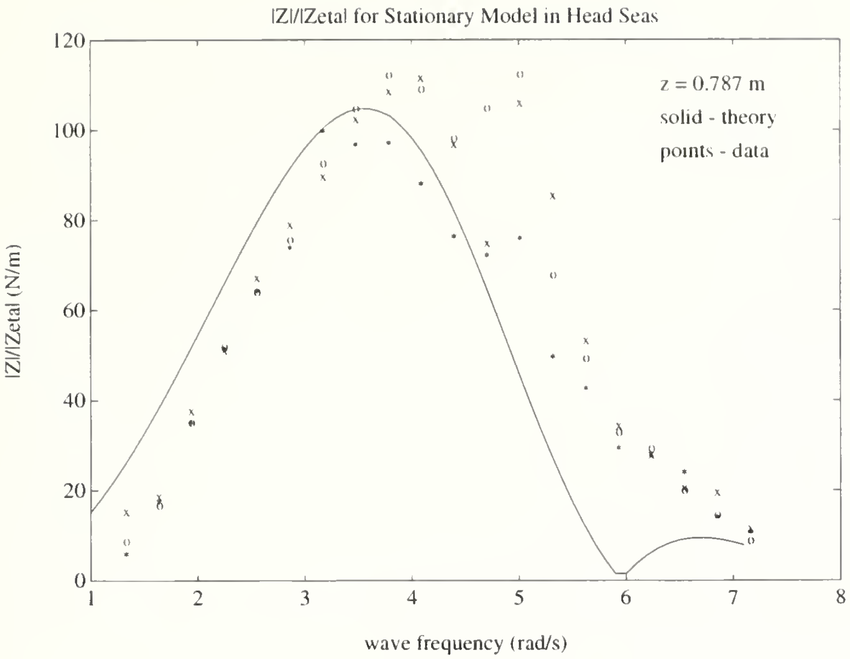

Figure 3.10a Heave Force Transfer Function Magnitude for Deep Model in Head Seas

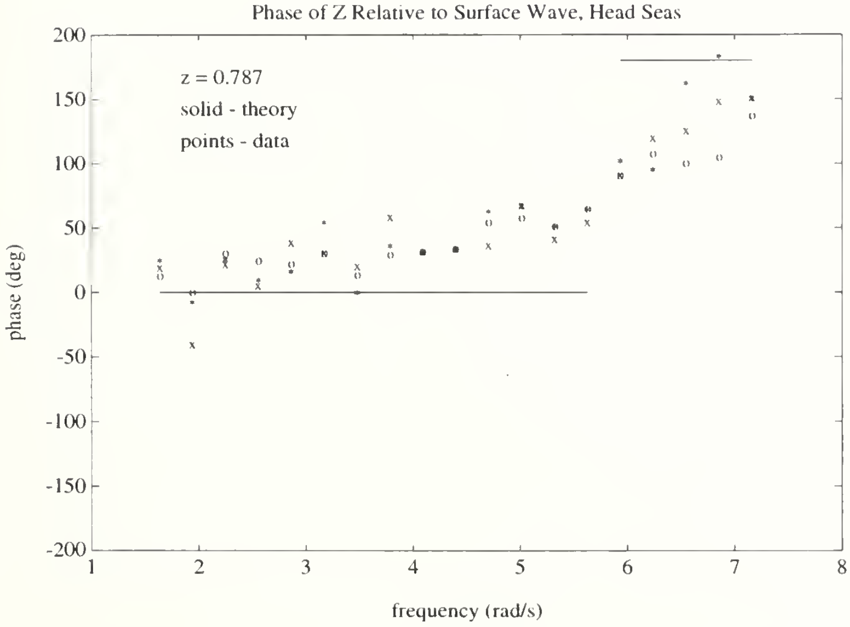

Figure 3.10b Heave Force Transfer Function Phase for Deep Model in Head Seas

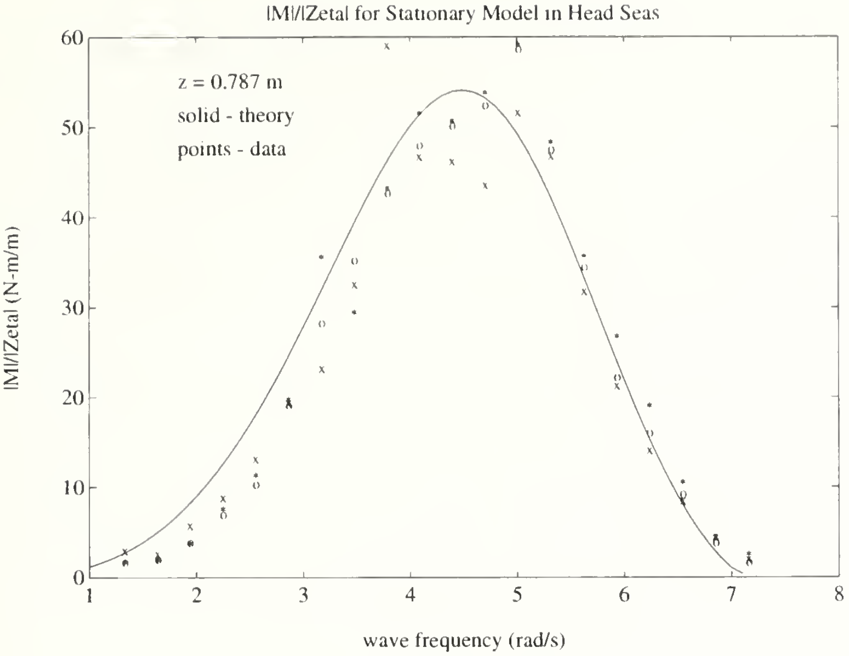

Figure 3.11a Pitch Moment Transfer Function Magnitude for Deep Model in Head Seas

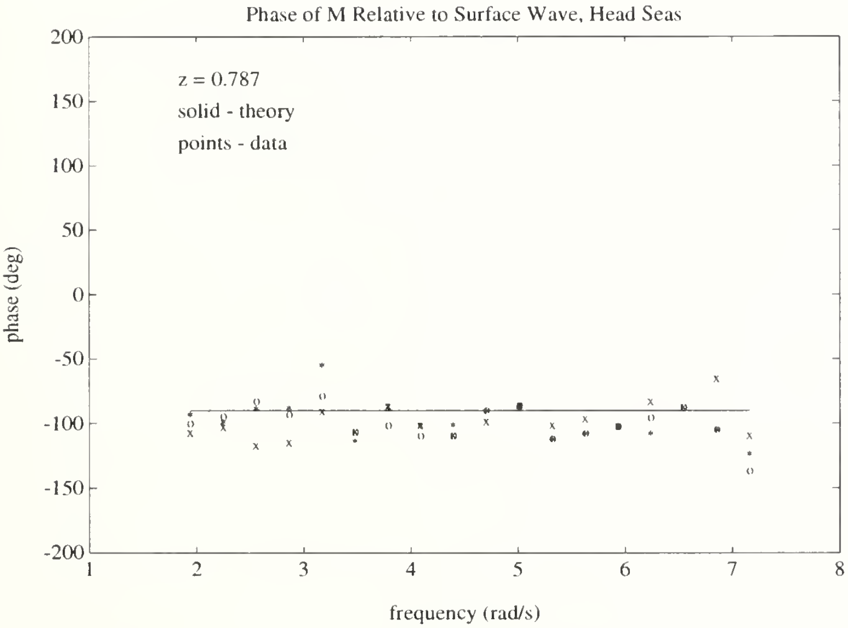

Figure 3.11b Pitch Moment Transfer Function Phase for Deep Model in Head Seas

3.3.3.2 Stationary Model in Beam Seas

Figures 3.12 through 3.16 compare theoretical and experimental transfer function magnitude and phase information for Y, Z, K, M and N versus wave frequency for the model at a centerline depth of 0.379 m. The theoretical curves were developed using the methods described in chapter 2 with the body contour of the model taken into account. Similarly, figures 3.17 through 3.21 compare the same transfer function magnitude and phase information for the model at a centerline depth of 0.787 m.

Again the data is well predicted by theory in phase and magnitude, with the exception of the prediction of K, where no theory is presented. The scatter in data for M and N is noted, as are the relatively small values of M and N when compared to M in head seas. Because the magnitudes of the M and N moments in beam seas are relatively small, sensor axis crosstalk and the effect of imperfect waves are possible causes of the scatter in data depicted in figures 3.15, 3.16, 3.20, and 3.21.

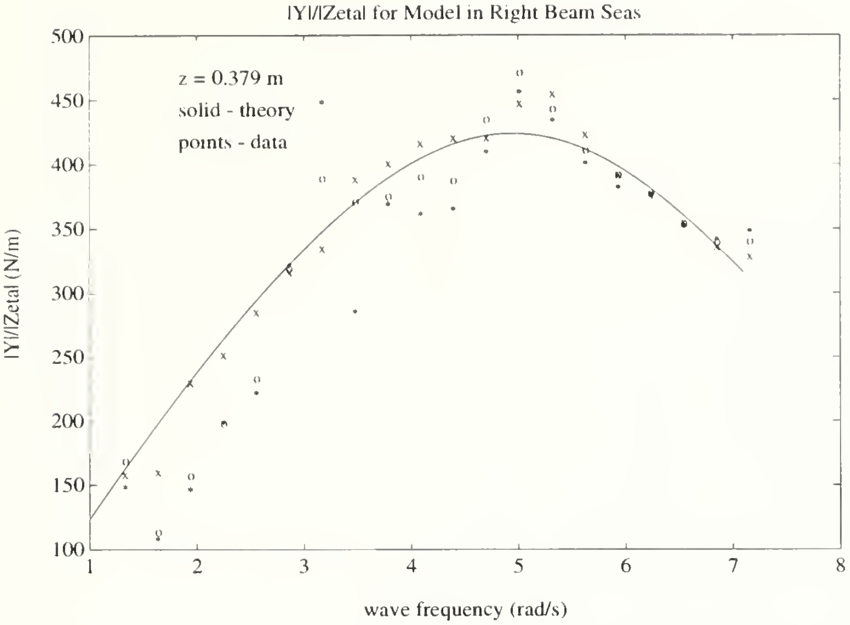

Figure 3.12a Sway Force Transfer Function Magnitude for Shallow Model in Beam Seas

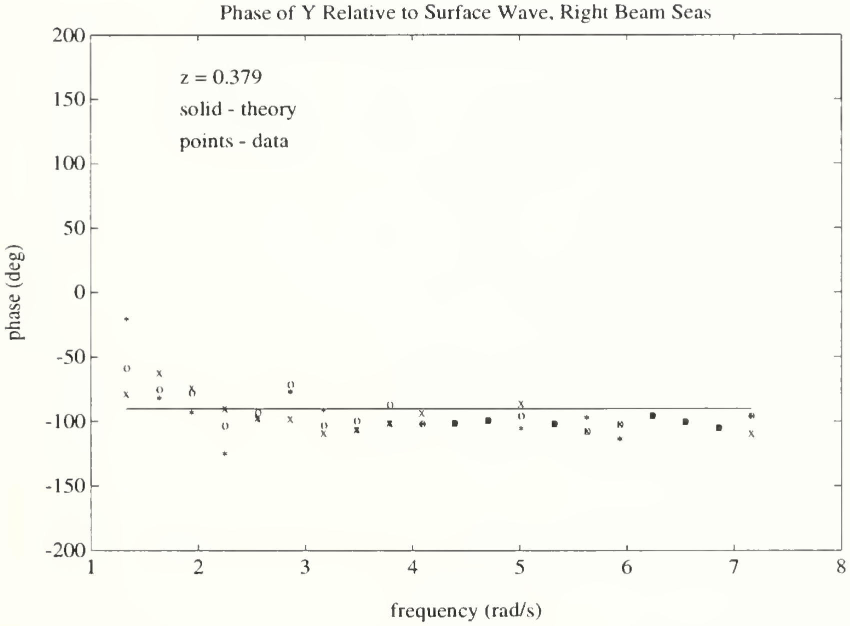

Figure 3.12b Sway Force Transfer Function Phase for Shallow Model in Beam Seas

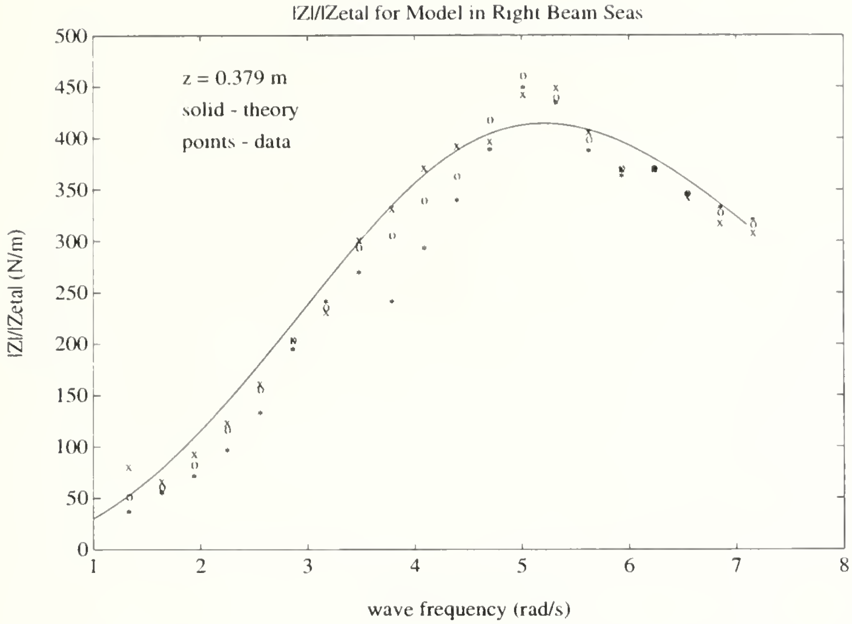

Figure 3.13a Heave Force Transfer Function Magnitude for Shallow Model in Beam Seas

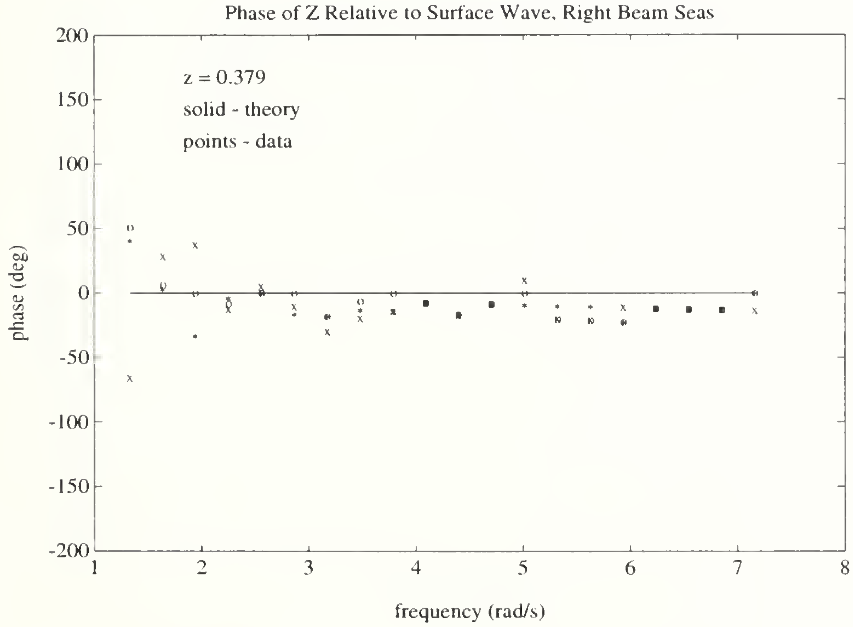

Figure 3.13b Heave Force Transfer Function Phase for Shallow Model in Beam Seas

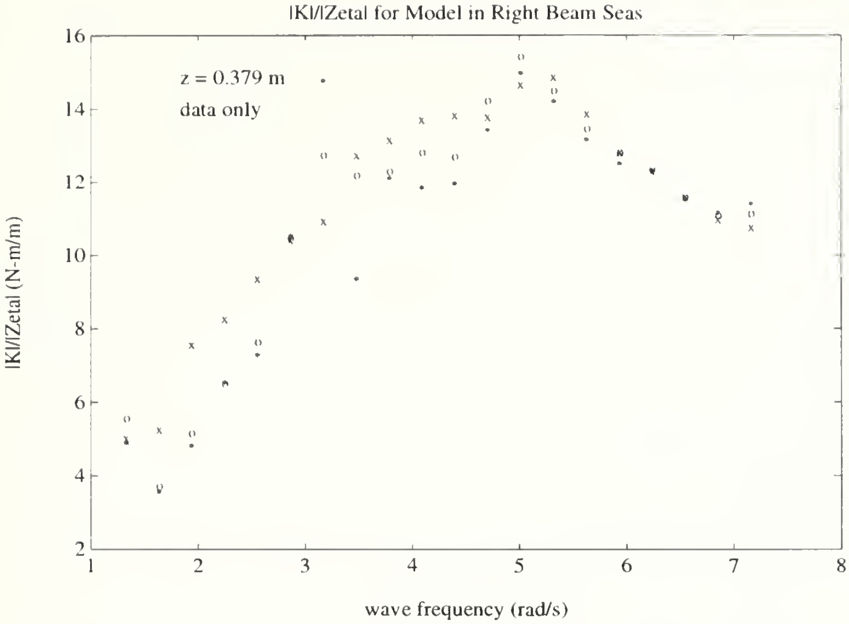

Figure 3.14a Roll Moment Transfer Function Magnitude for Shallow Model in Beam Seas

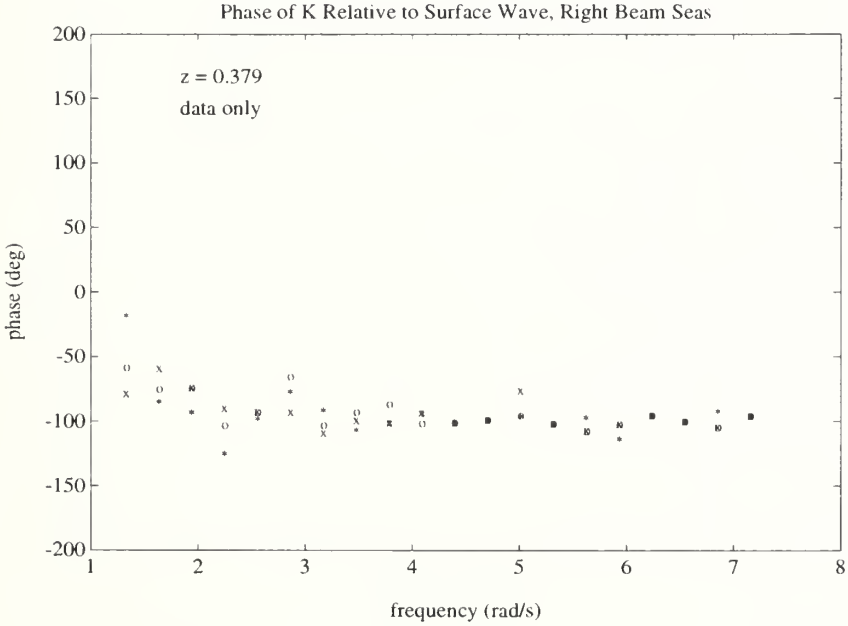

Figure 3.14b Roll Moment Transfer Function Phase for Shallow Model in Beam Seas

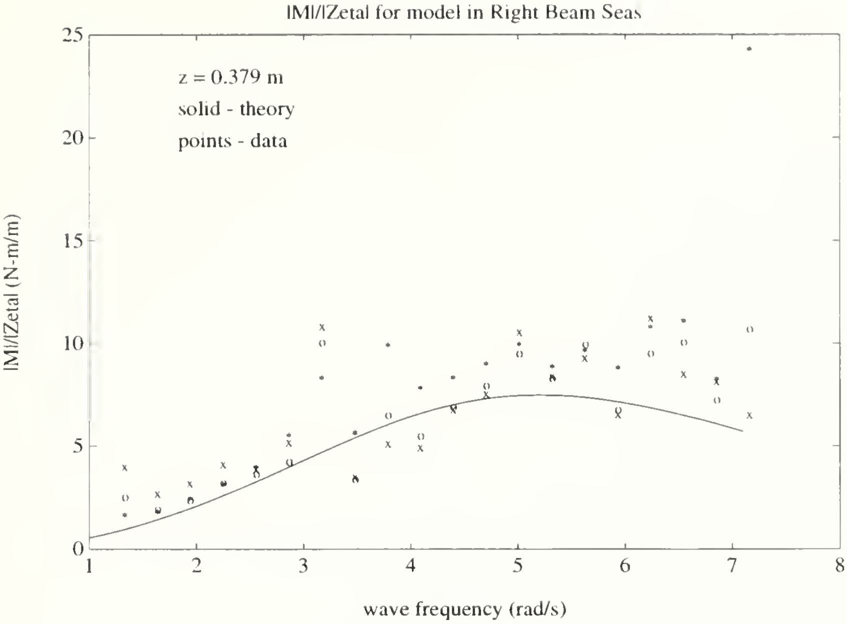

Figure 3.15a Pitch Moment Transfer Function Magnitude for Shallow Model in Beam Seas

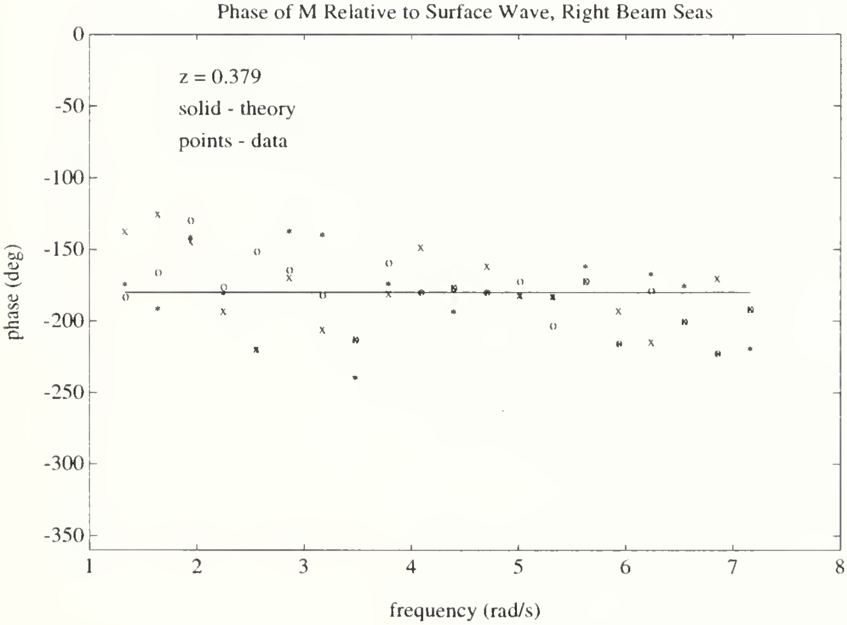

Figure 3.15b Pitch Moment Transfer Function Phase for Shallow Model in Beam Seas

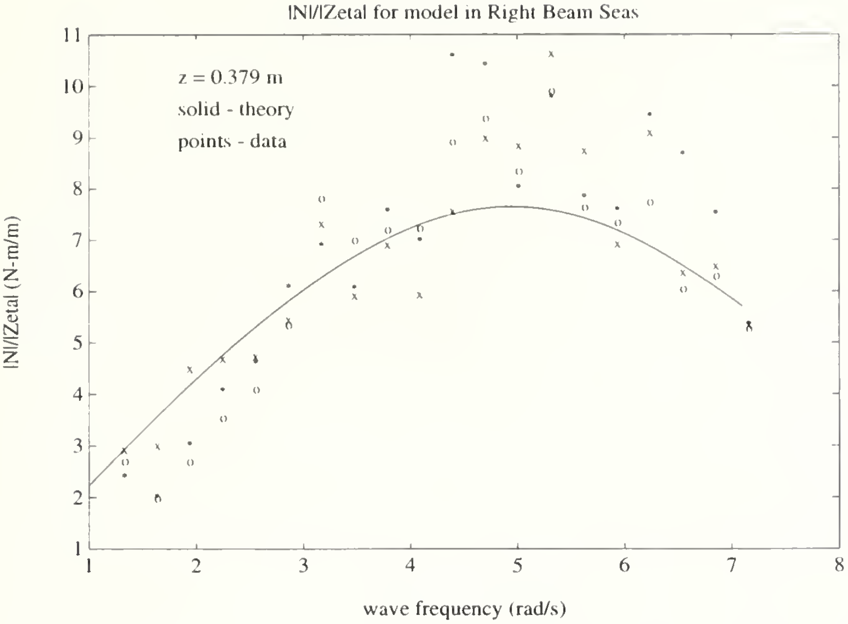

Figure 3.16a Yaw Moment Transfer Function Magnitude for Shallow Model in Beam Seas

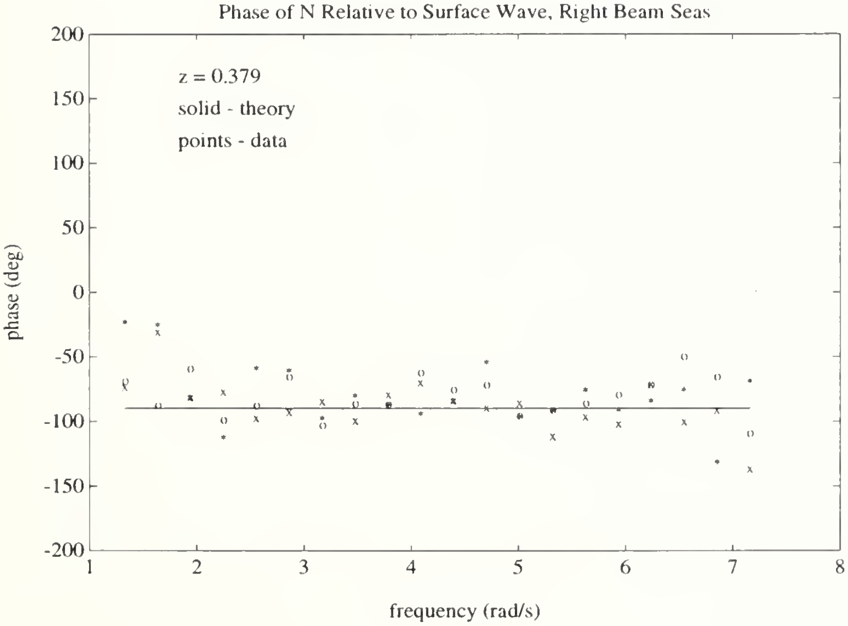

Figure 3.16b Yaw Moment Transfer Function Phase for Shallow Model in Beam Seas

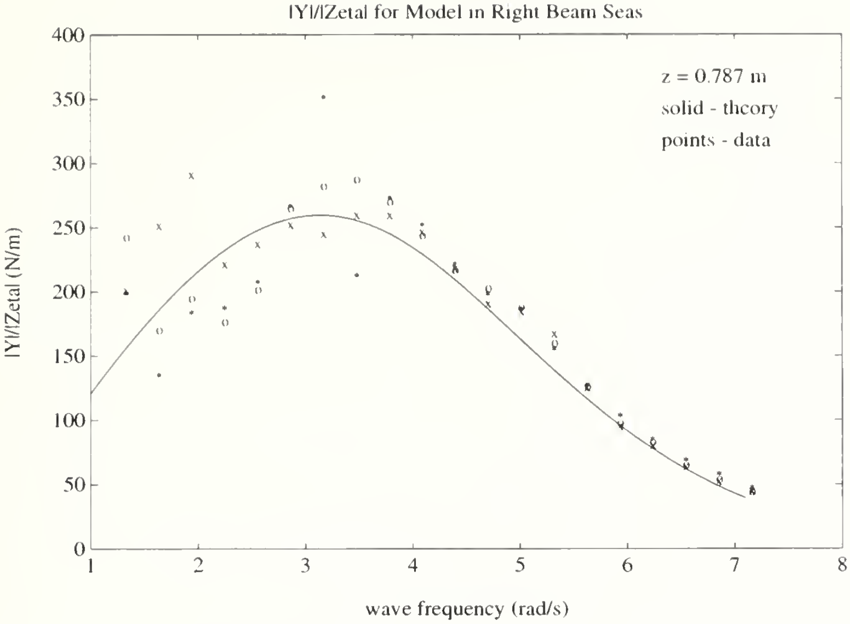

Figure 3.17a Sway Force Transfer Function Magnitude for Deep Model in Beam Seas

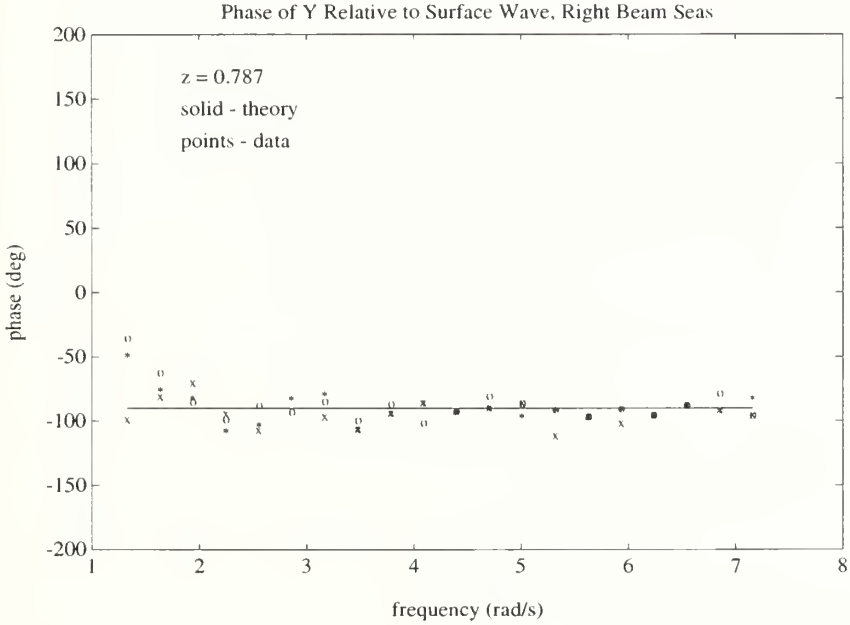

Figure 3.17b Sway Force Transfer Function Phase for Deep Model in Beam Seas

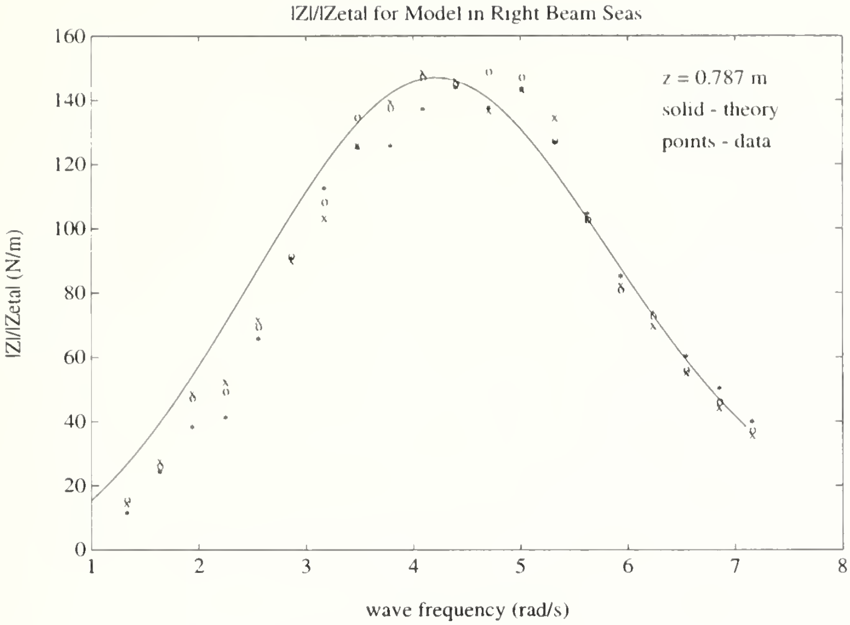

Figure 3.18a Heave Force Transfer Function Magnitude for Deep Model in Beam Seas

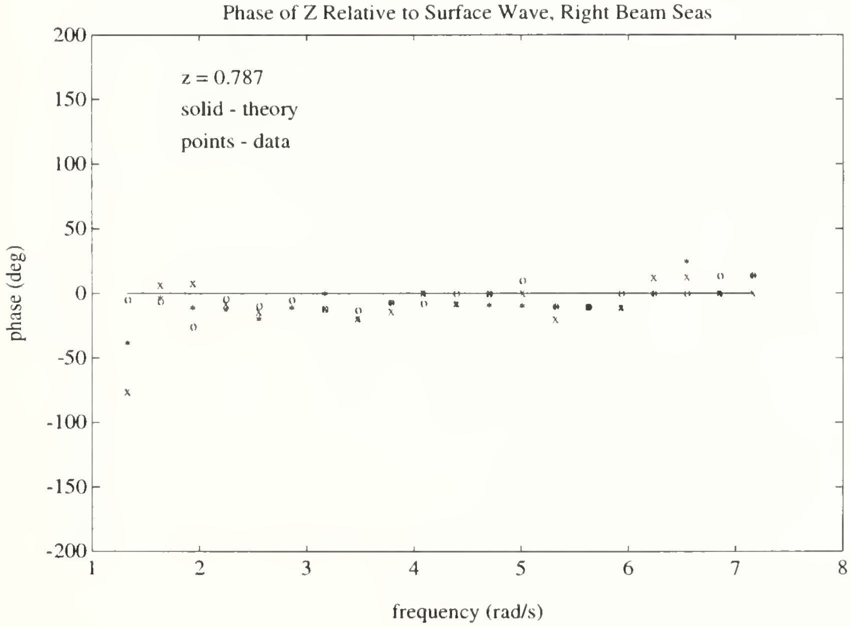

Figure 3.18b Heave Force Transfer Function Phase for Deep Model in Beam Seas

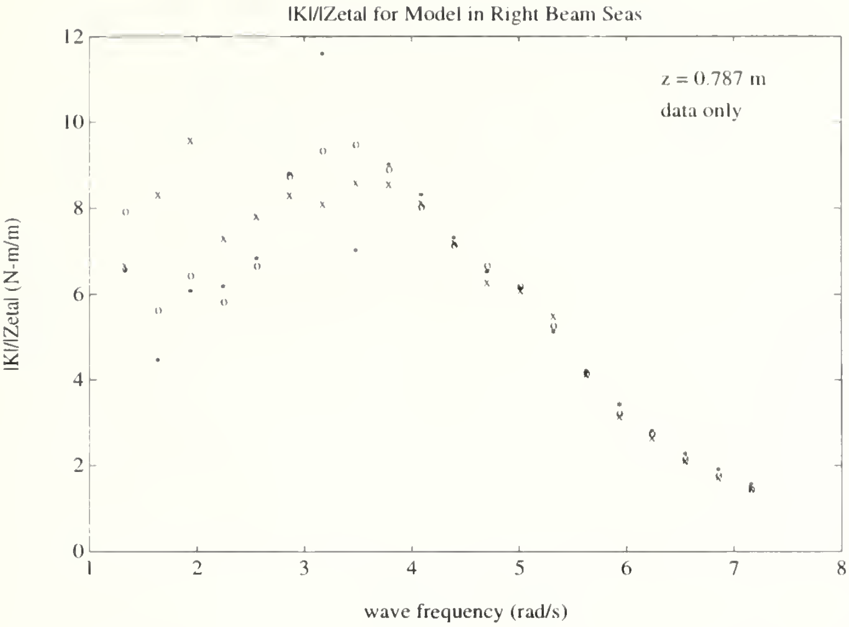

Figure 3.19a Roll Moment Transfer Function Magnitude for Deep Model in Beam Seas

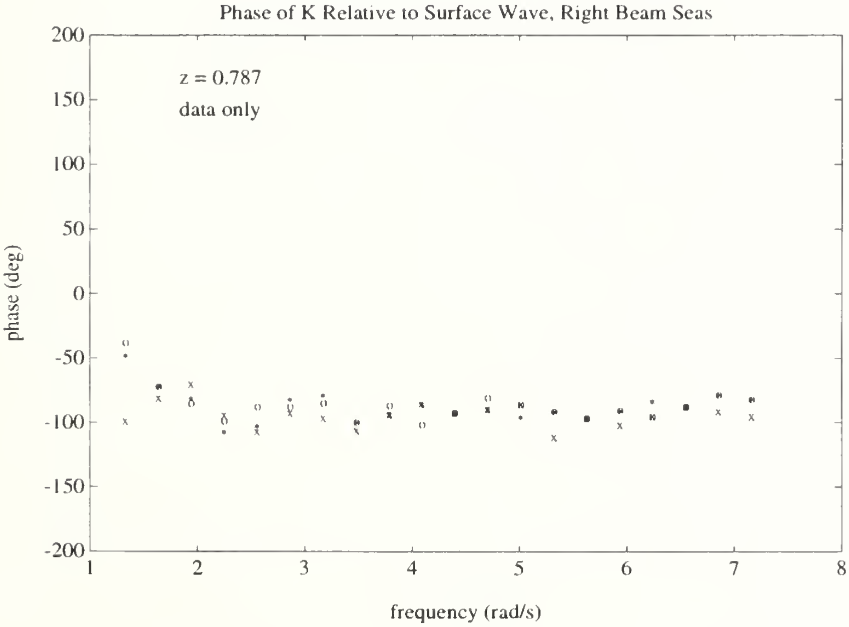

Figure 3.19b Roll Moment Transfer Function Phase for Deep Model in Beam Seas

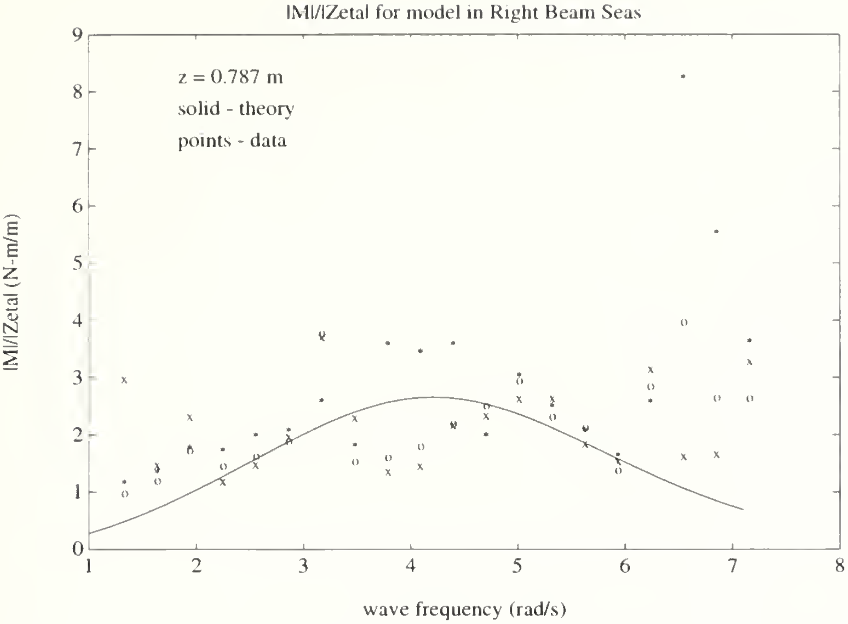

Figure 3.20a Pitch Moment Transfer Function Magnitude for Deep Model in Beam Seas

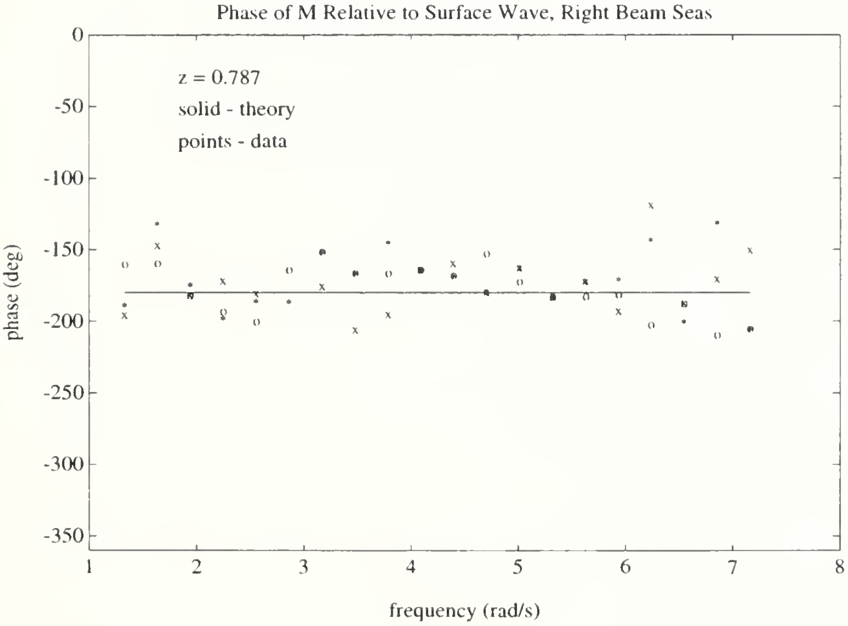

Figure 3.20b Pitch Moment Transfer Function Phase for Deep Model in Beam Seas

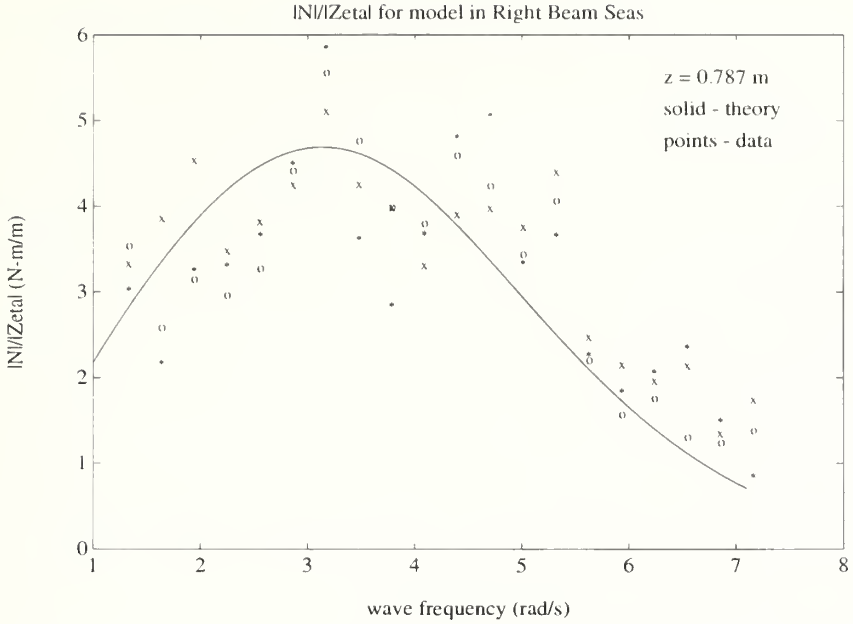

Figure 3.21a Yaw Moment Transfer Function Magnitude for Deep Model in Beam Seas

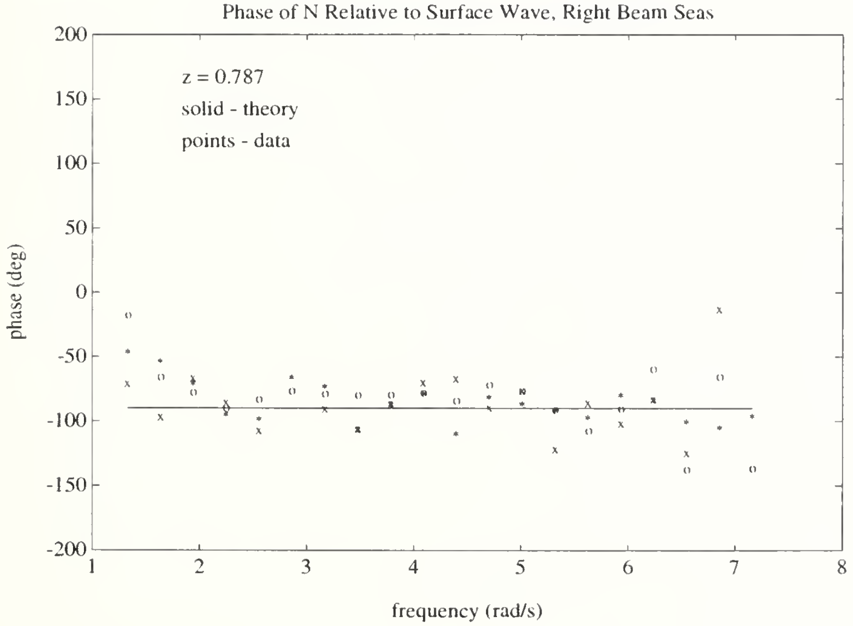

Figure 3.21b Yaw Moment Transfer Function Phase for Deep Model in Beam Seas

3.3.3.3 Forward Moving Model in Head Seas

Figures 3.22 through 3.24 show experimental data depicting transfer function magnitude information for the dynamic components of X, Z and M versus wave frequency for the model at a centerline depth of 0.379 m and 0.489 m/s forward speed. Theoretical curves for the stationary model are plotted with the data for reference. Similarly, figures 3.25 through 3.27 show experimental data for the model at the same depth with a forward speed of 0.733 m/s, with the same theoretical stationary model curves plotted for reference.

Continuous shedding of vortices behind the model is now expected due to the model forward speed. The resulting form drag due to this vortex shedding makes the stationary model theory less applicable. Deviation from the results of the static model testing is clearly seen for X and Z at higher frequencies, and particularly where the zero of the X transfer function was seen at approximately 6 rad/s for the static model AUV. The similarity of the M transfer function magnitude for the static and dynamic AUV cases is noted.

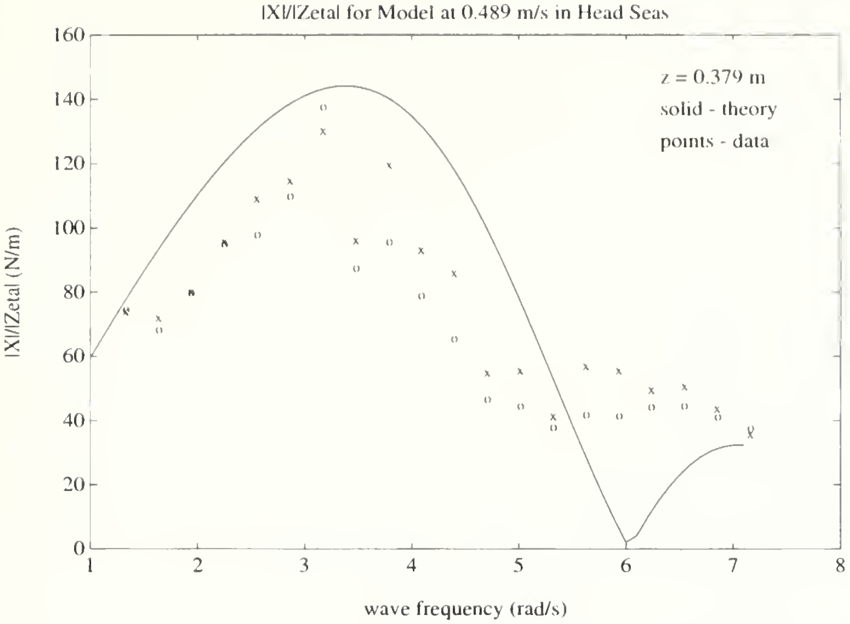

Figure 3.22 Surge Force Transfer Function Magnitude for Model at 0.489 m/s in Head Seas

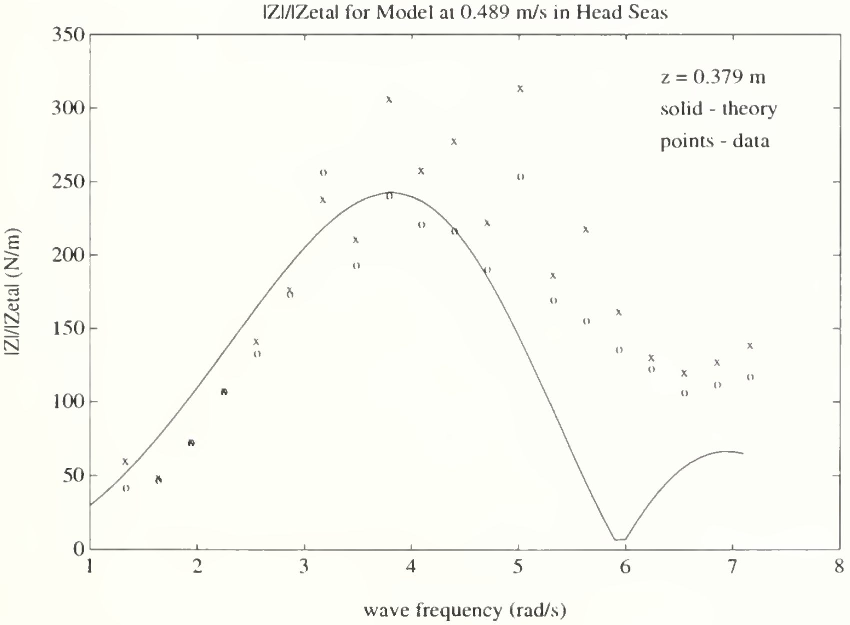

Figure 3.23 Heave Force Transfer Function Magnitude for Model at 0.489 m/s in Head Seas

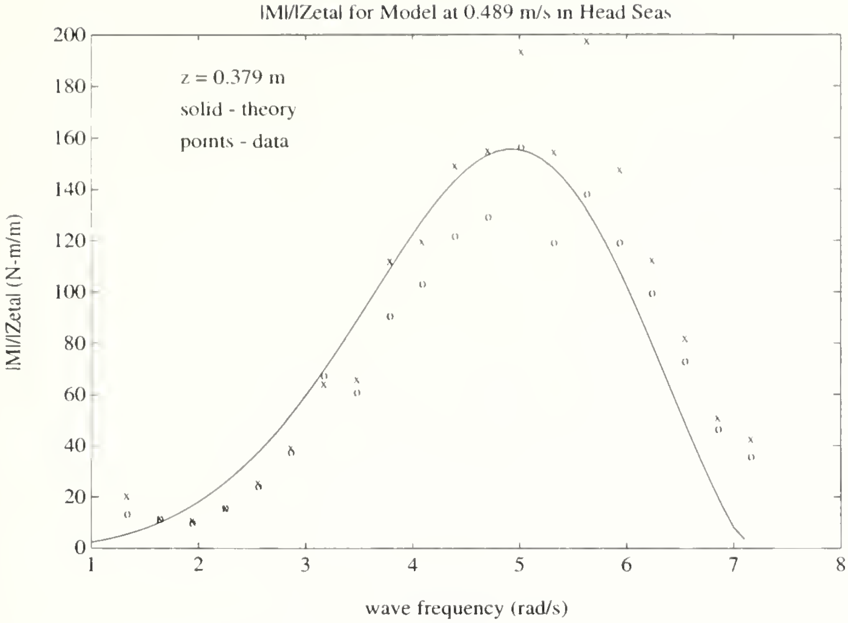

Figure 3.24 Pitch Moment Transfer Function Magnitude for Model at 0.489 m/s in Head Seas

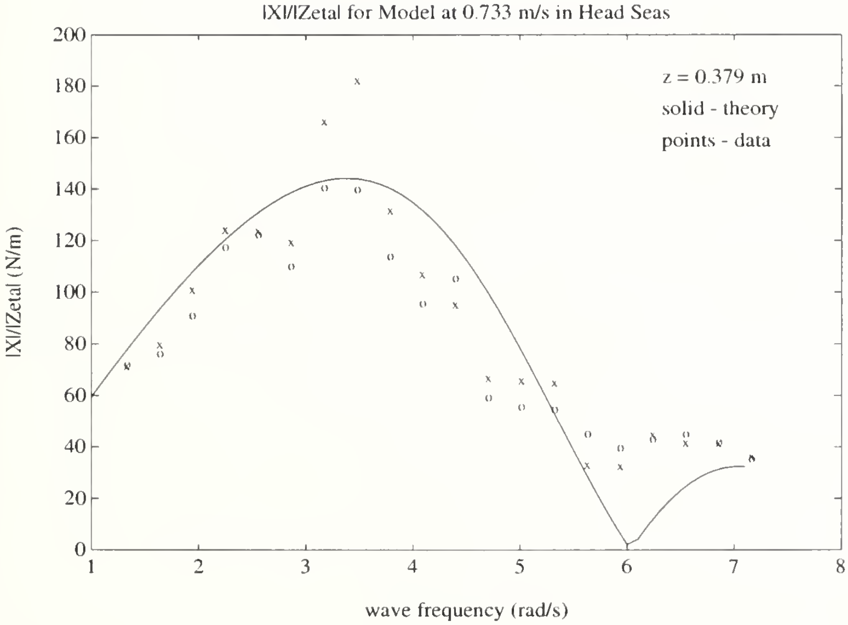

Figure 3.25 Surge Force Transfer Function Magnitude for Model at 0.733 m/s in Head Seas

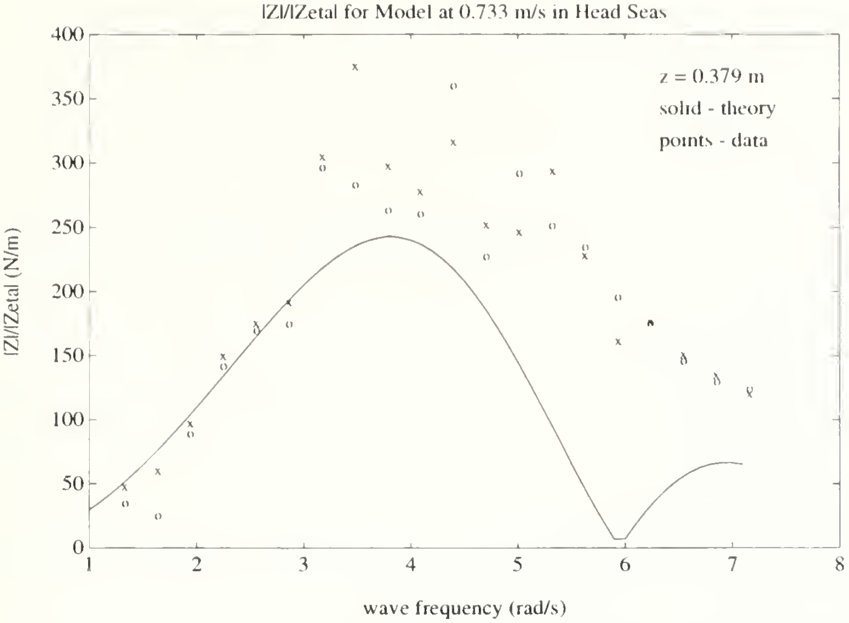

Figure 3.26 Heave Force Transfer Function Magnitude for Model at 0.733 m/s in Head Seas

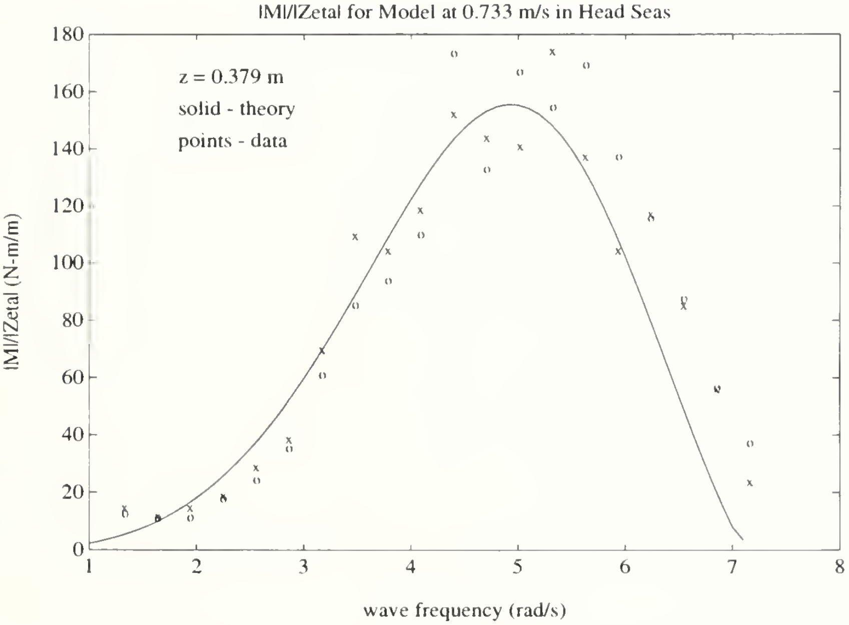

Figure 3.27 Pitch Moment Transfer Function Magnitude for Model at 0.733 m/s in Head Seas

Chapter 4 AUV DYNAMICS

4.1 Equations of Motion

4.1.1 Coordinate Systems

The motion of an AUV in its body reference frame is typically related to its motion in an earth-fixed reference frame versus that of a true inertial frame. For the relatively slow moving ocean vehicle, the neglected motion of the earth's surface is of small consequence.

Figure 4.1 depicts the three ordered rotations, known as Euler angles, which describe the coordinate transformation from the earth-fixed to body-fixed reference frames. To understand the rotations which describe this change in frames, it can be imagined that a body first begins in a neutral earth fixed attitude: facing true north, level with the horizon both to the north and east. To reach the final vehicle attitude, the first rotation is taken about the normal (z) axis, is called yaw and denoted ψ, and can be thought of as a heading change (positive right). The next rotation is pitch, taken about the transverse (y) axis, and is denoted θ (positive nose up). The third and final rotation is roll, taken about the longitudinal (x) axis, and is denoted ϕ (positive right). The order of these rotations is not arbitrary, and taken in a different sequence, could result in a different set of angles for the same final body attitude. All body attitudes, except those including $\theta = \pm 90°$, can be uniquely described by the rotations of the three Euler angles. The singularity associated with $\theta = \pm 90°$ can be avoided by using a four parameter method to

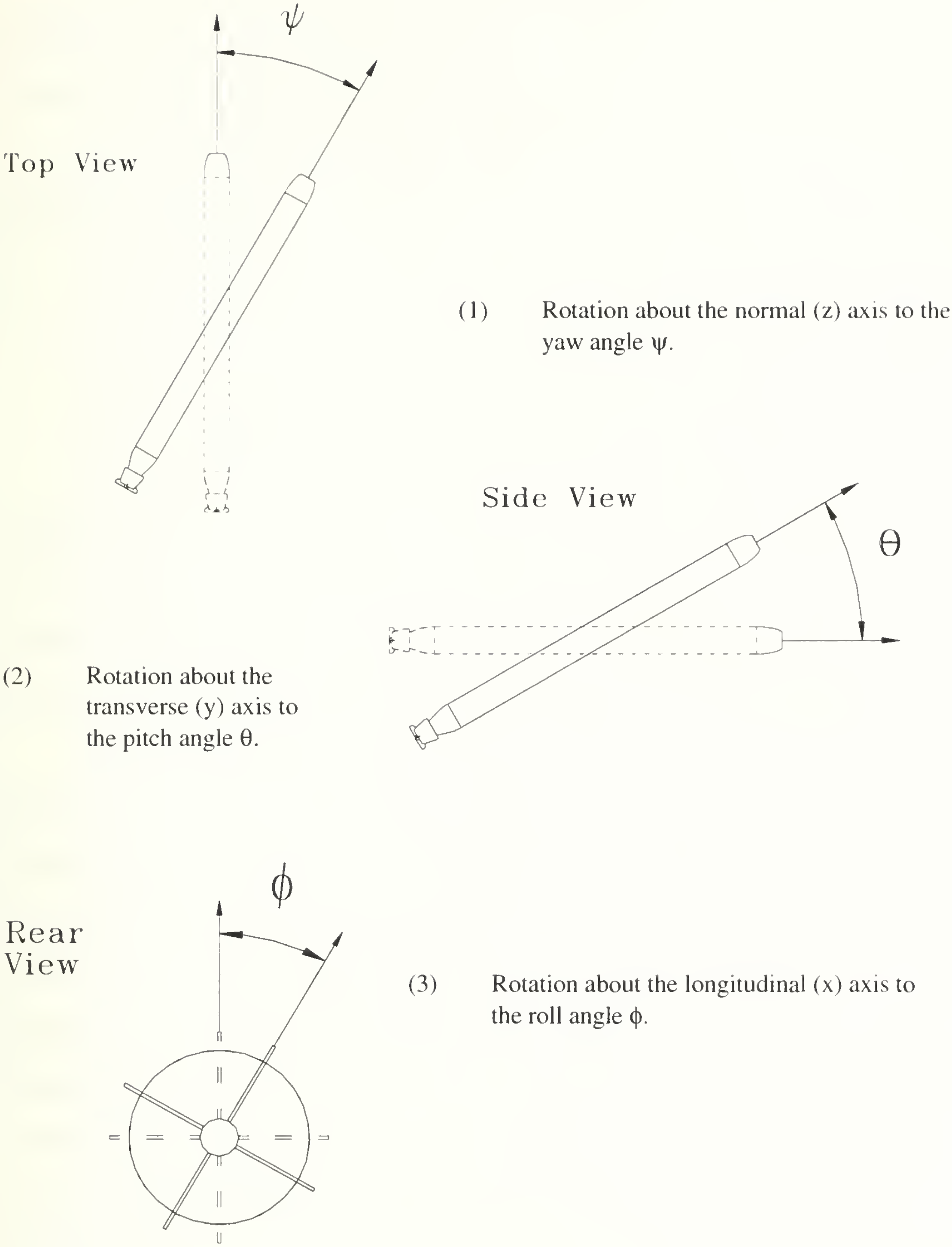
ψ
Top View
Side View
θ
φ
Rear
View

(1) Rotation about the normal (z) axis to the yaw angle ψ.

(2) Rotation about the transverse (y) axis to the pitch angle θ.

(3) Rotation about the longitudinal (x) axis to the roll angle φ.

Figure 4.1 The Euler Angles

describe the three basic rotations, but the natural insight into the body attitude is lost in this approach. For this discussion, $|\theta| < 90°$ is a standing assumption.

Based on the SNAME (1950) notation, the motion of an AUV can then be described with the following vectors:

$$\begin{array}{lll} \eta^T = \begin{bmatrix} \eta_1^T & \eta_2^T \end{bmatrix} & \eta_1^T = \begin{bmatrix} x & y & z \end{bmatrix} & \eta_2^T = \begin{bmatrix} \phi & \theta & \psi \end{bmatrix} \\ \nu^T = \begin{bmatrix} \nu_1^T & \nu_2^T \end{bmatrix} & \nu_1^T = \begin{bmatrix} u & v & w \end{bmatrix} & \nu_2^T = \begin{bmatrix} p & q & r \end{bmatrix} \\ \tau^T = \begin{bmatrix} \tau_1^T & \tau_2^T \end{bmatrix} & \tau_1^T = \begin{bmatrix} X & Y & Z \end{bmatrix} & \tau_2^T = \begin{bmatrix} K & M & N \end{bmatrix} \end{array} \tag{4.1}$$

where η represents position and attitude information which fixes the vehicle in the earth reference frame, ν represents translation and rotation information relative to the body fixed reference frame, and τ represents external forces and moments acting on the AUV in the body reference frame.

The scalars x, y, and z from equations (4.1) represent the vehicle position in an earth fixed, right hand, three dimensional reference frame with the x-axis and y-axis pointing to the horizon, and the z-axis positive downward. The scalars ϕ, θ, and ψ are the previously mentioned Euler angles of roll, pitch, and yaw, respectively. The scalars u, v, and w represent body-fixed reference velocity along the longitudinal axis (surge), the transverse axis (sway), and the normal axis (heave). The scalars p, q, and r refer to right hand rule angular rotation rate about the body longitudinal (x) axis, transverse (y) axis, and normal (z) axis, respectively. The values X, Y, and Z represent forces along the body x, y and z axes respectively. K, M, and N are moments along the axes which would cause positive roll, pitch and yaw, respectively. Table 4.1 summarizes the SNAME notation.

The description of the vehicle's flight path in the earth fixed frame given the body fixed motion is governed by the transformation matrix $\mathbf{J}_1(\eta_2)$, i.e.

DOF	MOTION	FORCES and MOMENTS	LINEAR and ANGULAR VELOCITY (ν)	POSITIONS and EULER ANGLES (η)
1	translation in x (surge)	X	u	x
2	translation in y (sway)	Y	v	y
3	translation in z (heave)	Z	w	z
4	rotation about x-axis (roll)	K	p	ϕ
5	rotation about y-axis (pitch)	M	q	θ
6	rotation about z-axis (yaw)	N	r	ψ

Table 4.1. SNAME Notation Used for Ocean Vehicles

$$\dot{\eta}_1 = \mathbf{J}_1(\eta_2)\nu_1$$

$$\mathbf{J}_1(\eta_2) = \begin{bmatrix} c\psi c\theta & -s\psi c\phi + c\psi s\theta s\phi & s\psi s\phi + c\psi c\phi s\theta \\ s\psi c\theta & c\psi c\phi + s\phi s\theta s\psi & -c\psi s\phi + s\theta s\psi c\phi \\ -s\theta & c\theta s\phi & c\theta c\phi \end{bmatrix} \tag{4.2}$$

where $s(\bullet)$, $c(\bullet)$, and $t(\bullet)$ represent $\sin(\bullet)$, $\cos(\bullet)$, and $\tan(\bullet)$, respectively.

Similarly, the description of the vehicle's earth fixed rotation given the body fixed rotation vector is governed by the transformation matrix $\mathbf{J}_2(\eta_2)$, i.e.

$$\dot{\eta}_2 = \mathbf{J}_2(\eta_2)\nu_2$$

$$\mathbf{J}_2(\eta_2) = \begin{bmatrix} 1 & s\phi t\theta & c\phi t\theta \\ 0 & c\phi & -s\phi \\ 0 & s\phi / c\theta & c\phi / c\theta \end{bmatrix} \tag{4.3}$$

Since each of the two reference frames uniquely maps to the other, it follows that the two transformation matrices are invertible, and the reverse transformations also hold, i.e.

$$\mathbf{v}_1 = \mathbf{J}_1^{-1}(\eta_2)\dot{\eta}_1 \tag{4.4}$$

$$\mathbf{v}_2 = \mathbf{J}_2^{-1}(\eta_2)\dot{\eta}_2 \tag{4.5}$$

are also true.

More generally, it can be written

$$\dot{\eta} = \mathbf{J}(\eta_2)\mathbf{v} \tag{4.6}$$

$$\mathbf{v} = \mathbf{J}^{-1}(\eta_2)\dot{\eta} \tag{4.7}$$

where

$$\mathbf{J}(\eta_2) = \begin{bmatrix} \mathbf{J}_1(\eta_2) & \mathbf{0} \\ \mathbf{0} & \mathbf{J}_2(\eta_2) \end{bmatrix} \tag{4.8}$$

4.1.2 Rigid Body Dynamics

The rigid body equations of motion for an underwater vehicle can be written about an arbitrary origin. When considering an AUV with body symmetry, it is convenient to take the origin as the intersection of the longitudinal, lateral, and normal axes of the body. If the cross moments of inertia about the center of gravity are negligible, then using the parallel axis theorem, the rigid body equations of motion can be expressed as:

$$
\begin{aligned}
m[\dot{u} - vr + wq - x_G(q^2 + r^2) + y_G(pq - \dot{r}) + z_G(pr + \dot{q})] &= X \\
m[\dot{v} - wp + ur - y_G(r^2 + p^2) + z_G(qr - \dot{p}) + x_G(qp + \dot{r})] &= Y \\
m[\dot{w} - uq + vp - z_G(p^2 + q^2) + x_G(rp - \dot{q}) + y_G(rq + \dot{p})] &= Z \\
I_x\dot{p} + (I_z - I_y)qr + m[y_G(\dot{w} - uq + vp) - z_G(\dot{v} - wp + ur)] &= K \\
I_y\dot{q} + (I_x - I_z)rp + m[z_G(\dot{u} - vr + wq) - x_G(\dot{w} - uq + vp)] &= M \\
I_z\dot{r} + (I_y - I_x)pq + m[x_G(\dot{v} - wp + ur) - y_G(\dot{u} - vr + wq)] &= N
\end{aligned} \tag{4.9}
$$

where $\mathbf{r}_G = \begin{bmatrix} x_G & y_G & z_G \end{bmatrix}$ represents the displacement from the origin to the center of gravity. The above equations can be written in the more compact form (Sagatun and Fossen, 1991):

$$\mathbf{M}_{RB}\dot{\boldsymbol{\nu}} + \mathbf{C}_{RB}(\boldsymbol{\nu})\boldsymbol{\nu} = \boldsymbol{\tau}_{RB} \tag{4.10}$$

where
$$\mathbf{M}_{RB} = \begin{bmatrix} m & 0 & 0 & 0 & mz_G & -my_G \\ 0 & m & 0 & -mz_G & 0 & mx_G \\ 0 & 0 & m & my_G & -mx_G & 0 \\ 0 & -mz_G & my_G & I_x & 0 & 0 \\ mz_G & 0 & -mx_G & 0 & I_y & 0 \\ -my_G & mx_G & 0 & 0 & 0 & I_z \end{bmatrix} \tag{4.11}$$

and the Coriolis matrix, though not unique, can be written in a skew symmetric form

$$\mathbf{C}_{RB}(\mathbf{v}) = \begin{bmatrix} 0 & 0 & 0 & m(y_G q + z_G r) & -m(x_G q - w) & -m(x_G r + v) \\ 0 & 0 & 0 & -m(y_G p + w) & m(z_G r + x_G p) & -m(y_G r - u) \\ 0 & 0 & 0 & -m(z_G p - v) & -m(z_G q + u) & m(x_G p + y_G q) \\ -m(y_G q + z_G r) & m(y_G p + w) & m(z_G p - v) & 0 & I_z r & -I_y q \\ m(x_G q - w) & -m(z_G r + x_G p) & m(z_G q + u) & -I_z r & 0 & I_x p \\ m(x_G r + v) & m(y_G r - u) & -m(x_G p + y_G q) & I_y q & -I_x p & 0 \end{bmatrix} \tag{4.12}$$

Here it is worthwhile pointing out that the above relationships are Newton's equations for six degrees of freedom, and that the vector $\tau_{RB} = [X \quad Y \quad Z \quad K \quad M \quad N]^T$ represents all external forces on the vehicle, such as hydrodynamic added mass and damping terms, restoring forces and moments caused by gravity and buoyancy, and any controls and disturbances.

4.1.3 Hydrodynamic Forces

While the rigid body equations of motion can be exactly derived for a given body, the external force vector, τ_{RB}, is usually obtained by using a combination of theoretical and experimental methods, which is to say that an exact solution for τ_{RB} is not available. Fossen (1994) uses the notation

$$\tau_{RB} = \tau_R + \tau_V + \tau_E + \tau_C \tag{4.13}$$

where

τ_R represents the radiation induced forces, and is the vector sum of the hydrodynamic added mass, potential damping and restoring forces,

τ_V is the vector of viscous damping forces

τ_E represents the environmental forces, including those caused by currents and waves, and

τ_C is the vector of control forces, such as those from thrusters and control surfaces.

Then it can be shown that the first term in equation (4.13) can be represented as

$$\tau_R = \underbrace{-\mathbf{M}_A\dot{\boldsymbol{\nu}} - \mathbf{C}_A(\boldsymbol{\nu})\boldsymbol{\nu}}_{\text{added mass and Coriolis}} \quad \underbrace{-\mathbf{D}_P(\boldsymbol{\nu})\boldsymbol{\nu}}_{\text{potential damping}} \quad \underbrace{-\mathbf{g}(\boldsymbol{\eta})}_{\text{restoring forces}} \tag{4.14}$$

Here, the matrices which comprise the added mass and Coriolis terms are represented as

$$\mathbf{M}_A = -\begin{bmatrix} X_{\dot{u}} & X_{\dot{v}} & X_{\dot{w}} & X_{\dot{p}} & X_{\dot{q}} & X_{\dot{r}} \\ Y_{\dot{u}} & Y_{\dot{v}} & Y_{\dot{w}} & Y_{\dot{p}} & Y_{\dot{q}} & Y_{\dot{r}} \\ Z_{\dot{u}} & Z_{\dot{v}} & Z_{\dot{w}} & Z_{\dot{p}} & Z_{\dot{q}} & Z_{\dot{r}} \\ K_{\dot{u}} & K_{\dot{v}} & K_{\dot{w}} & K_{\dot{p}} & K_{\dot{q}} & K_{\dot{r}} \\ M_{\dot{u}} & M_{\dot{v}} & M_{\dot{w}} & M_{\dot{p}} & M_{\dot{q}} & M_{\dot{r}} \\ N_{\dot{u}} & N_{\dot{v}} & N_{\dot{w}} & N_{\dot{p}} & N_{\dot{q}} & N_{\dot{r}} \end{bmatrix} \tag{4.15}$$

and though not unique, $C_A(\nu)$ can be written in the skew symmetric form

$$\mathbf{C}_A(\mathbf{v}) = \begin{bmatrix} 0 & 0 & 0 & 0 & C_A^{15} & C_A^{16} \\ 0 & 0 & 0 & C_A^{24} & 0 & C_A^{26} \\ 0 & 0 & 0 & C_A^{34} & C_A^{35} & 0 \\ 0 & -C_A^{24} & -C_A^{34} & 0 & C_A^{45} & C_A^{46} \\ -C_A^{15} & 0 & -C_A^{35} & -C_A^{45} & 0 & C_A^{56} \\ -C_A^{16} & -C_A^{26} & 0 & -C_A^{46} & -C_A^{56} & 0 \end{bmatrix} \tag{4.16}$$

where

$$C_A^{15} = -X_{\dot{w}}u - Y_{\dot{w}}v - Z_{\dot{w}}w - Z_{\dot{p}}p - Z_{\dot{q}}q - Z_{\dot{r}}r$$

$$C_A^{16} = X_{\dot{v}}u + Y_{\dot{v}}v + Y_{\dot{w}}w + Y_{\dot{p}}p + Y_{\dot{q}}q + Y_{\dot{r}}r$$

$$C_A^{24} = X_{\dot{w}}u + Y_{\dot{w}}v + Z_{\dot{w}}w + Z_{\dot{p}}p + Z_{\dot{q}}q + Z_{\dot{r}}r$$

$$C_A^{26} = -X_{\dot{u}}u - X_{\dot{v}}v - X_{\dot{w}}w - X_{\dot{p}}p - X_{\dot{q}}q - X_{\dot{r}}r$$

$$C_A^{34} = -X_{\dot{v}}u - Y_{\dot{v}}v - Y_{\dot{w}}w - Y_{\dot{p}}p - Y_{\dot{q}}q - Y_{\dot{r}}r$$

$$C_A^{35} = X_{\dot{u}}u + X_{\dot{v}}v + X_{\dot{w}}w + X_{\dot{p}}p + X_{\dot{q}}q + X_{\dot{r}}r$$

$$C_A^{45} = -X_{\dot{r}}u - Y_{\dot{r}}v - Z_{\dot{r}}w - K_{\dot{r}}p - M_{\dot{r}}q - N_{\dot{r}}r$$

$$C_A^{46} = X_{\dot{q}}u + Y_{\dot{q}}v + Z_{\dot{q}}w + K_{\dot{q}}p + M_{\dot{q}}q + M_{\dot{r}}r$$

$$C_A^{56} = -X_{\dot{p}}u - Y_{\dot{p}}v - Z_{\dot{p}}w - K_{\dot{p}}p - K_{\dot{q}}q - K_{\dot{r}}r$$

The potential damping term from equation (4.14), $\mathbf{D}_P(\mathbf{v})\mathbf{v}$, results from the generation of waves on the free surface due to the motion of the AUV, and can therefore be considered negligible when the AUV is sufficiently deep to preclude its generation of waves (Newman 1977). The restoring forces are those caused by the forces of gravity and buoyancy upon the vehicle, and recalling that the z axis is taken positive downward, can be represented

$$\mathbf{g}(\eta) = \begin{bmatrix} (W-B)s\theta \\ -(W-B)c\theta s\phi \\ -(W-B)c\theta c\phi \\ -(y_G W - y_B B)c\theta c\phi + (z_G W - z_B B)c\theta s\phi \\ (z_G W - z_B B)s\theta + (x_G W - x_B B)c\theta c\phi \\ -(x_G W - x_B B)c\theta s\phi - (y_G W - y_B B)s\theta \end{bmatrix} \tag{4.17}$$

where W and B represent the vehicle weight and buoyancy forces, respectively, and $\mathbf{r}_B = \begin{bmatrix} x_B & y_B & z_B \end{bmatrix}$ is the displacement from the origin to the center of buoyancy.

The second term of equation (4.13), representing viscous damping, can be written in the form

$$\tau_V = \underbrace{-\mathbf{D}_V(\nu)\nu}_{\text{viscous damping}} \tag{4.18}$$

where the matrix $\mathbf{D}_V(\nu)$ can be calculated with varying degrees of accuracy by either direct experimentation or the use of published experimental data such as that in (Hoerner 1965, 1975) for similar shaped bodies.

In this discussion, the characterization of the environmental force term, τ_E from equation (4.13), will be restricted to the forces caused by surface waves, and is the subject of chapters 2 and 3. The final term in equation (4.13), the control vector τ_C, is dependent upon the mix of thrusters and / or control surfaces which are available for a specific AUV.

4.1.4 Body Symmetry Considerations

In the above discussion, equations (4.10) and (4.13) taken together provide the general framework for developing the nonlinear, highly coupled equations of motion for an AUV, with

the only assumption thus far being that the cross moments of inertia about the center of gravity are considered negligible. Further exploitation of the symmetry of an AUV body can result in simplified representations of the rigid body mass and Coriolis matrices from equations (4.11) and (4.12), as well as those matrices comprising the hydrodynamic added mass and Coriolis forces, restoring forces, and viscous damping terms.

The top-bottom and left-right symmetry of the 21UUV allows for simplification of the hydrodynamic added mass and Coriolis matrices, namely

$$\mathbf{M}_A = -\begin{bmatrix} X_{\dot{u}} & 0 & 0 & 0 & 0 & 0 \\ 0 & Y_{\dot{v}} & 0 & 0 & 0 & Y_{\dot{r}} \\ 0 & 0 & Z_{\dot{w}} & 0 & Z_{\dot{q}} & 0 \\ 0 & 0 & 0 & K_{\dot{p}} & 0 & 0 \\ 0 & 0 & M_{\dot{w}} & 0 & M_{\dot{q}} & 0 \\ 0 & N_{\dot{v}} & 0 & 0 & 0 & N_{\dot{r}} \end{bmatrix} \tag{4.19}$$

and the same representation for $C_A(\boldsymbol{\nu})$ as in equation (4.16), where now

$$\begin{array}{lll} C_A^{15} = -Z_{\dot{w}}w - Z_{\dot{q}}q & C_A^{16} = Y_{\dot{v}}v + Y_{\dot{r}}r & C_A^{24} = Z_{\dot{w}}w + Z_{\dot{q}}q \\ C_A^{26} = -X_{\dot{u}}u & C_A^{34} = -Y_{\dot{v}}v - Y_{\dot{r}}r & C_A^{35} = X_{\dot{u}}u \\ C_A^{45} = -Y_{\dot{r}}v - N_{\dot{r}}r & C_A^{46} = Z_{\dot{q}}w + M_{\dot{q}}q & C_A^{56} = -K_{\dot{p}}p \end{array} \tag{4.20}$$

(Fossen 1994).

Considering only first order viscous damping terms, the form of $\mathbf{D}_V(\boldsymbol{\nu})$ for this discussion is chosen as

$$\mathbf{D}_V(\nu) = -\begin{bmatrix} X_{u|u|}|u| & 0 & 0 & 0 & 0 & 0 \\ 0 & Y_v & 0 & 0 & 0 & Y_r \\ 0 & 0 & Z_w & 0 & Z_q & 0 \\ 0 & 0 & 0 & K_p & 0 & 0 \\ 0 & 0 & M_w & 0 & M_q & 0 \\ 0 & N_v & 0 & 0 & 0 & N_r \end{bmatrix} \quad (4.21)$$

Also assumed for the remainder of this discussion is that for the 21UUV, $y_G = 0$, which further simplifies $\mathbf{C}_{RB}(\nu)$, $\mathbf{M}_{RB}$, and $\mathbf{g}(\eta)$.

4.2 Model Simplifications

Healy and Marco (1992) suggest that the 6 degree of freedom equations of motion for an AUV can be divided into three non-interacting (or lightly-interacting) sets of equations for control of speed, steering and diving, each involving the state variables:

(1) Speed system state: u(t)
(2) Steering system states: v(t), r(t), ψ(t), x(t) and y(t)
(3) Diving system states: w(t), q(t), θ(t), and z(t)

The rolling mode (p(t) and ϕ(t)) is left passive in this approach for their vehicle, the Naval Postgraduate School AUVII. Their motivation for this approximation is the limited number of actuators on their vehicle, consisting of forward thrusters, stern planes and rudders.

An approach similar to this is currently being used in the development of a sliding controller for a precursor to the 21UUV, the NUWC LDUUV, though the rolling mode is actively

controlled for this vehicle. With this controller design, inner loop pitch and yaw controllers are used to implement desired attitude control action calculated in the outer loop depth and heading controllers, respectively. With this model simplification and accounting for the body symmetry of the LDUUV which is similar in shape to the 21UUV, control of the vehicle in the dive and steering planes are seen as nearly identical problems, the only difference being the restoring forces which act in the dive plane and are absent in the steering plane. The speed system and roll system controllers are somewhat more straightforward to design and implement because of the actuators available on the vehicle (a forward thrust propeller and coordination of the stern and rudder planes as ailerons).

Here, attention is restricted to the longitudinal plane, and the formulation of section 4.1 yield the state equations

$$\begin{aligned}(m - X_{\dot{u}})\dot{u} = {} & (Z_{\dot{w}} - m)wq + (Z_{\dot{q}} + mx_G)q^2 + (mx_G - Y_{\dot{r}})r^2 + \\ & (m - Y_{\dot{v}})vr - mz_G(pr + \dot{q}) + X_{u|u|}|u|u + \\ & (B - W)s\theta + X_d(t) + X_{thr} + \\ & X_{q\delta_s}uq\delta_s + X_{w\delta_s}uw\delta_s + X_{\delta_s^2}u^2\delta_s{}^2\end{aligned} \tag{4.22}$$

$$\begin{aligned}(I_y - M_{\dot{q}})\dot{q} = {} & (I_z - I_x - N_{\dot{r}} + K_{\dot{p}})rp + mz_G(vr - \dot{u} - wq) + \\ & (mx_G + M_{\dot{w}})\dot{w} + (-Z_{\dot{q}} - mx_G)uq + (mx_G - Y_{\dot{r}})vp + \\ & (X_{\dot{u}} - Z_{\dot{w}})uw + (z_B B - z_G W)s\theta + (x_B B - x_G W)c\theta c\phi + \\ & M_w w + M_q q + M_d(t) + M_{\delta_s}u^2\delta_s\end{aligned} \tag{4.23}$$

$$\begin{aligned}(m - Z_{\dot{w}})\dot{w} = {} & (mx_G + Z_{\dot{q}})\dot{q} + Z_q q + Z_w w + (Y_{\dot{v}} - m)vp + \\ & (m - X_{\dot{u}})uq + (Y_{\dot{r}} - mx_G)rp + mz_G(p^2 + q^2) + \\ & (W - B)c\theta c\phi + Z_d(t) + Z_{\delta_s}u^2\delta_s\end{aligned} \tag{4.24}$$

where $X_d(t)$, $Z_d(t)$ and $M_d(t)$ are wave disturbance terms, and X_{thr} and δ_s are the forward thrust and stern plane deflection angle, respectively. By making the further assumptions that

$$\phi(t) = 0 \qquad M_q = M_{uq}u \qquad M_w = M_{uw}u \qquad Z_q = Z_{uq}u \qquad Z_w = Z_{uw}u$$

and eliminating all second order non-longitudinal plane terms yields the decoupled equations which will be used in subsequent discussions:

$$\begin{aligned}(m - X_{\dot{u}})\dot{u} = {} & (Z_{\dot{w}} - m)w\dot{\theta} + (Z_{\dot{q}} + mx_G)\dot{\theta}^2 - mz_G\ddot{\theta} + \\ & X_{u|u|}|u|u + (B - W)s\theta + X_d(t) + X_{thr} + \\ & X_{q\delta_s}uq\delta_s + X_{w\delta_s}uw\delta_s + X_{\delta_s^2}u^2\delta_s{}^2\end{aligned} \tag{4.25}$$

$$\begin{aligned}(I_y - M_{\dot{q}})\ddot{\theta} = {} & -mz_G\dot{u} - mz_G w\dot{\theta} + (mx_G + M_{\dot{w}})\dot{w} + \\ & (M_{uq} - Z_{\dot{q}} - mx_G)u\dot{\theta} + (M_{uw} + X_{\dot{u}} - Z_{\dot{w}})uw + \\ & (z_B B - z_G W)s\theta + (x_B B - x_G W)c\theta + M_d(t) + M_{\delta_s}u^2\delta_s\end{aligned} \tag{4.26}$$

$$\begin{aligned}(m - Z_{\dot{w}})\dot{w} = {} & (mx_G + Z_{\dot{q}})\ddot{\theta} + Z_{uw}uw + (Z_{uq} + m - X_{\dot{u}})u\dot{\theta} + \\ & mz_G\dot{\theta}^2 + (W - B)c\theta + Z_d(t) + Z_{\delta_s}u^2\delta_s\end{aligned} \tag{4.27}$$

$$\dot{z} = w\cos\theta - u\sin\theta \tag{4.28}$$

Chapter 5 CONTROLLER DESIGN AND SIMULATIONS

Sliding control has been used successfully for position and trajectory control of underwater vehicles by Yoerger and Slotine (1985, 1986) with the JASON remotely operated underwater vehicle, Healy and Marco (1992) with the Naval Postgraduate School AUVII, and Hills and Yoerger (1994) with the NUWC LDUUV.

In this chapter, computer simulations are used to investigate the performance of variations of sliding control as applied to the pitch axis of the 21UUV. Robust sliding control routines are first developed for integrated depth, pitch, and forward speed control of the 21UUV, and then an adaptive sliding controller is introduced for the pitch axis. Coordinated control of the 21UUV in the longitudinal plane is demonstrated by simulating the 21UUV making a depth change maneuver. The performance of the adaptive pitch controller in the presence of varying degrees of parametric uncertainty is also demonstrated.

Disturbance cancellation properties of extensions to the adaptive pitch controller is then investigated, using first a monochromatic pitch disturbance of known frequency, and then a stochastic disturbance of known spectrum.

The development of the robust sliding controller and the adaptive sliding controller presented here is found in (Slotine and Li 1991).

5.1 Robust Sliding Control

5.1.1 Overview

The single input dynamic system of the form

$$x^{(n)} = f(\mathbf{x}) + b(\mathbf{x})u \tag{5.1}$$

is considered here, where the scalar x is the output, n is the order of the system and denotes the number of derivatives of x with respect to time, u is the scalar input, and the functions f and b are generally nonlinear functions of the state vector $\mathbf{x} = [x \quad \dot{x} \quad \ldots \quad x^{(n-1)}]^T$ and any other measurable quantity. While the state vector $\mathbf{x}$ is assumed to be known exactly, the function f is not. Rather, the difference between f and its estimate is assumed to have a known bound that is a continuous function of the state and any other measurable quantity, i.e.

$$\left| f - \hat{f} \right| \leq F(\mathbf{x}) \tag{5.2}$$

Similarly, it is assumed that the control gain b is not exactly known, but is of known sign and is bounded by known, continuous functions of **x**.

The desired, realizable state trajectory is denoted $\mathbf{x}_d$, and the trajectory error vector is denoted $\tilde{\mathbf{x}} = \mathbf{x} - \mathbf{x}_d = [\tilde{x} \quad \dot{\tilde{x}} \quad \ldots \quad \tilde{x}^{(n-1)}]^T$. The hyperplane S(t) in the state space $\mathbf{R}^{(n)}$ is defined by

$$s(\mathbf{x};t) = (\tfrac{d}{dt} + \lambda)^{(n-1)}\tilde{x} = 0 \tag{5.3}$$

where λ is a strictly positive constant, and can be interpreted as the control bandwidth of the controller.

Since b has known sign and bounds, and assuming here that b is positive, it can be seen that

$$0 < b_{\min} \leq b \leq b_{\max} \tag{5.4}$$

and that the bounds on b can be written

$$\beta^{-1} \leq \frac{\hat{b}}{b} \leq \beta \tag{5.5}$$

where

$$\hat{b} = (b_{\min} b_{\max})^{1/2} \tag{5.6}$$

and

$$\beta(\mathbf{x}) = (b_{\max}/b_{\min})^{1/2} \tag{5.7}$$

While a control law which maintains $s = 0$ would be ideal, it is also discontinuous across the hyperplane S(t) because of the uncertainties in the dynamic system. Thus, in practice, implementing such a law produces chattering in the control activity which is normally undesirable. To smooth such a discontinuous control law, a boundary layer neighboring the hyperplane can be used, namely

$$\begin{gathered} B(t) = \left\{\mathbf{x}, \quad |s(\mathbf{x};t)| \leq \Phi\right\} \\ \Phi > 0 \end{gathered} \tag{5.8}$$

where the boundary layer thickness, Φ can be made time varying to exploit the bandwidth of the system.

It is shown in (Slotine and Li 1991) that the control law

$$u = \hat{b}^{-1}\left[\hat{u} - \overline{k}\ \mathrm{sat}(s/\Phi)\right] \tag{5.9}$$

where

$$\hat{u} = -\hat{f} - \dot{s} + x^{(n)} \tag{5.10}$$

$$\overline{k} = k(\mathbf{x}) - k(\mathbf{x}_d) + \lambda\Phi/\beta(\mathbf{x}_d) \tag{5.11}$$

and

$$k(\mathbf{x}) = \beta\left[F(\mathbf{x}) + \eta\right] + (\beta - 1)\left|\hat{u}\right| \tag{5.12}$$

with η a small, strictly positive constant, will provide robust stability in the presence of the assumed parametric uncertainty in f and b. The sat (saturation) function of equation (5.9) is given by

$$\begin{array}{lcl} |x| \le 1 & \Rightarrow & \mathrm{sat}(x) = x \\ |x| > 1 & \Rightarrow & \mathrm{sat}(x) = \mathrm{sign}(x) \end{array} \tag{5.13}$$

Boundary layer dynamics are given by

$$\begin{array}{lcl} k(\mathbf{x}_d) \ge \lambda\Phi/\beta(\mathbf{x}_d) & \Rightarrow & \dot{\Phi} = -\lambda\Phi + \beta(\mathbf{x}_d)k(\mathbf{x}_d) \\ k(\mathbf{x}_d) < \lambda\Phi/\beta(\mathbf{x}_d) & \Rightarrow & \dot{\Phi} = -\lambda\Phi/\beta^2(\mathbf{x}_d) + k(\mathbf{x}_d)/\beta(\mathbf{x}_d) \end{array} \tag{5.14}$$

with

$$\Phi(0) = \beta(\mathbf{x}_d)k(\mathbf{x}_d(0))/\lambda \tag{5.15}$$

5.1.2 Application to 21UUV Longitudinal Plane Equations

In the derivation of control laws for the 21UUV, the state vectors η and ν of equation (4.1) are assumed to be measured and known exactly, while $\dot{\nu}$ is assumed unknown but of known bounds.

Considering first 21UUV depth control, from equation (4.28)

$$\ddot{z} = \underbrace{\dot{w}\cos\theta - \dot{u}\sin\theta}_{f_z} \quad \underbrace{-(w\sin\theta + u\cos\theta)}_{b_z} \; \underset{u_z}{\dot{\theta}} \tag{5.16}$$

Then,

$$s_z = \dot{\tilde{z}} + \lambda_z \tilde{z} \tag{5.17}$$

$$\begin{aligned} \hat{f}_z &= 0 \\ F_z &= |\dot{w}|_{\max}\cos\theta + |\dot{u}|_{\max}\sin|\theta| \end{aligned} \tag{5.18}$$

and $\beta_z = 1$.

From equation (5.16) it is seen that the depth control of this AUV is reliant upon its pitch control, which is an intuitive result given the actuators available on the vehicle. Therefore, the resulting control requirement for θ affects not only the pitch angle, but the depth control of the vehicle as well. While $\dot{\theta}_d$ is derived by the depth controller, θ_d and $\ddot{\theta}_d$ are both quantities used in the derivation of the pitch controller. θ_d can be found by numerical integration of $\dot{\theta}_d$, and $\ddot{\theta}_d$ can either be approximated by using a numerical derivative of $\dot{\theta}_d$, or can be uniformly replaced by 0 (with an accompanying decay in performance). Since $\dot{\theta}_d$ is a formulated quantity and is constructed using a smooth control law, taking the numerical derivative of $\dot{\theta}_d$ is a viable option for the derivation of the pitch controller.

The control of the pitch angle is considered next, and from equation (4.26),

$$\ddot{\theta} = f_\theta + b_\theta u_\theta \tag{5.19}$$

where

$$\begin{aligned} f_\theta = (I_y - M_{\dot{q}})^{-1}[&-mz_G\dot{u} - mz_G w\dot{\theta} + (mx_G + M_{\dot{w}})\dot{w} + \\ &(M_{uq} - Z_{\dot{q}} - mx_G)u\dot{\theta} + (M_{uw} + X_{\dot{u}} - Z_{\dot{w}})uw + \\ &(z_B B - z_G W)\sin\theta + (x_B B - x_G W)\cos\theta] \end{aligned} \tag{5.20}$$

$$b_\theta = (I_y - M_{\dot{q}})^{-1} M_{\delta_s} u^2 \tag{5.21}$$

and

$$u_\theta = \delta_s \tag{5.22}$$

The external disturbance due to waves, $M_d(t)$, is assumed to be negligible for the moment.

Then, where the estimates to the hydrodynamic and 21UUV body coefficients are denoted by a ^ ,

$$s_\theta = \dot{\tilde{\theta}} + \lambda_\theta \tilde{\theta} \tag{5.23}$$

$$\begin{aligned} \hat{f}_\theta = (\hat{I}_y - \hat{M}_{\dot{q}})^{-1}[&-\hat{m}\hat{z}_G w\dot{\theta} + (\hat{M}_{uq} - \hat{Z}_{\dot{q}} - \hat{m}\hat{x}_G)u\dot{\theta} + \\ &(\hat{M}_{uw} + \hat{X}_{\dot{u}} - \hat{Z}_{\dot{w}})uw + (\hat{z}_B\hat{B} - \hat{z}_G\hat{W})\sin\theta + \\ &(\hat{x}_B\hat{B} - \hat{x}_G\hat{W})\cos\theta] \end{aligned} \tag{5.24}$$

If the above hydrodynamic and body coefficients are known to within a certain range of values, their estimates can be taken as the algebraic mean of the highest and lowest values, and with $|\dot{u}|_{\max}$ and $|\dot{w}|_{\max}$ known, F_θ can be found from equation (5.2). If this method is used to calculate $\hat{b}_\theta$, equations (5.6) and (5.7) may not hold true, but by using equations (5.5) and (5.21), a conservative value for β_θ can be calculated, and is found to be a constant.

The control of the 21UUV forward speed is considered last, and from equation (4.25)

$$\dot{u} = f_u + b_u u_u \tag{5.25}$$

where

$$\begin{aligned} f_u = (m - X_{\dot{u}})^{-1}\big[&(Z_{\dot{w}} - m)w\dot{\theta} + (Z_{\dot{q}} + m x_G)\dot{\theta}^2 - m z_G \ddot{\theta} + \\ &X_{u|u|}|u|u + (B - W)\sin\theta + X_{q\delta_s} u q \delta_s + X_{w\delta_s} u w \delta_s + X_{\delta_s^2} u^2 {\delta_s}^2\big] \end{aligned} \tag{5.26}$$

$$b_u = (m - X_{\dot{u}})^{-1} \tag{5.27}$$

and

$$u_u = X_{thr} \tag{5.28}$$

Again, the external wave disturbance, $X_d(t)$, is assumed to be negligible for the moment.

Noting that equation (5.25) is of first order,

$$s_u = \tilde{u} \tag{5.29}$$

$$\begin{aligned} \hat{f}_u = (\hat{m} - \hat{X}_{\dot{u}})^{-1}\big[&(\hat{Z}_{\dot{w}} - \hat{m})w\dot{\theta} + (\hat{Z}_{\dot{q}} + \hat{m}\hat{x}_G)\dot{\theta}^2 + \hat{X}_{u|u|}|u|u + \\ &(\hat{B} - \hat{W})\sin\theta + \hat{X}_{q\delta_s} u q \delta_s + \hat{X}_{w\delta_s} u w \delta_s + \hat{X}_{\delta_s^2} u^2 {\delta_s}^2\big] \end{aligned} \tag{5.30}$$

and with $\left|\ddot{\theta}\right|_{\max}$ assumed known, F_u can be found. Again, a conservative value of β_u can be calculated and is found to be a constant.

With the completion of the above formulation, the choice of λ_θ and λ_z remains. Guidance for the selection of sliding controller bandwidth is given in (Slotine and Li 1991) with concern for structural resonant modes, neglected time delays, and sampling rates addressed.

While unmodeled sternplane actuator dynamics may determine a reasonable choice for λ_θ, the value of λ_z becomes dependent upon that of λ_θ. Because the outer loop depth controller develops the desired inner loop pitch rate and angle, $\lambda_z \leq \lambda_\theta/4$ is used so that λ_θ may be neglected when considering the equation of motion for z.

5.2 Adaptive Sliding Control

5.2.1 Application to 21UUV Pitch Equation

Another approach to developing control laws in the presence of parametric uncertainty associated with the hydrodynamic and body coefficients of the equations in section 4.2 is to use a model based adaptive sliding controller. Where it was previously assumed in section 5.1.2 that the parameters in equations (4.25) through (4.27) are possibly time varying but bounded by upper and lower limits, the use of an adaptive sliding controller assumes no known bounds on the 21UUV equation coefficients, but rather that the coefficients remain constant.

Because pitch control is critical not only to the attitude but also to the depth control of the 21UUV, the application of adaptive sliding control will be presented here for the pitch equation.

Equation (4.26) can be written

$$a_1\ddot{\theta} + a_2 w\dot{\theta} + a_3 u\dot{\theta} + a_4 wu + a_5 \sin\theta + a_6 \cos\theta + d_1(t) + d_0 M_d(t) = -u^2\delta_s \qquad (5.31)$$

where

$$a_1 = \frac{I_y - M_{\dot{q}}}{-M_{\delta_s}} \qquad a_2 = \frac{m z_G}{-M_{\delta_s}} \qquad a_3 = \frac{Z_{\dot{q}} + m x_G - M_{uq}}{-M_{\delta_s}}$$

$$a_4 = \frac{Z_{\dot{w}} - X_{\dot{u}} - M_{uw}}{-M_{\delta_s}} \qquad a_5 = \frac{z_G W - z_B B}{-M_{\delta_s}} \qquad a_6 = \frac{x_G W - x_B B}{-M_{\delta_s}} \tag{5.32}$$

$$d_0 = \frac{1}{-M_{\delta_s}} \qquad d_1(t) = \frac{m x_G + M_{\dot{w}}}{M_{\delta_s}} \dot{w} - \frac{m z_G}{M_{\delta_s}} \dot{u}$$

Estimates of the values of the above hydrodynamic and body coefficients can be obtained through experimentation or the use of published experimental data such as that in (Hoerner 1965, 1975) for similar shaped bodies. Then if $|\dot{w}|_{\max}$ and $|\dot{u}|_{\max}$ are known, D such that $|d_1|_{\max} < D$ can also be conservatively estimated, where for the moment, $M_d(t)$ is considered negligible.

Using the adaptive sliding pitch controller developed in the appendix yields the control and adaptation laws

$$\begin{aligned} \delta_s &= u^{-2}(k_\theta s_\theta - \mathbf{Y}\hat{\mathbf{a}}) \\ \dot{\hat{\mathbf{a}}} &= -\mathbf{\Gamma}\mathbf{Y}^T s_{\theta\,\Delta} \end{aligned} \tag{5.33}$$

where

$$\begin{aligned} \mathbf{Y} &= \begin{bmatrix} \ddot{\theta}_d - \lambda_\theta \dot{\tilde{\theta}} & w\dot{\theta} & u\dot{\theta} & wu & \sin\theta & \cos\theta \end{bmatrix} \\ \hat{\mathbf{a}} &= \begin{bmatrix} \hat{a}_1 & \hat{a}_2 & \hat{a}_3 & \hat{a}_4 & \hat{a}_5 & \hat{a}_6 \end{bmatrix}^T \\ \mathbf{\Gamma}^{-1} &= \mathbf{\Gamma}^{-T} > 0 \\ s_{\theta\,\Delta} &= s_\theta - \Phi_\theta \operatorname{sat}(s_\theta/\Phi_\theta) \end{aligned} \tag{5.34}$$

and k_θ is such that

$$k_\theta \Phi_\theta \geq D \tag{5.35}$$

As noted above, the adaptation gain matrix, Γ, is symmetric and positive definite. In practice, a diagonal matrix with strictly positive entries can be selected which allows for easy tuning of the adaptation gain for each parameter estimate, $\hat{a}_i$, individually.

The adaptive sliding controller presented here, and referred to in later discussion, uses a time invariant boundary layer, Φ. Slotine and Coetsee (1986) present similar results for the adaptive sliding controller with a time varying boundary layer, $\Phi(t)$.

By comparing the laws for robust sliding pitch control and adaptive sliding pitch control, similarities can be seen. For the case when s remains inside its boundary layer, reformulating the robust sliding control law results in

$$\delta_s = u^{-2}\left(\underbrace{\hat{a}_1 \frac{\bar{k}}{\Phi_\theta}}_{k_{\theta eff}(t)} s - \mathbf{Y}\hat{\mathbf{a}} \right) \qquad s \leq \Phi_\theta \tag{5.36}$$

which can be compared to equation (5.33). The on-line adjustment of $k_{\theta eff}$ using the laws given in section 5.1.1 for the robust sliding controller allows for better exploitation of the control "bandwidth" available (Slotine and Li 1991).

5.2.2 Adaptive Wave Disturbance Cancellation

Notwithstanding the stochastic nature of ocean water waves and the development of chapters 2 and 3, first considered is the case where the 21UUV is operating under a sea dominated by regular waves of a single known frequency, ω, with unknown phase and amplitude. Then it is seen that the wave disturbance term in equation (5.31) can be written

$$d_0 M_d(t) = a_7 \sin(\omega t) + a_8 \cos(\omega t) \tag{5.37}$$

and by the addition of wave disturbance cancellation terms to $\mathbf{Y}$ and corresponding coefficient estimates to $\hat{\mathbf{a}}$ in equations (5.33) and (5.34), namely

$$\begin{aligned} \mathbf{Y} &= \begin{bmatrix} \ddot{\theta}_d - \lambda_\theta \dot{\tilde{\theta}} & w\dot{\theta} & u\dot{\theta} & wu & \sin\theta & \cos\theta & \sin\omega t & \cos\omega t \end{bmatrix} \\ \hat{\mathbf{a}} &= \begin{bmatrix} \hat{a}_1 & \hat{a}_2 & \hat{a}_3 & \hat{a}_4 & \hat{a}_5 & \hat{a}_6 & \hat{a}_7 & \hat{a}_8 \end{bmatrix}^T \end{aligned} \tag{5.38}$$

the adaptive cancellation of the single frequency wave disturbance is possible.

In an attempt to extend the above idea to better cancel the disturbance caused by random water waves, additional disturbance cancellation terms which span some portion of the spectrum of the stochastic disturbance can be added to $\mathbf{Y}$. While robust stability and performance guarantees can no longer be provided as they were previously, a potential improvement in pitch performance seems likely under at least some conditions, and this idea will be investigated.

5.3 Simulation Results

Simulation results are presented here which demonstrate the performance of the two variations of sliding control presented in sections 5.1 and 5.2. In all cases, the simplified, coupled 21UUV longitudinal plane equations ((4.25) through (4.28)) are used.

5.3.1 Additional Modeling Considerations

In the derivation of the longitudinal plane dynamic equations for the 21UUV, and subsequently during the controller design, no regard was given to actuator dynamics. For simulation purposes here, both the main thruster and sternplanes are modeled as first order systems which saturate, as depicted in figure 5.1.

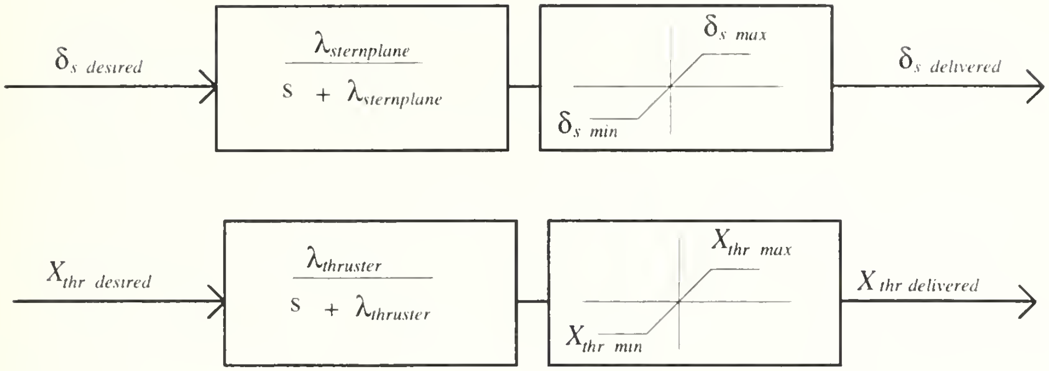
$\delta_{s\ desired}$
$\frac{\lambda_{sternplane}}{s + \lambda_{sternplane}}$
$\delta_{s\ max}$
$\delta_{s\ min}$
$\delta_{s\ delivered}$
$X_{thr\ desired}$
$\frac{\lambda_{thruster}}{s + \lambda_{thruster}}$
$X_{thr\ max}$
$X_{thr\ min}$
$X_{thr\ delivered}$

Figure 5.1 Sternplane and Thruster Dynamics Model

Another modeling consideration previously ignored is that the moment produced by the sternplanes grows with time until reaching its final value, $M_{\delta_s} u^2 \delta_s$. The *Wagner* or '*growth of lift*' function given in (Woods 1961) can be used to describe the lift dynamics. To develop 90% of the final lift, the sternplanes must travel approximately 6 chord lengths (Newman 1977).

For the 0.1 meter chord length 21UUV sternplane at 2 m/s, 90% lift is generated in about 0.3 seconds. Equating this time to twice the time constant of a first order linear system results in an approximate bandwidth of 6.7 rad/sec. Since this bandwidth is somewhat greater than that assumed for the sternplane actuators, the lift dynamics are ignored for the purpose of these modeling considerations.

Table 5.1 contains nominal values of the body, hydrodynamic, controller, and actuator coefficients used in the simulations. The values for the body and hydrodynamic coefficients were derived using strip theory and assuming the vehicle is neutrally buoyant. For hydrodynamic actuator constants (those with a δ_s subscript) and values of the centers of buoyancy and gravity, the values provided by NUWC for the LDUUV are used.

Body Coefficients		Hydrodynamic Coefficients			
m	1619 kg	M_{uw}	849 kg	Z_{uq}	-770.4 kg
W	15882 N	M_{uq}	-3066 kg-m	Z_{δ_s}	-99.3 kg/m
B	15882 N	$M_{\dot{q}}$	-7255 kg-m^2	$X_{\dot{u}}$	-41.5 kg
I_y	7100 kg-m^2	$M_{\dot{w}}$	121.5 kg-m	$X_{u\lvert u\rvert}$	-16.9 kg/m
x_G	2×10^{-6} m	M_{δ_s}	-355.1 kg	$X_{q\delta_s}$	-55.3 kg
z_G	0.005 m	$Z_{\dot{q}}$	121.5 kg-m	$X_{w\delta_s}$	-16.1 kg/m
x_B	0 m	$Z_{\dot{w}}$	-1619 kg	$X_{\delta_s^2}$	-36.7 kg/m
z_B	0 m	Z_{uw}	-201.5 kg/m		

Controller Constants		Actuator Constants			
λ_z	0.125	$\lambda_{sternplane}$	4	$\lambda_{thruster}$	0.5
$\lambda_\theta, \lambda_u$	0.5	$\delta_{s\ max}$	30°	$\delta_{s\ min}$	-30°
$\eta_z, \eta_\theta, \eta_u$	0.01	$X_{thr\ max}$	650 N	$X_{thr\ min}$	0 N
Γ_0	diag[4000, 10, 1, 100, 1, 0.1]				

Table 5.1 Nominal Body, Hydrodynamic, Controller and Actuator Parameters

Unless otherwise stated, it is assumed that the body coefficients of table 5.1 are known to within 5% error (estimated coefficients are within 5% of the nominal coefficients), and that the hydrodynamic coefficients are known to within 30% error. Actual values of the hydrodynamic and body coefficients used for simulation dynamics are those of the nominal values. Estimated values of the hydrodynamic coefficients used by the robust sliding controllers in their model of the 21UUV dynamics are 130% of the nominal values except for added mass terms ($X_{\dot{u}}$, $M_{\dot{q}}$, $M_{\dot{w}}$, $Z_{\dot{q}}$, and $Z_{\dot{w}}$) which are 70% of the nominal values. Similarly, estimated values of the body coefficients are 105% of the nominal values except for the inertia terms (m and I_y) which are 95% of the nominal values.

Adaptive sliding controller initial estimates for $\hat{\mathbf{a}}$ vary and are detailed with each associated simulation.

Simulation results for the conditions investigated here have indicated the following estimates for bounds on maximum accelerations:

$$|\dot{w}|_{\max} < 0.2 \text{ m/s}^2, \quad |\dot{u}|_{\max} < 0.2 \text{ m/s}^2, \quad |\ddot{\theta}|_{\max} < 0.1 \text{ deg/s}^2 \tag{5.39}$$

Then from equations (5.32) and (5.39), it can be seen that $|d_1(t)|_{\max} < D = 0.08$.

5.3.2 Depth Trajectory Following

Figures 5.2, 5.3, and 5.4 show simulation results of the 21UUV making a 10 meter depth change with the three integrated robust sliding controllers developed in section 5.1.2 controlling depth, pitch, and forward speed. Despite parametric uncertainty, depth trajectory following is good, and provides a baseline against which subsequent simulation results can be compared. Figure 5.5 depicts $k_{\theta_{eff}}(t)$ for the robust sliding pitch controller during the depth maneuver.

By comparison, figures 5.6 and 5.7 show simulation results of the 21UUV making an equivalent depth maneuver with the same depth and speed controllers, but with the pitch control law from equation (5.33). With $\mathbf{\Gamma} = \mathbf{0}$, no parametric adaptation occurs, i.e. $\hat{\mathbf{a}} = \hat{\mathbf{a}}(0)$. The parameter estimates are calculated using the same body and hydrodynamic coefficient estimates used in the previous simulation. This pitch controller is tuned to have approximately the same feedback gain, k_θ, as that of the robust sliding controller demonstrated in figure 5.3. With $k_\theta = 7 \approx k_{\theta_{eff}}(t)$, depth and pitch control depicted in figures 5.6 and 5.7 closely match those of figures 5.2 and 5.3. Speed control, while also nearly identical to the previous case, is of secondary interest, and is not depicted in this nor subsequent simulations.

Figures 5.8 and 5.9 depict the same depth maneuver as in the previous cases with the pitch control law from equation (5.33), and with $\Gamma = \Gamma_0$ from table 5.1. All other conditions from the previous simulation remain the same. The resulting parameter adaptation is seen to have a positive effect upon the pitch and resulting depth control of the vehicle. Figure 5.10 depicts the adaptation of the vector $\hat{\mathbf{a}}$ shown with the parameter s_θ and its boundary layer Φ_θ. Convergence of the parameter estimates to the values they estimate is not observed, nor is it necessarily expected. Narendra and Annaswamy (1989) and Slotine and Li (1991) both provide a thorough discussion concerning the condition of *persistent excitation* under which parameter estimates do converge to their target values.

Next considered is the performance of the adaptive pitch controller in the presence of more substantial parametric uncertainty. It is now assumed that the hydrodynamic coefficients from table 5.1 are totally unknown, with the lone exception of M_{δ_s}, which is still assumed to be known to within 30% error. Dry body coefficients are assumed known to within 5% error as before. For the initial estimate of the adaptive controller parameter vector $\hat{\mathbf{a}}$, the previous estimated values of the body coefficients and M_{δ_s} are used, with the remainder of the hydrodynamic coefficient initially estimated to be 0. Actual values of the hydrodynamic and body coefficients used for simulation dynamics remain unchanged.

Figures 5.11 and 5.12 show simulation results of the 21UUV attempting the 10 meter depth change with robust sliding depth and speed controllers, and the pitch control law from equation (5.33) with no adaptation. As illustrated, this control scheme is unstable. By comparison, figures 5.13 and 5.14 illustrate the beneficial effect of adaptation for the same initial conditions. Pitch control is shown to be stable, leading to good depth trajectory following. Figures 5.15 and 5.10 can be compared to see the effect of the added initial parametric uncertainty on the adaptation of the vector $\hat{\mathbf{a}}$.

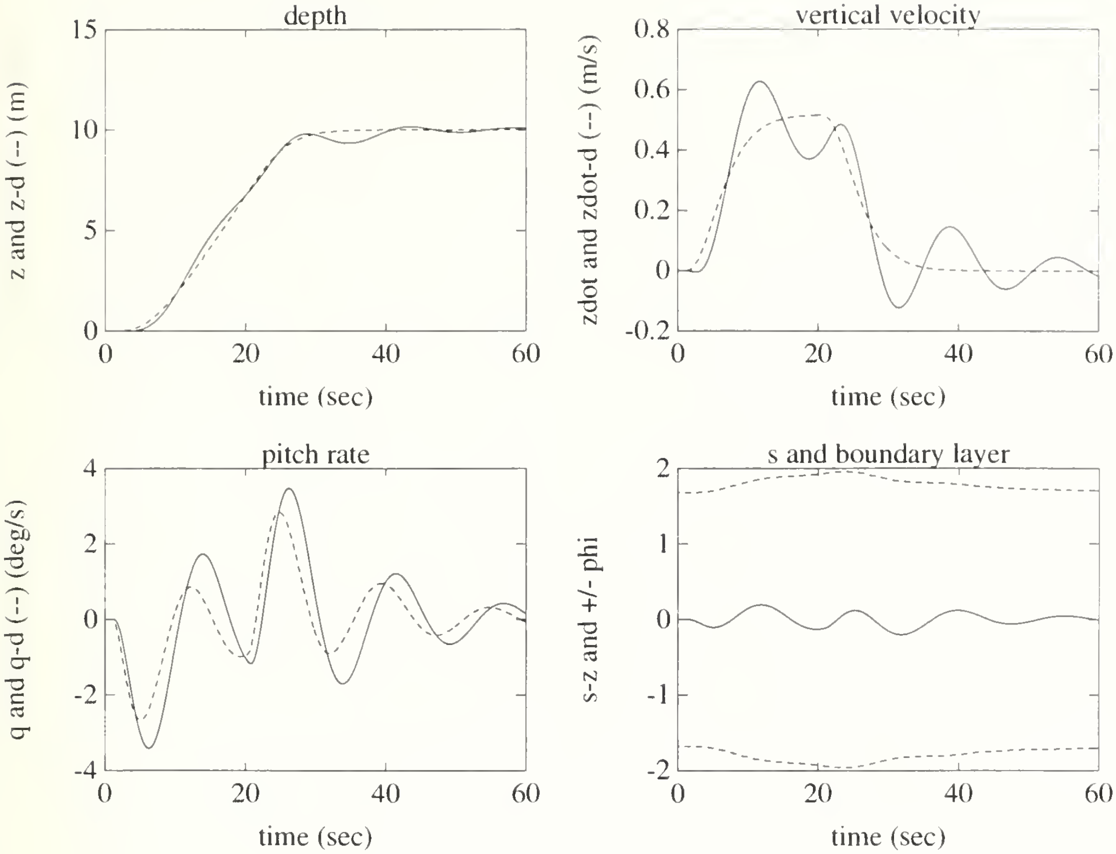

Figure 5.2 21UUV Depth Trajectory with Robust Sliding Pitch Controller. Depicted (clockwise from top left) are (1) desired and simulated vehicle depth, (2) desired and simulated vertical velocity, (3) desired and simulated pitch rate, which is the control variable used in the depth equation, and (4) the generalized error parameter, s_z, and its boundary layer, Φ_z. It is seen that despite substantial parametric uncertainty, good depth trajectory following is achieved. Note that s_z remains well bounded by Φ_z, which is a design feature of the robust sliding controller, and indicates that the resulting vehicle depth trajectory is maintained within the expected bounds of performance given the level of parametric uncertainty present.

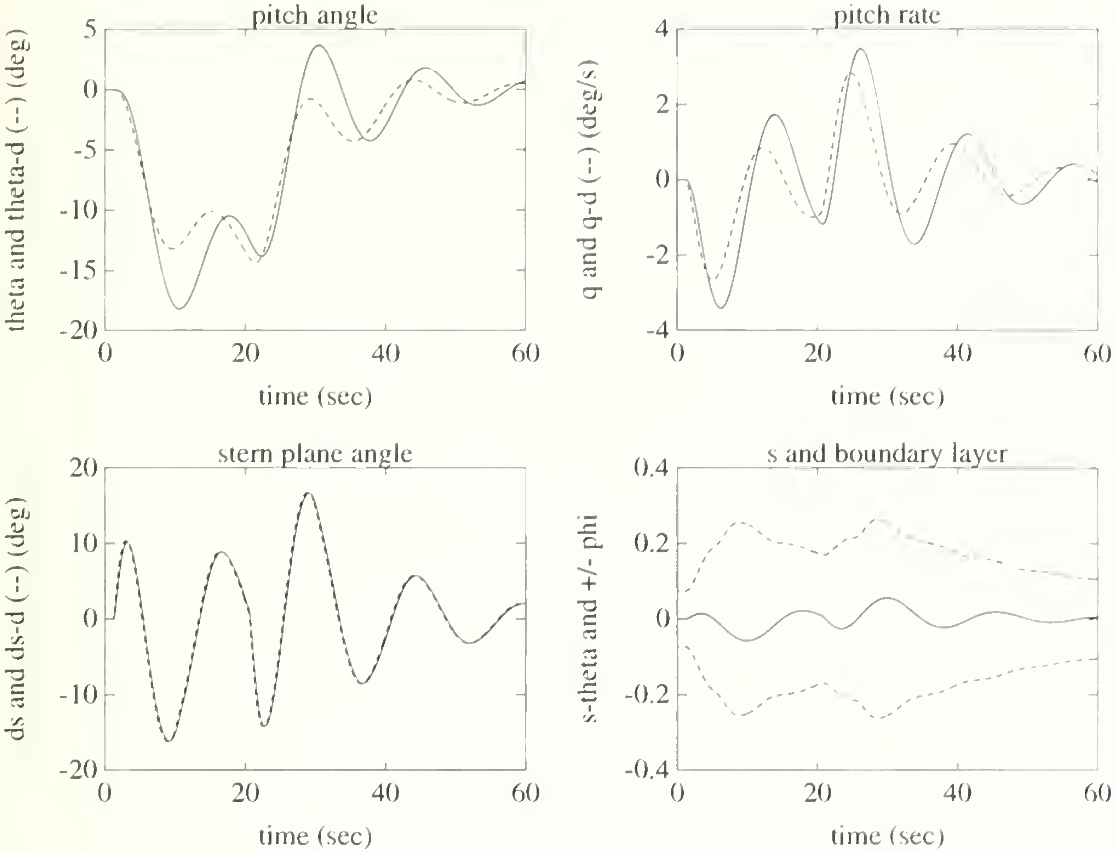

Figure 5.3 21UUV Pitch Response During Depth Maneuver. Here, the desired pitch rate is generated during the simulation by the depth controller, and the robust sliding pitch controller provides sternplane commands to follow the generated pitch trajectory. The sternplane is seen to remain within its saturation limits, and because of the high bandwidth of the sternplane actuator, sternplane angle follows the desired values closely. As in the case of the z controller, the error parameter, s_θ remains bounded by Φ_θ.

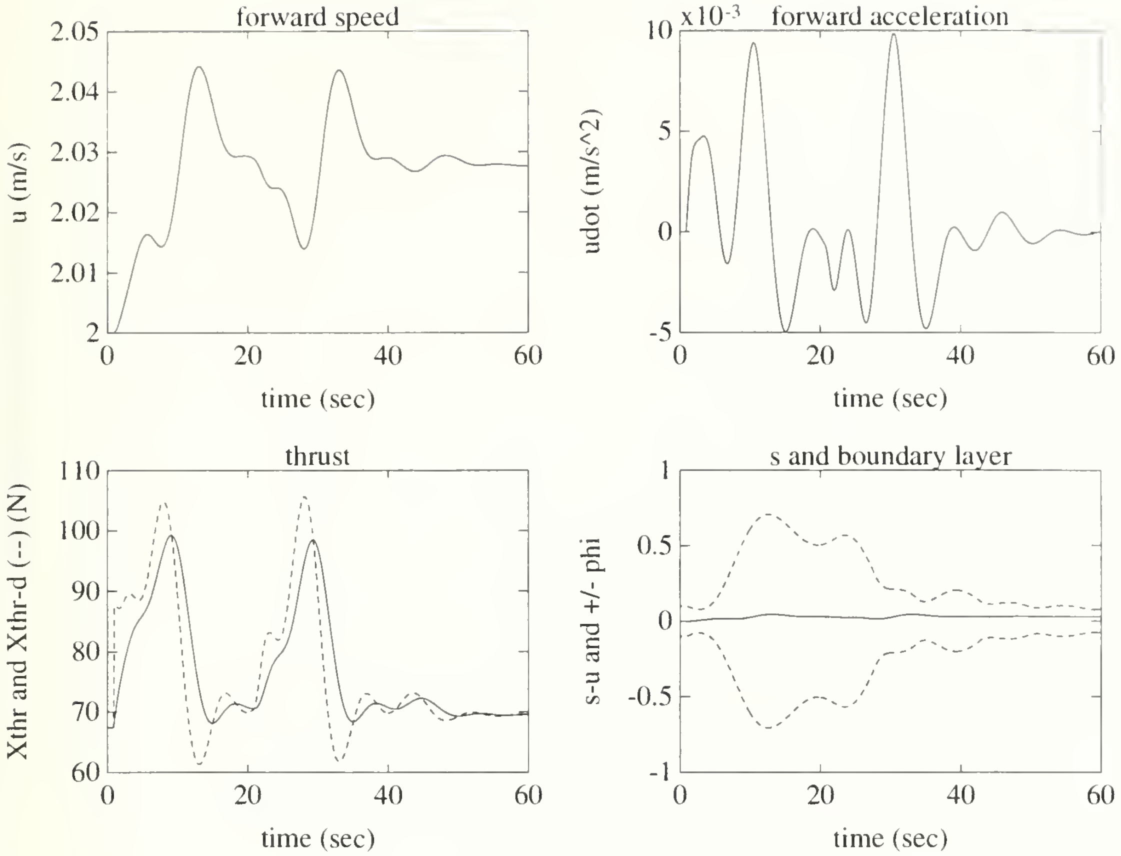

Figure 5.4 21UUV Speed Response During Depth Maneuver. The forward speed controller here attempts to regulate the vehicle at 2 m/s during the change in vehicle depth. The steady state forward speed error seen at the end of the run is due to the parametric error in the estimated constants that the controller uses in its speed model. The effect of thruster dynamics are seen as delivered thrust varies from desired thrust. As in the previous two cases, s_u remains bounded by Φ_u.

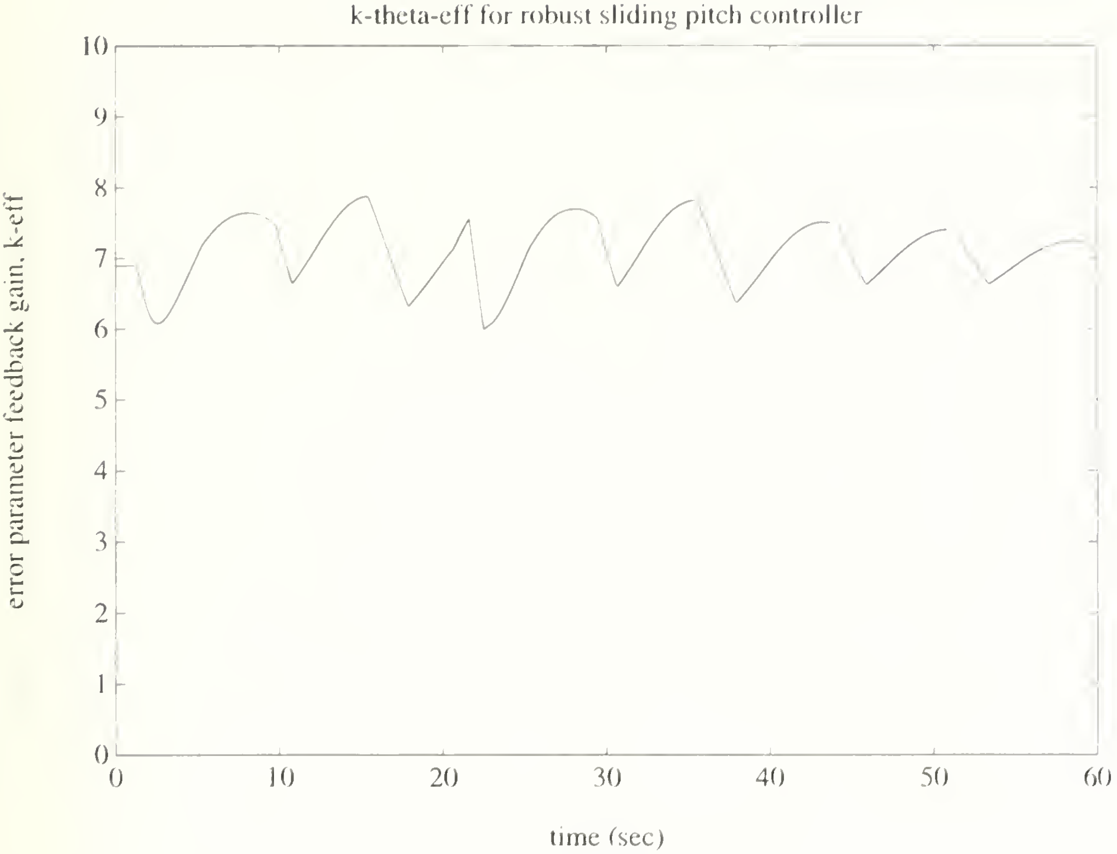

Figure 5.5 Robust Sliding Pitch Controller $k_{\theta eff}(t)$. Though $k_{\theta eff}$ varies with time, it is seen that $k_{\theta eff} \approx 7$ for the duration of this depth change maneuver.

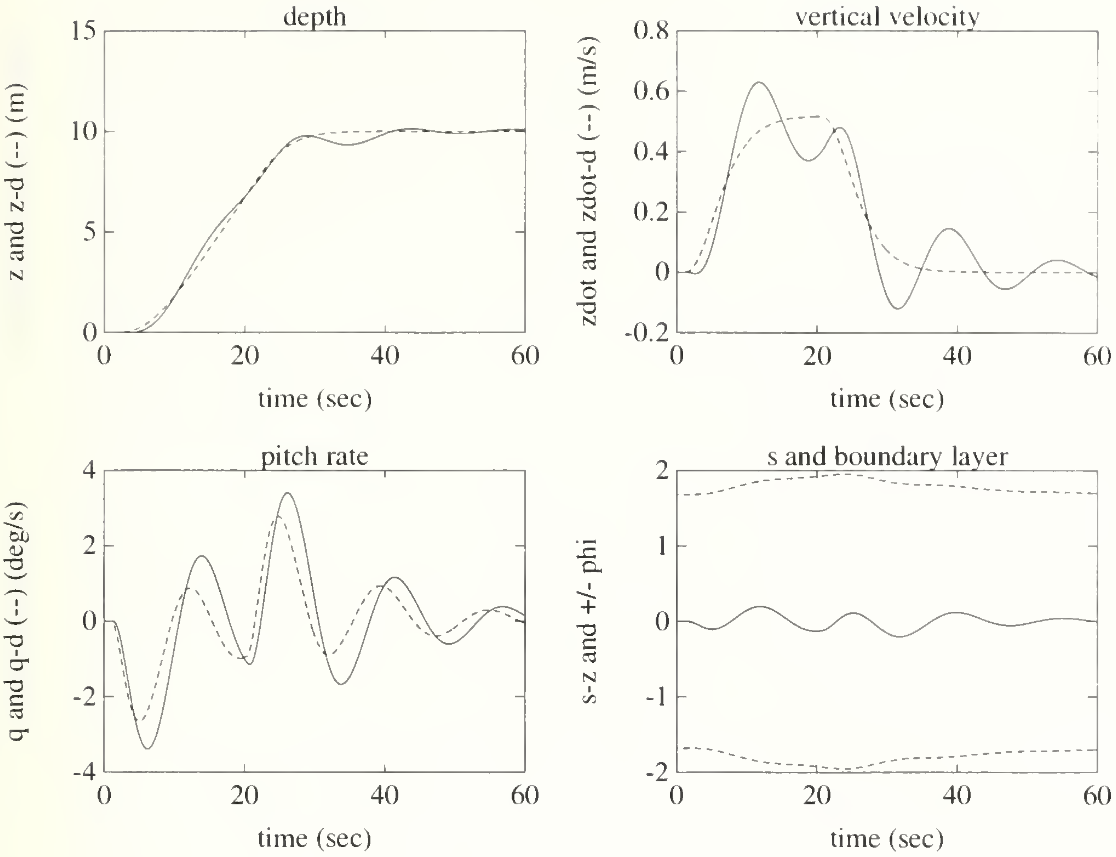

Figure 5.6 21UUV Depth Trajectory with Adaptive Sliding Pitch Control Law, $\Gamma = \mathbf{0}$. Here, the pitch control law from equation (5.33) is used with no adaptation of parameter estimates. This pitch controller is very similar to the robust sliding controller used previously, differing only in that the feedback gain $k_{\theta eff}(t)$ from the robust sliding controller is approximated by a constant, $k_\theta = 7$. Speed and depth controllers remain unchanged. As expected, depth trajectory following is very similar to that depicted in figure 5.2.

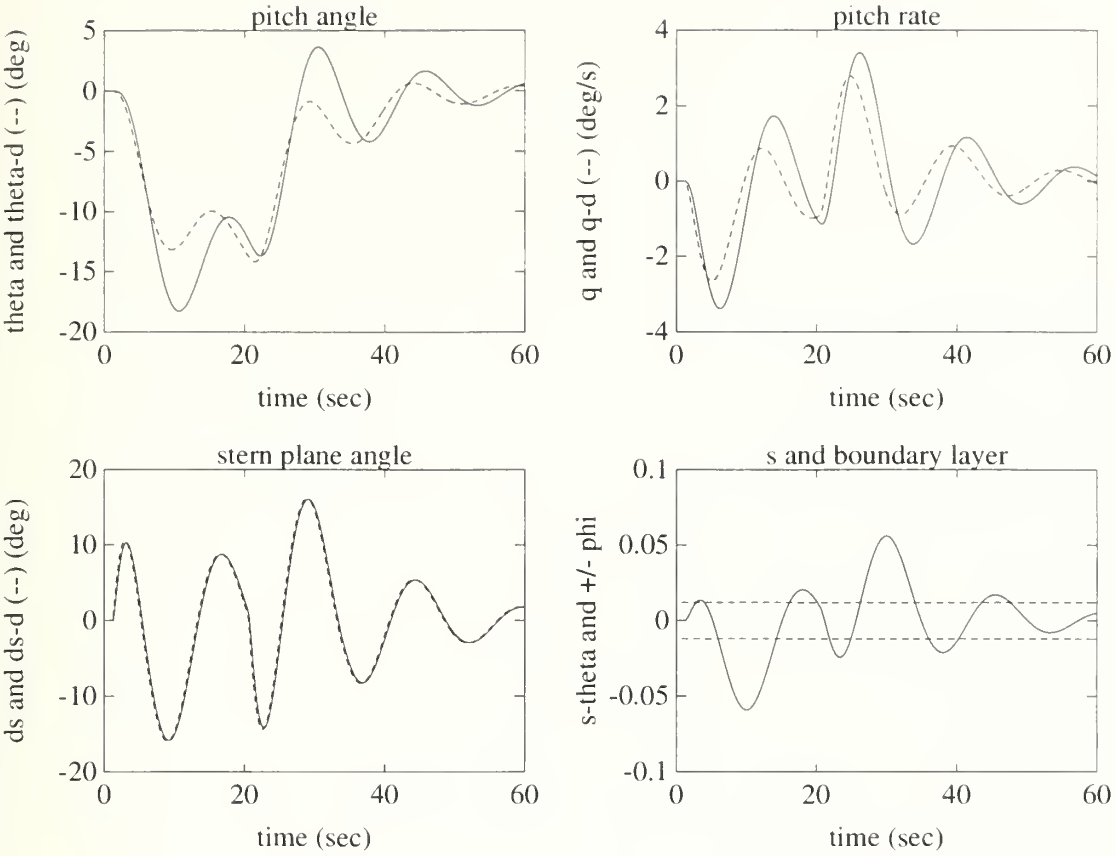

Figure 5.7 21UUV Pitch Response with Adaptive Sliding Pitch Control Law, $\Gamma = \mathbf{0}$. Pitch controller constants are $k_\theta = 7$, $\Phi_\theta = 0.012$. $\hat{\mathbf{a}} = \hat{\mathbf{a}}(0)$ is derived using the same parameter estimates used by the robust sliding controllers in the previous simulation. By design, pitch response is very similar to that depicted in figure 5.3.

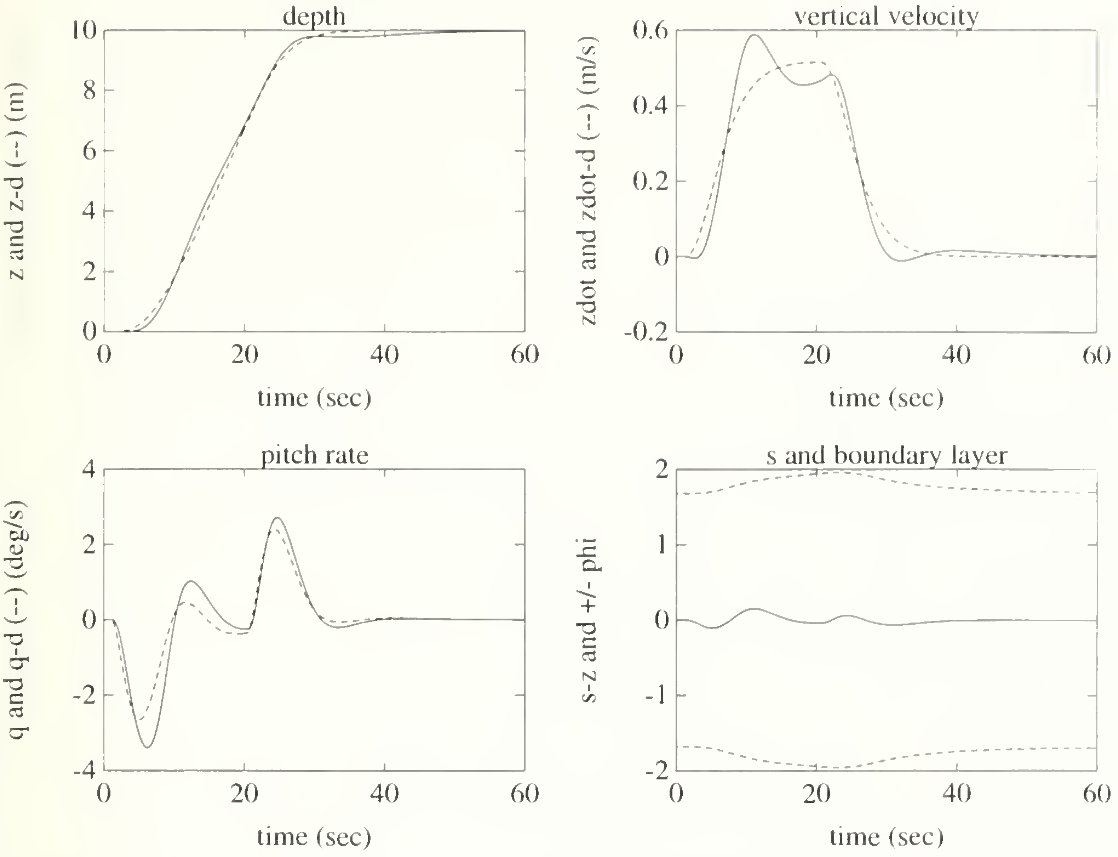

Figure 5.8 21UUV Depth Trajectory with Adaptive Sliding Pitch Control Law, $\Gamma = \Gamma_0$. Here, the pitch control law from equation (5.33) is used with adaptation of parameter estimates, and speed and depth controllers remain unchanged. Depth trajectory following is slightly improved from the previous two cases (figures 5.2 and 5.6) as a result of parameter adaptation by the adaptive pitch controller.

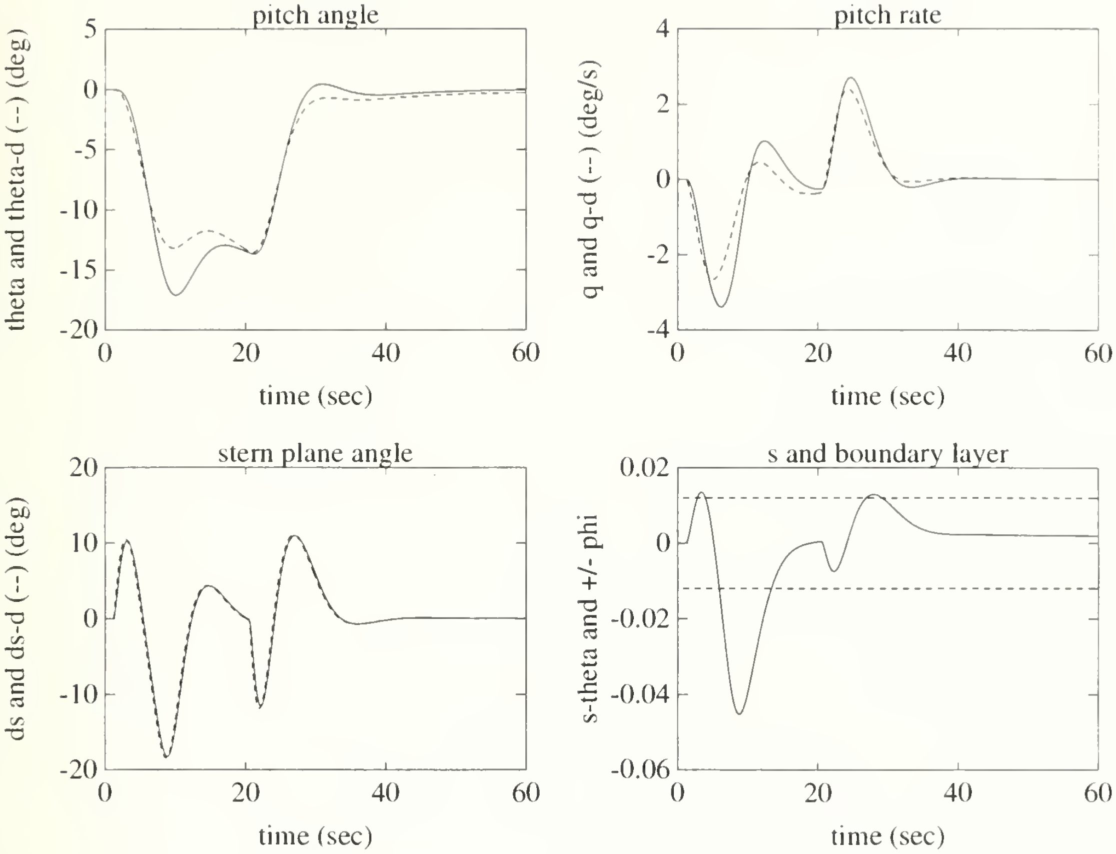

Figure 5.9 21UUV Pitch Response with Adaptive Sliding Pitch Control Law, $\Gamma = \Gamma_0$. Pitch controller values and $\hat{\mathbf{a}}(0)$ remain the same as the previous simulation, but parameter adaptation now takes place. Pitch response is improved from the previous two cases (figures 5.3 and 5.7), resulting in the better depth trajectory following seen in the previous figure.

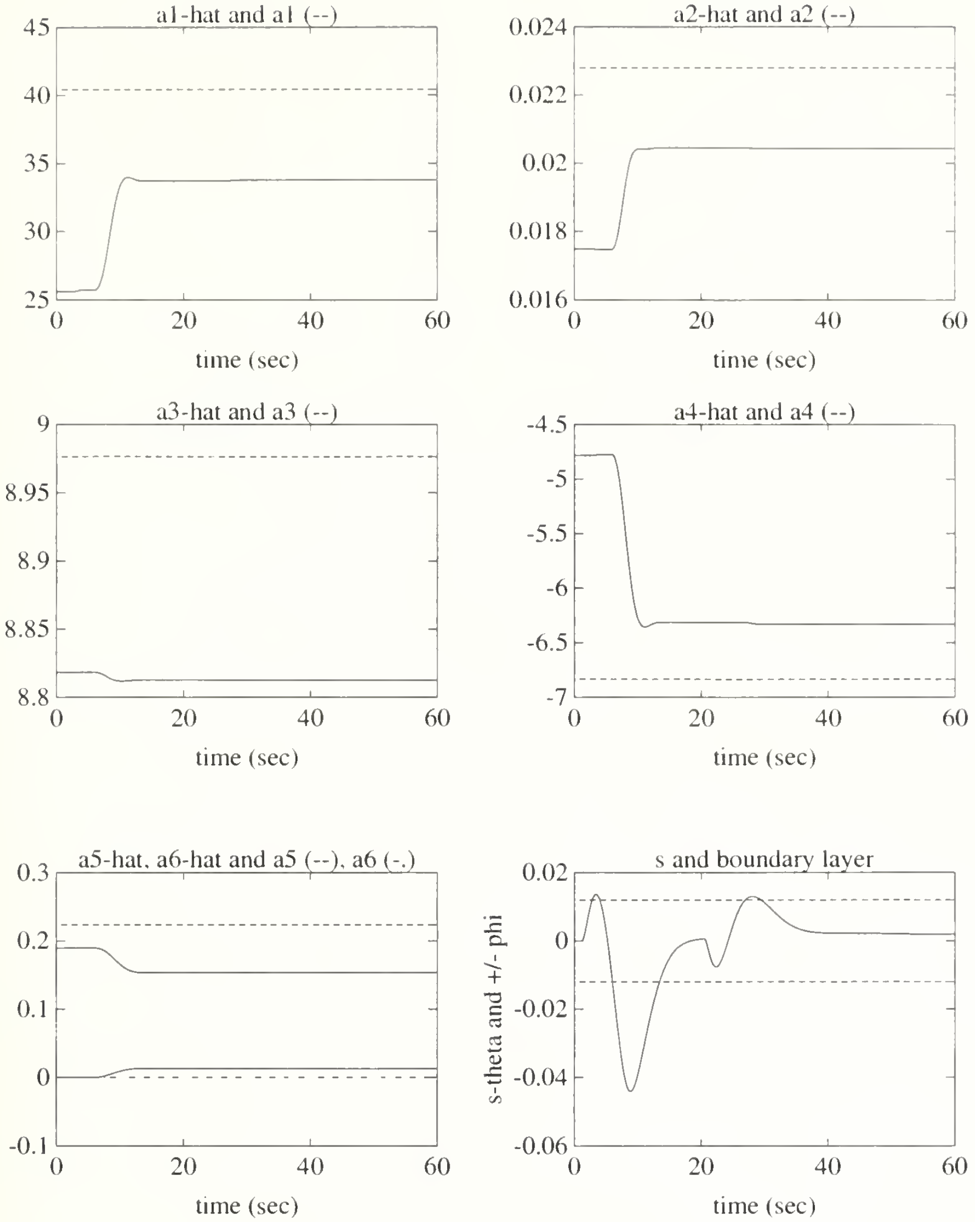

Figure 5.10 Adaptation of $\hat{\mathbf{a}}$ and s_θ with Φ_θ. The parameters $\hat{a}_1(t)$ through $\hat{a}_6(t)$ are shown here for the previous simulation, and it is seen that adaptation occurs only while $|s_\theta| > \Phi_\theta$. It is noted that the parameter estimates, $\hat{a}_i$, do not necessarily converge to their target values, but s_θ does converge to the region inside boundary layer, Φ_θ which implies that $s_{\theta\Delta} \rightarrow 0$.

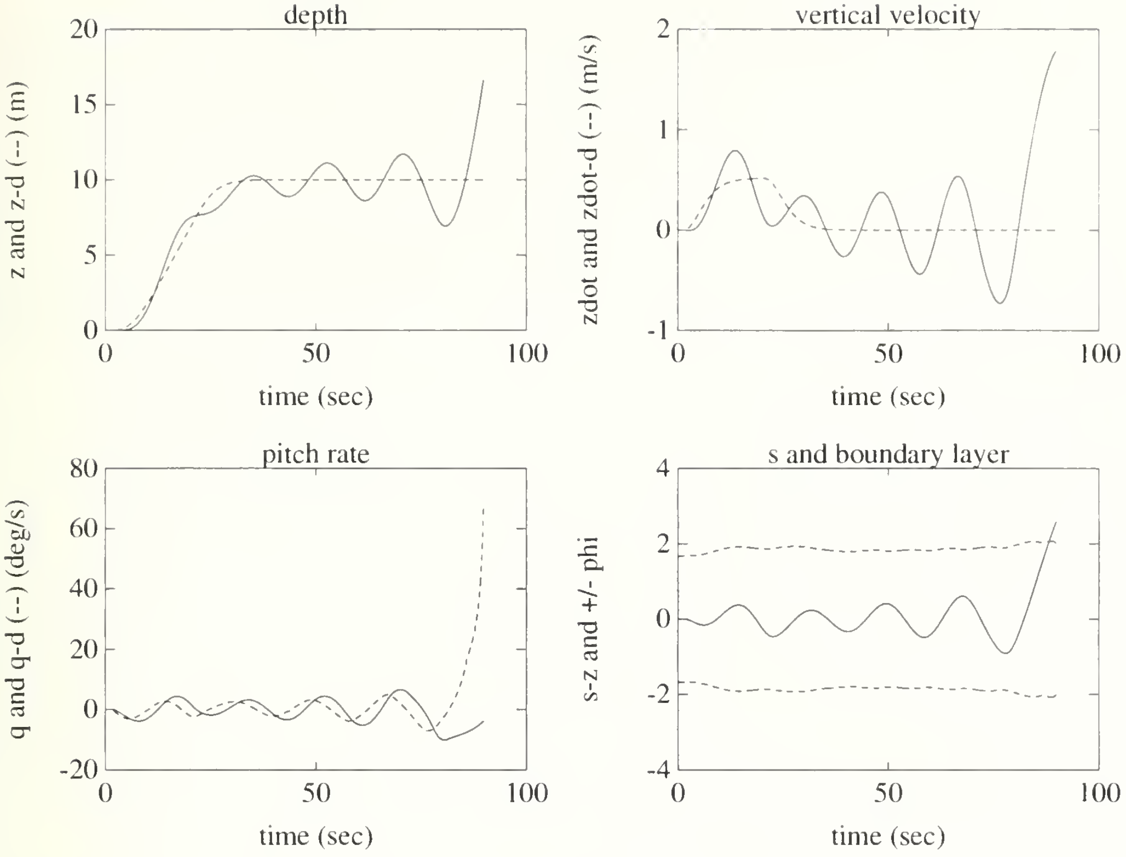

Figure 5.11 21UUV Depth Trajectory with Adaptive Sliding Pitch Control Law, $\Gamma = \mathbf{0}$. Here, the pitch control law from equation (5.33) is used with no adaptation of parameter estimates, and the depth and speed controllers remain unchanged. In this case, it is assumed that there is no prior knowledge of the hydrodynamic coefficients except for M_{δ_s}, which is known to within 30% error as before. Body coefficients, as before, are assumed known to within 5% error. Because parametric uncertainty is so high, without adaptation this control scheme is unstable.

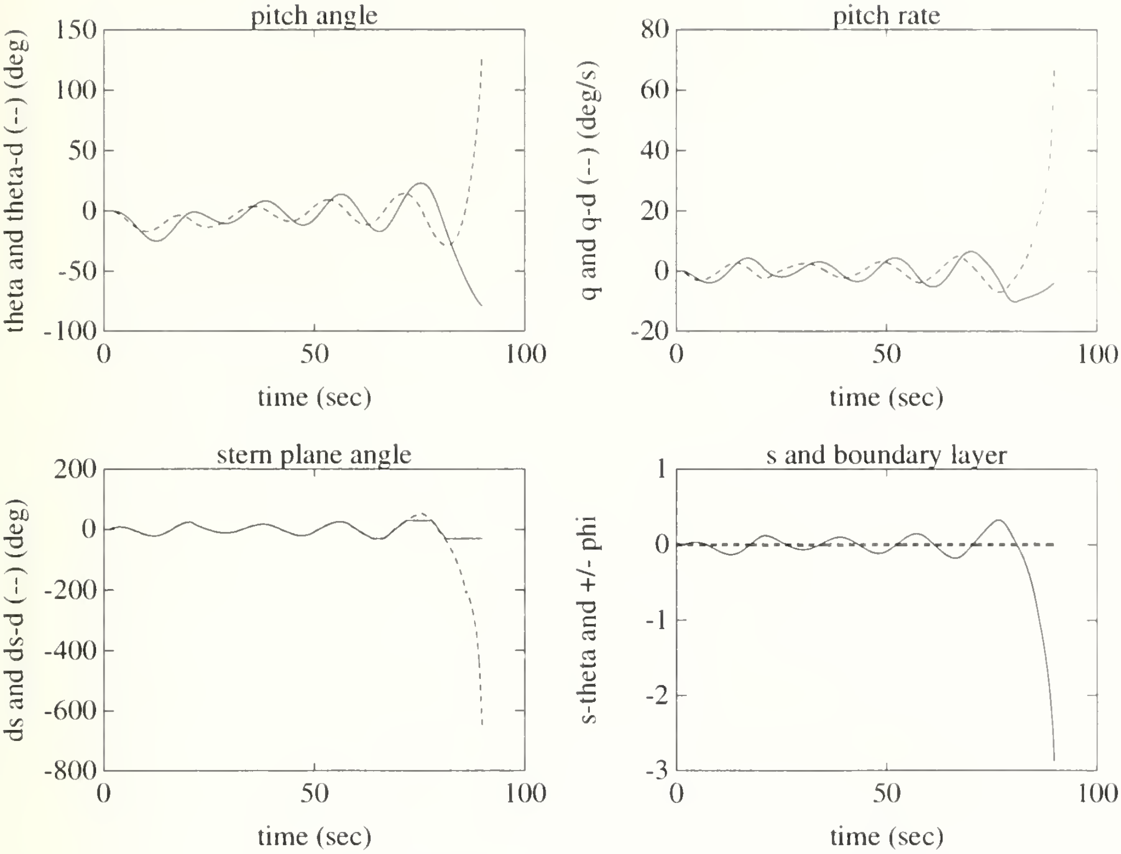

Figure 5.12 21UUV Pitch Response with Adaptive Sliding Pitch Control Law, $\Gamma = \mathbf{0}$. The pitch control law from equation (5.33) is used, and controller constants remain $k_\theta = 7$ and $\Phi_\theta = 0.012$. $\hat{\mathbf{a}} = \hat{\mathbf{a}}(0)$ is derived using an assumption of no prior knowledge of hydrodynamic constants except for M_{δ_s}, which is known to within 30% error as before. The estimates of body coefficients remain unchanged. Parametric uncertainty and the lack of parametric adaptation leads to instability of this pitch controller.

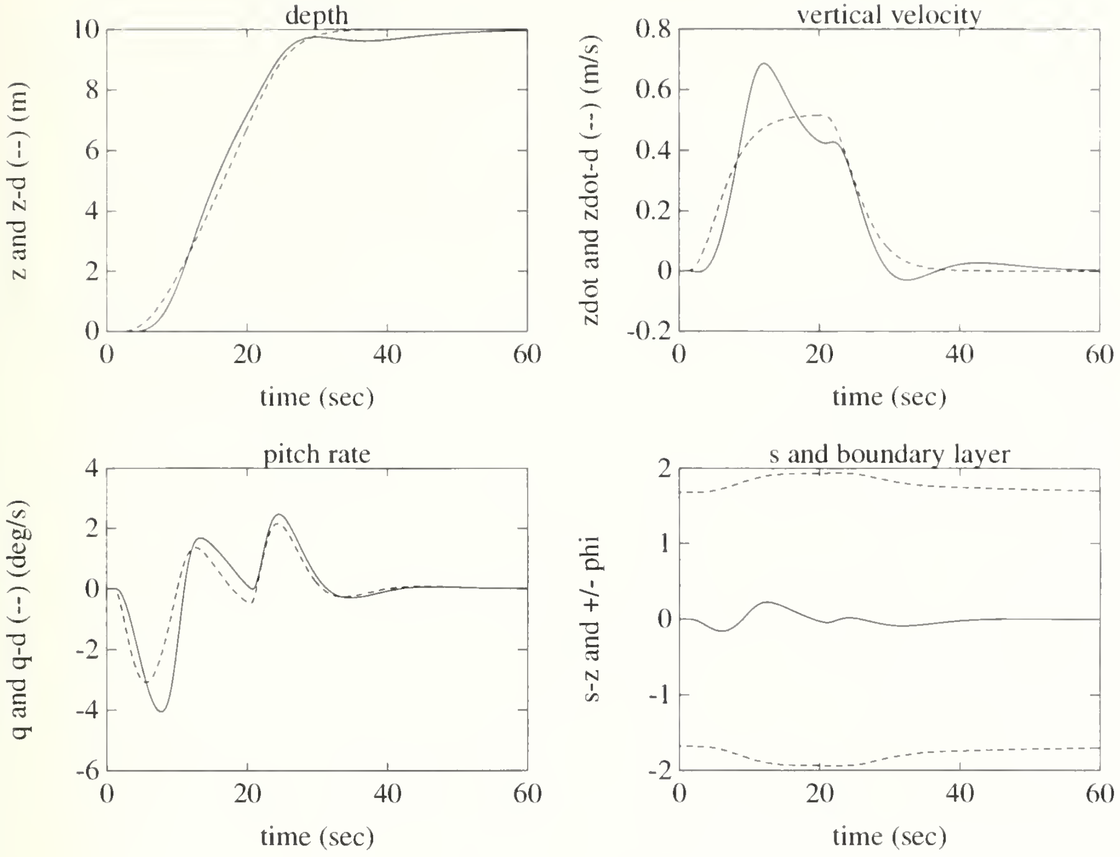

Figure 5.13 21UUV Depth Trajectory with Adaptive Sliding Pitch Control Law, $\Gamma = \Gamma_0$. Here, the pitch control law from equation (5.33) is used with adaptation of parameter estimates. Controller constants remain unchanged, and $\hat{\mathbf{a}}(0)$ is computed as in the previous simulation with no prior knowledge of hydrodynamic coefficients except for M_{δ_s}, which is again known to within 30% error. Despite high initial parametric uncertainty, this controller executes a depth change with good trajectory following.

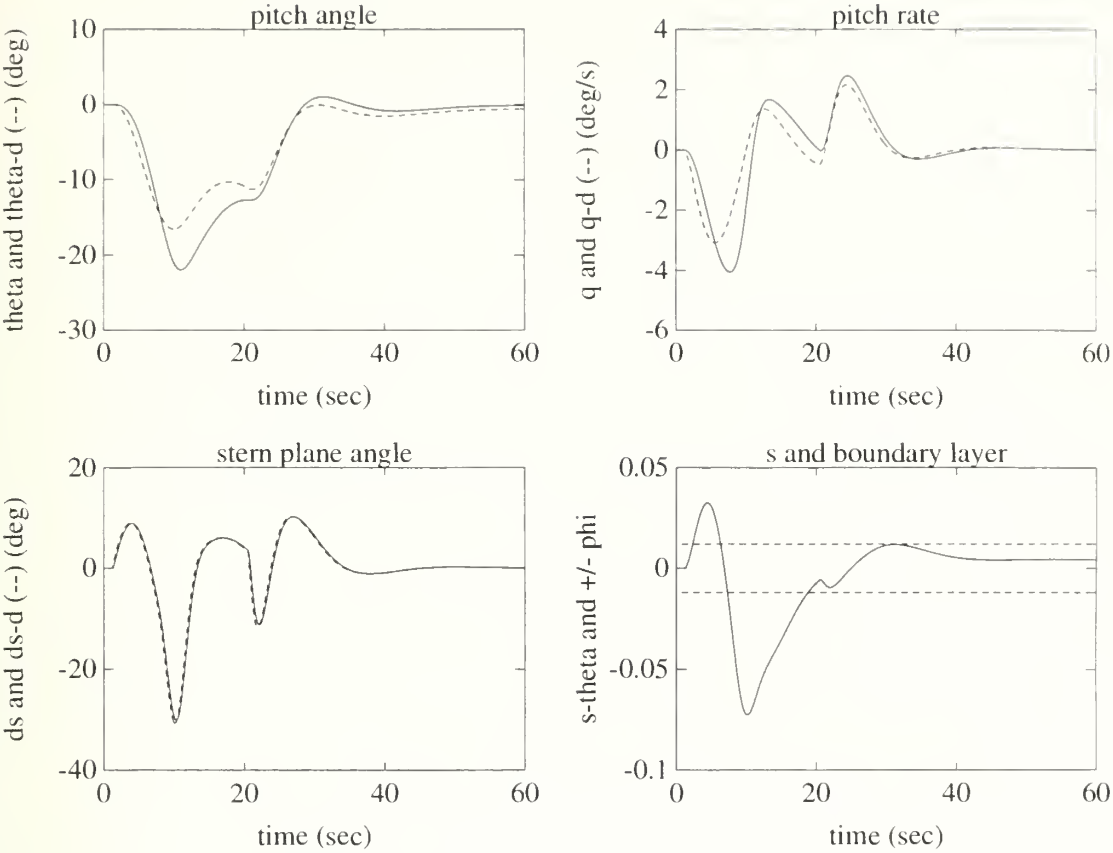

Figure 5.14 21UUV Pitch Response with Adaptive Sliding Pitch Control Law, $\Gamma = \Gamma_0$. Pitch controller values are the same as reported in figure 5.12, as is $\hat{a}(0)$. Despite high initial parametric uncertainty, this adaptive sliding pitch controller provides stable performance which translates to the good depth trajectory following seen in figure 5.13.

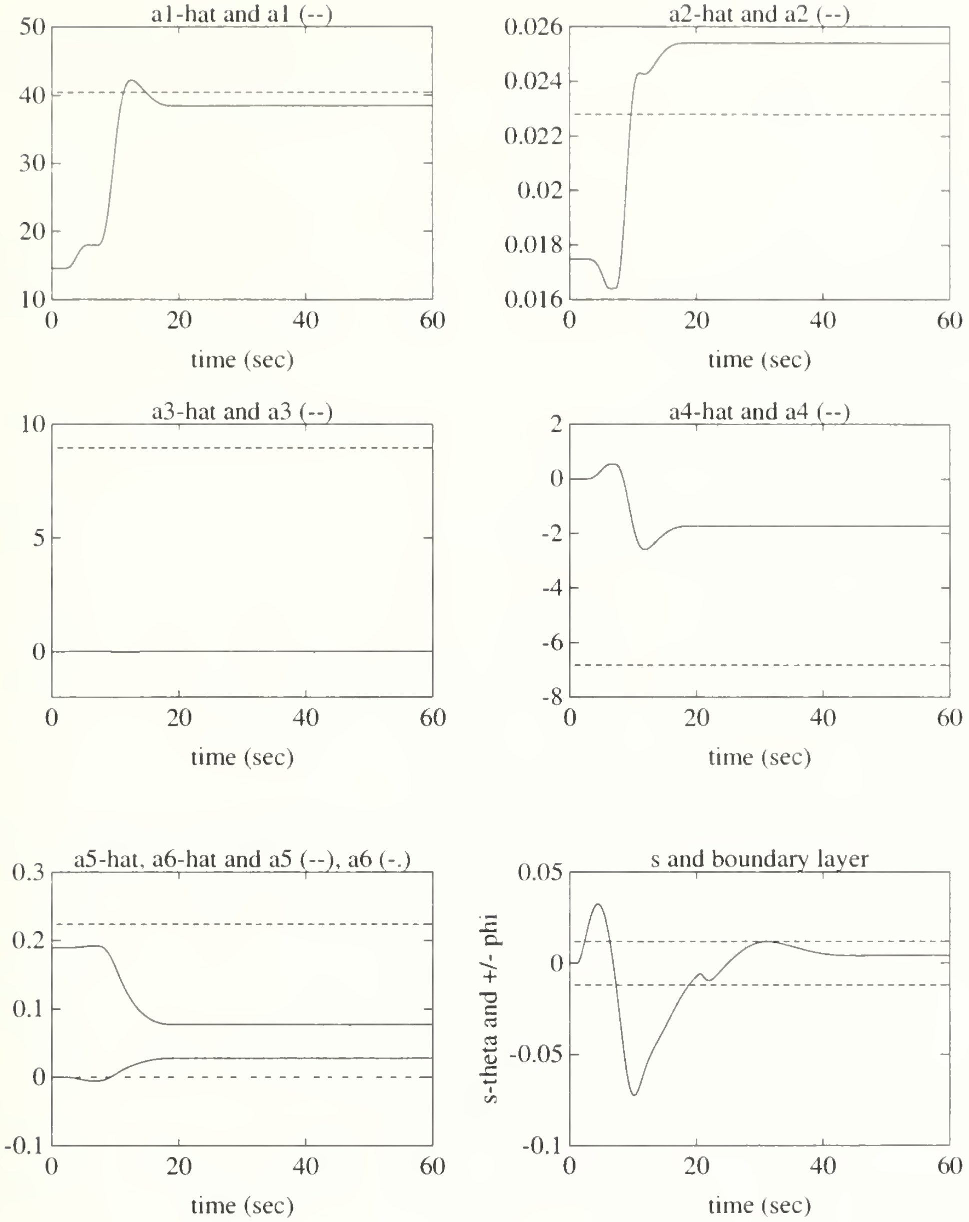

Figure 5.15 Adaptation of $\hat{\mathbf{a}}$ and s_θ with Φ_θ. The parameters $\hat{a}_1(t)$ through $\hat{a}_6(t)$ are shown here for the previous simulation with almost total hydrodynamic coefficient uncertainty. Like the case presented in figure 5.10, adaptation occurs only while $|s_\theta| > \Phi_\theta$, and parameter estimates do not necessarily converge to their target values, but $s_{\theta\Delta} \to 0$.

5.3.3 Pitch Control in Regular Waves

Now considered is the case where the objective of the pitch controller is to regulate the 21UUV pitch angle at 0 degrees in the presence of a single frequency disturbance, such as that provided by regular waves. Though the coupled equations of motion and forward speed control are as before, the depth controller is disabled and no longer provides desired pitch information. Instead, θ_d, $\dot{\theta}_d$, and $\ddot{\theta}_d$ are maintained at 0, while u_d is 2 m/s as before. This is done in an attempt to maintain the coupling effects of the speed and heave equations to the pitch equation, particularly in the presence of disturbances to all three axes, as will be investigated in section 5.3.4. Such a situation of regulating pitch at 0 degrees may arise in practice during a phase of AUV operation when the stability of vehicle attitude takes priority over vehicle vertical position in the water column.

In the following simulations, k_θ and Φ_θ are adjusted from the previous simulations to demonstrate the effect of the disturbance adaptation. The previous values of k_θ and Φ_θ provided a pitch controller insensitive to the level of disturbance, which, when canceled, did not saturate the sternplane actuators at the 21UUV forward speed of 2 m/s.

Figure 5.16 depicts a simulation of the 21UUV subjected to a pitch disturbance of single frequency, with the pitch control law from equation (5.33) and no adaptation. In figure 5.17, pitch control of the 21UUV is shown with the same controller and subjected to the same disturbance, but with adaptation of the vehicle parameter estimates enabled. Though vehicle parameter estimates are updated through adaptation, little improvement in pitch regulation is seen with this second simulation.

Assuming that the pitch disturbance frequency is known allows for use of the adaptive controller with disturbance cancellation terms as described in equation (5.38). Figure 5.18 depicts this adaptive pitch controller performance in the presence of the same monochromatic disturbance used in the previous two simulations. The advantage of being able to include

cancellation terms which allow for phase and magnitude matching of the disturbance is seen in figure 5.18 as this controller substantially eliminates the effects of the regular waves and best maintains the 21UUV pitch at 0 degrees.

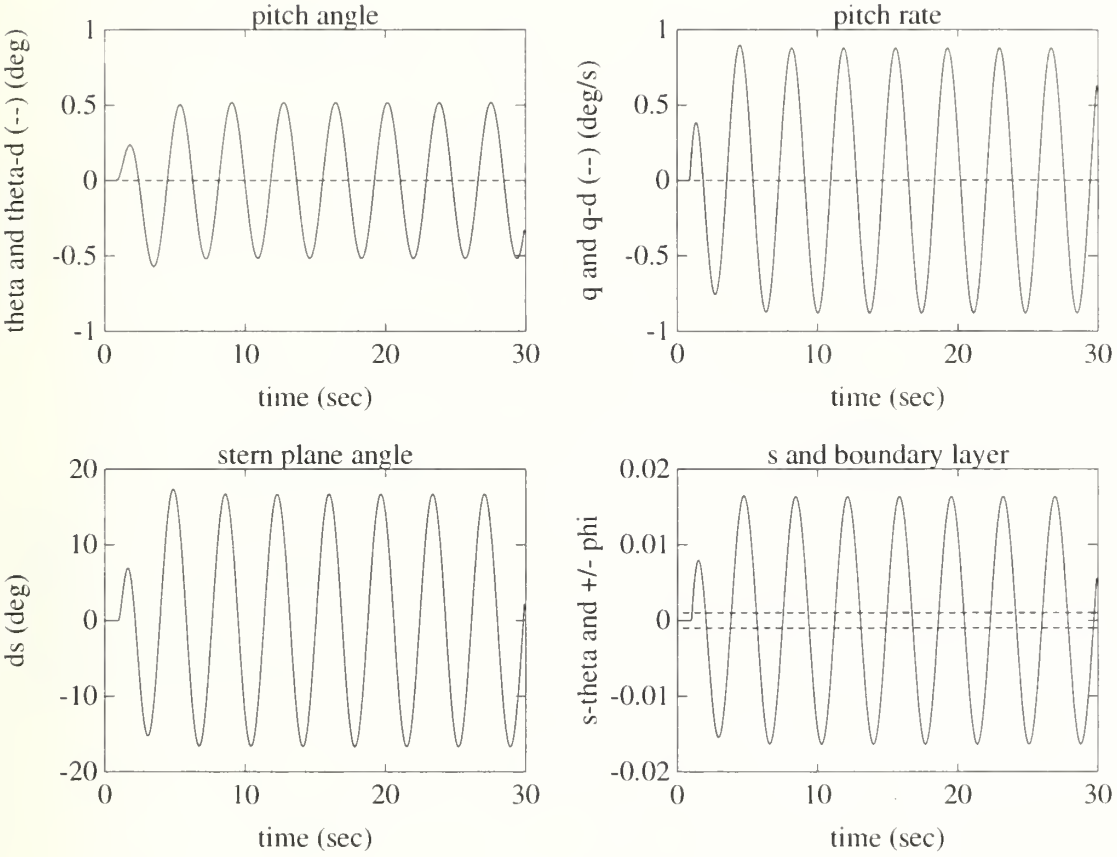

Figure 5.16 Adaptive Pitch Control Law with Single Frequency Disturbance, $\Gamma = \mathbf{0}$. For this and the following simulations where a single frequency pitch disturbance is used, $k_\theta = 80$, $\Phi_\theta = 0.001$, and $M_d(t) = 400 \sin(1.7\,t + 0.3)$ N - m. The vector $\hat{\mathbf{a}}(0)$ is calculated from here on with the assumption that body and hydrodynamic coefficients are known to within 5% and 30% error, respectively, with the estimated coefficient values chosen as described in section 5.3.1.

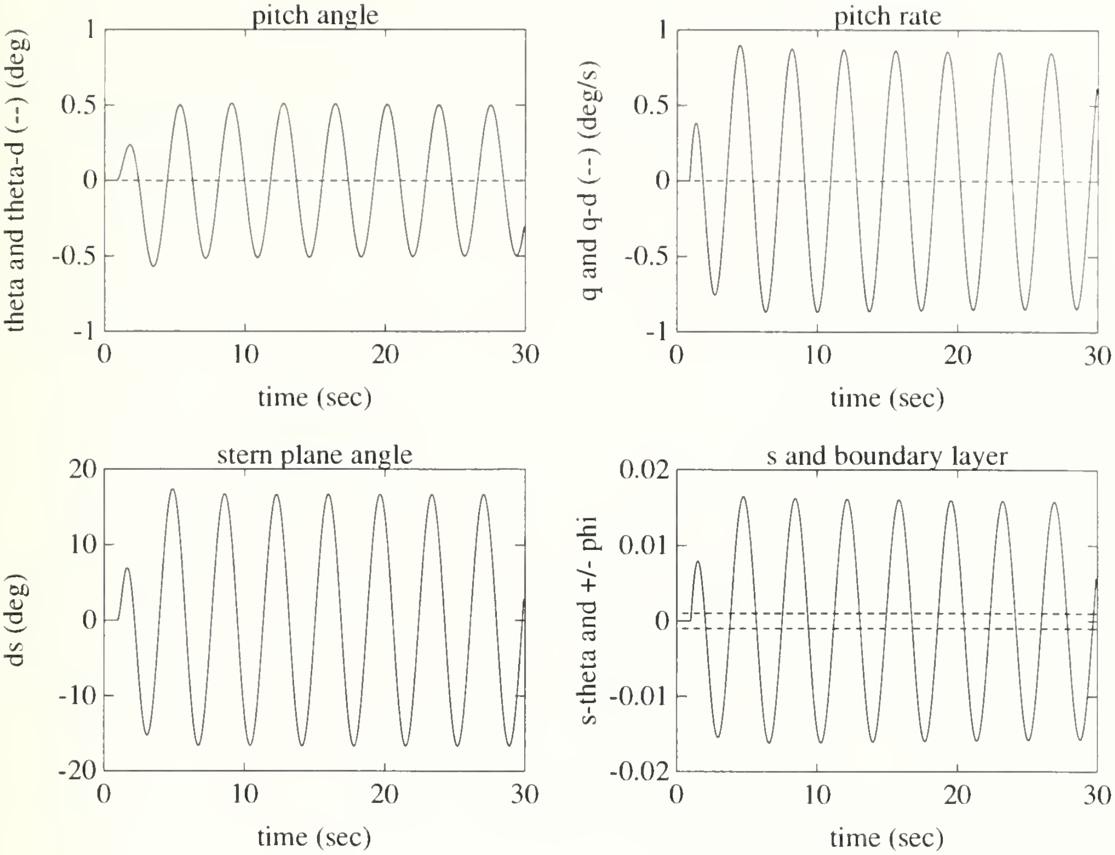

Figure 5.17 Adaptive Sliding Pitch Controller with Single Frequency Disturbance. This adaptive controller includes no disturbance cancellation terms, and $\Gamma = \Gamma_0$. While parameter estimate adaptation occurs, it is seen that pitch performance is very similar to the previous simulation with no adaptation.

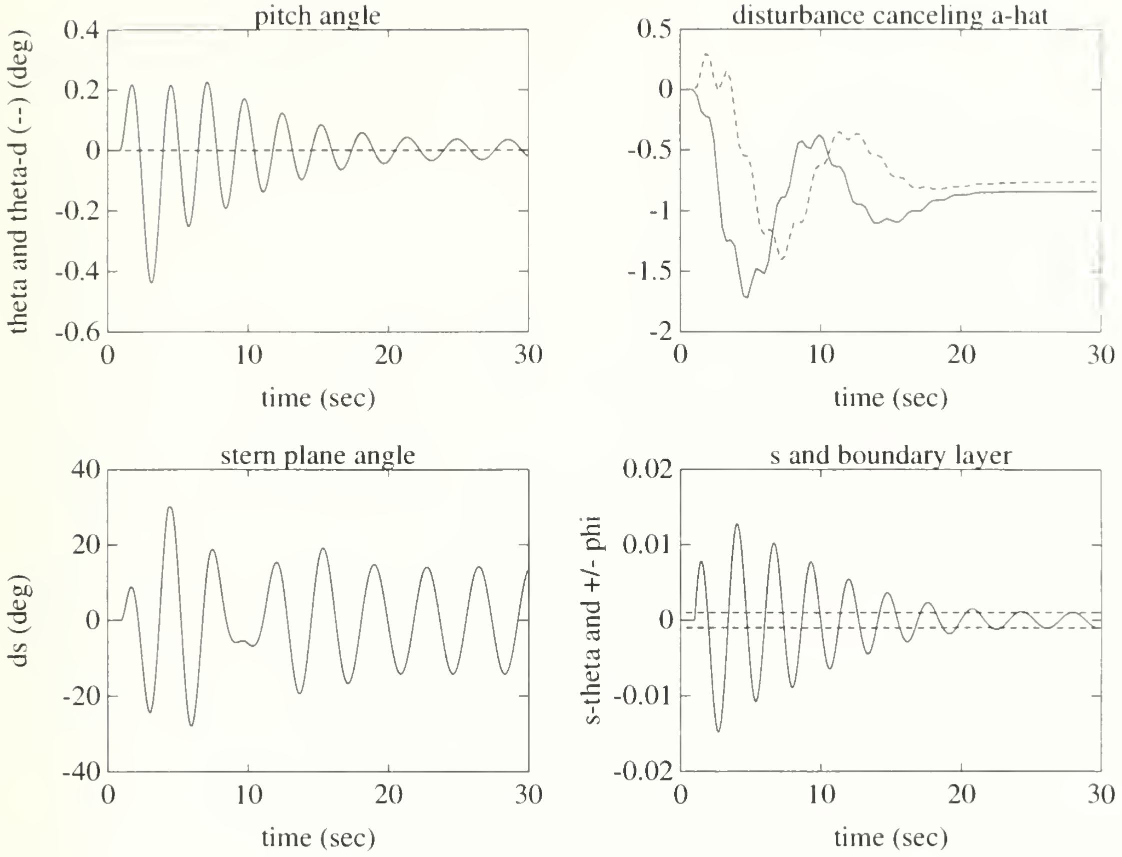

Figure 5.18 Adaptation to a Single Frequency Disturbance by the Pitch Controller. Here, Γ = diag[Γ_0, 100**I**]. Performance is improved with this controller which uses two disturbance cancellation terms, $\hat{a}_7 \sin(1.7\,t)$ and $\hat{a}_8 \cos(1.7\,t)$, to adapt to and cancel the pitch disturbance of known frequency, but of unknown phase and magnitude. Pitch response is significantly reduced from the previous cases, with final control action magnitude comparable to that of the previous two controllers. The error parameter, s_θ is seen to decrease in amplitude so that it becomes bounded by Φ_θ, which implies that $s_{\theta\Delta} \to 0$.

5.3.4 Pitch Control in Random Waves

Considered here is pitch control for the 21UUV at a depth of 10 meters, in water 30 meters deep, and in the presence of a disturbance which approximates that of sea state 2 conditions. The theory presented in chapter 2 is used to calculate the spectra of pitch, heave, and surge disturbances. A set of possible time realizations for the three disturbances is then generated. These disturbances are used in simulations to investigate the performance of the adaptive sliding pitch controllers presented in section 5.2.

Figure 5.19 depicts the single-sided pitch, heave, and surge spectra. The first 60 seconds of pitch, heave, and surge time records used in the subsequent simulations are depicted in figure 5.20. Associated with figure 5.20 are maximum horizontal and vertical displacement parameters of 0.2, justifying the use of the inertia dominated wave force assumption.

Control simulations follow, and figure 5.21 shows an adaptive sliding pitch controller with no disturbance cancellation terms regulating 21UUV pitch angle at 0 degrees in the presence of the stochastic wave disturbance. Attempting to partially reproduce the adaptive disturbance cancellation results seen in section 5.3.3, seven disturbance cancellation frequencies which span the known disturbance spectrum are added in feedforward, and their amplitudes and phase are adapted on-line. Figure 5.22 depicts this adaptive controller performance under the same conditions as those used with the previous simulation. The improvement in pitch regulation by this adaptive controller with disturbance cancellation terms is seen. Improvements for adaptive controllers with fewer disturbance cancellation terms, or for lower gain controllers with larger values of Φ_θ, were found to be far less significant.

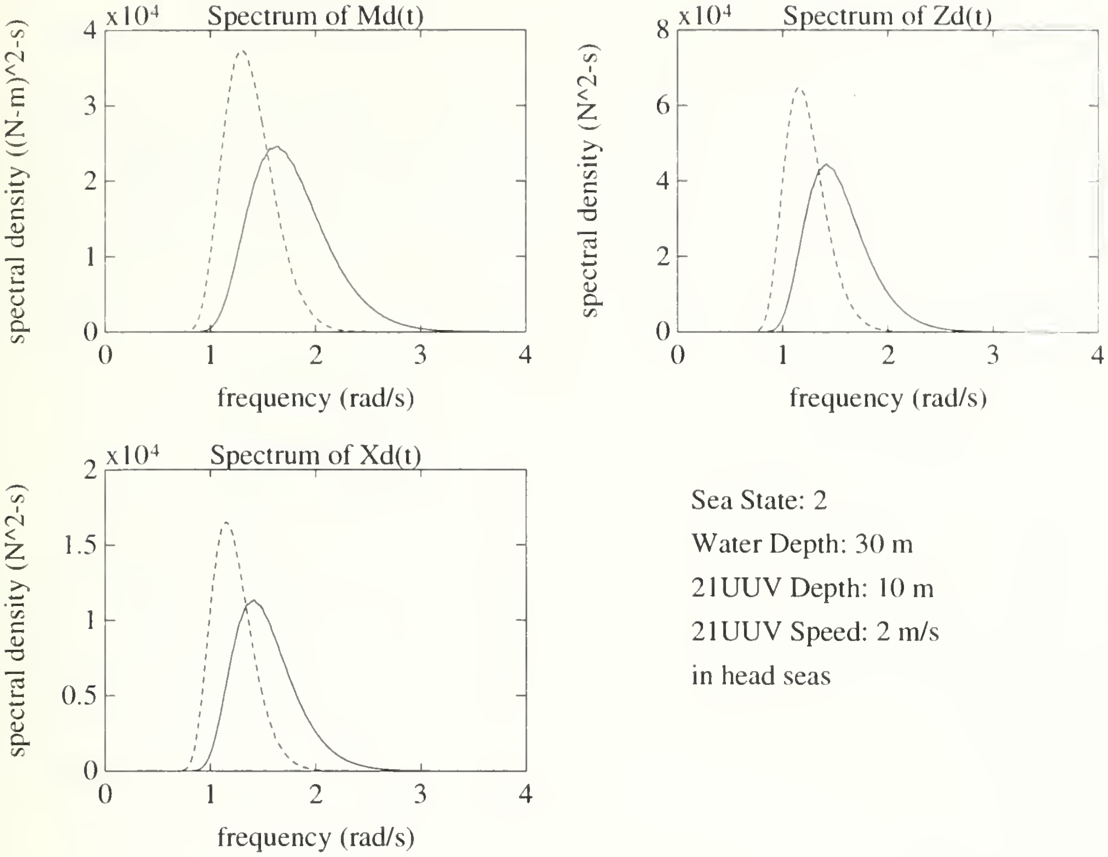

Sea State: 2
Water Depth: 30 m
21UUV Depth: 10 m
21UUV Speed: 2 m/s
in head seas

Figure 5.19 Wave Disturbance Spectra. The single-sided spectra above were generated using the ITTC recommended surface wave spectrum and the transfer functions for the 21UUV in inertia dominated wave forces presented in chapter 2. The dashed lines represent the head sea disturbance spectra for the AUV at 0 m/s, while the solid curves account for the shift of the spectra due to vehicle forward motion and frequency of encounter with the waves. As a spectrum is shifted to the right and its energy is spread over a larger range of frequencies, its peak amplitude drops, but the areas under the unshifted and shifted spectra remain equal.

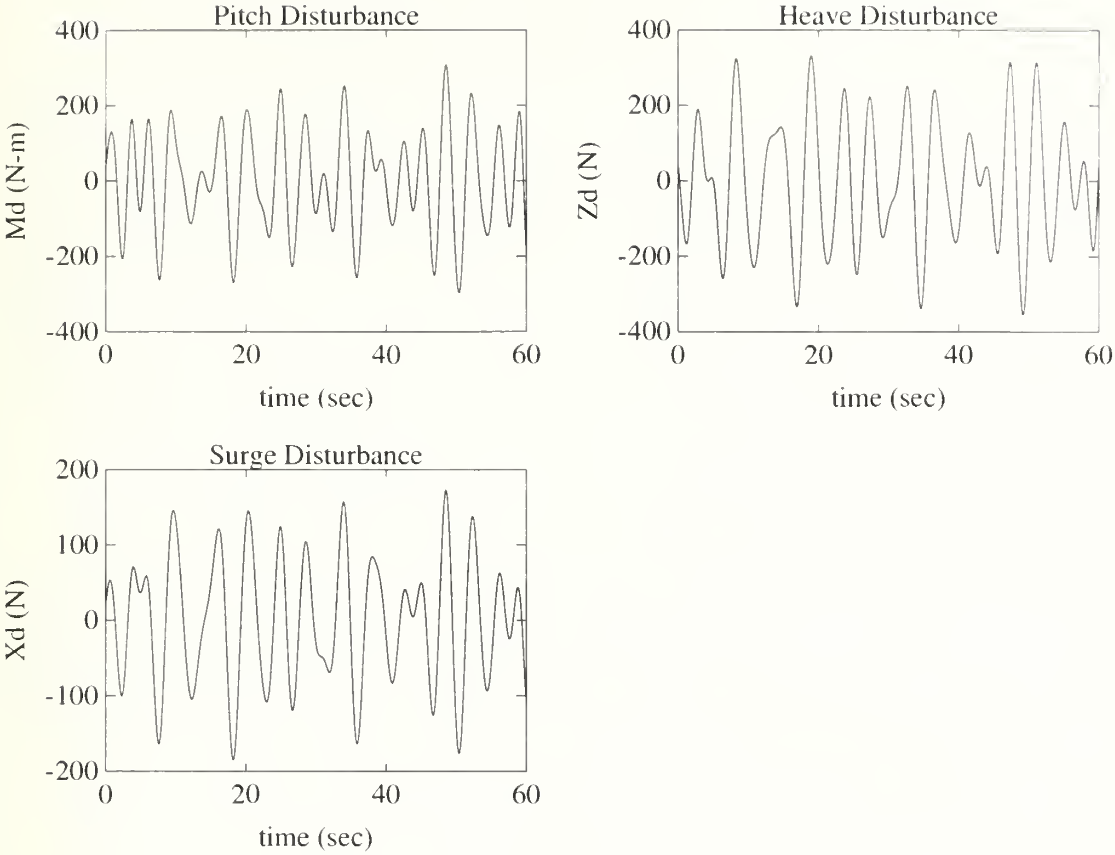

Figure 5.20 Possible Time Realizations for Pitch, Heave, and Surge Disturbance. These disturbances were generated using the spectra in figure 5.19 and by superimposing 350 sine components as described in section 2.1.2. While the phase of each sine wave is random, proper relative phase between the sine components of each of the three disturbances (as presented in section 3.3.3.1) is preserved.

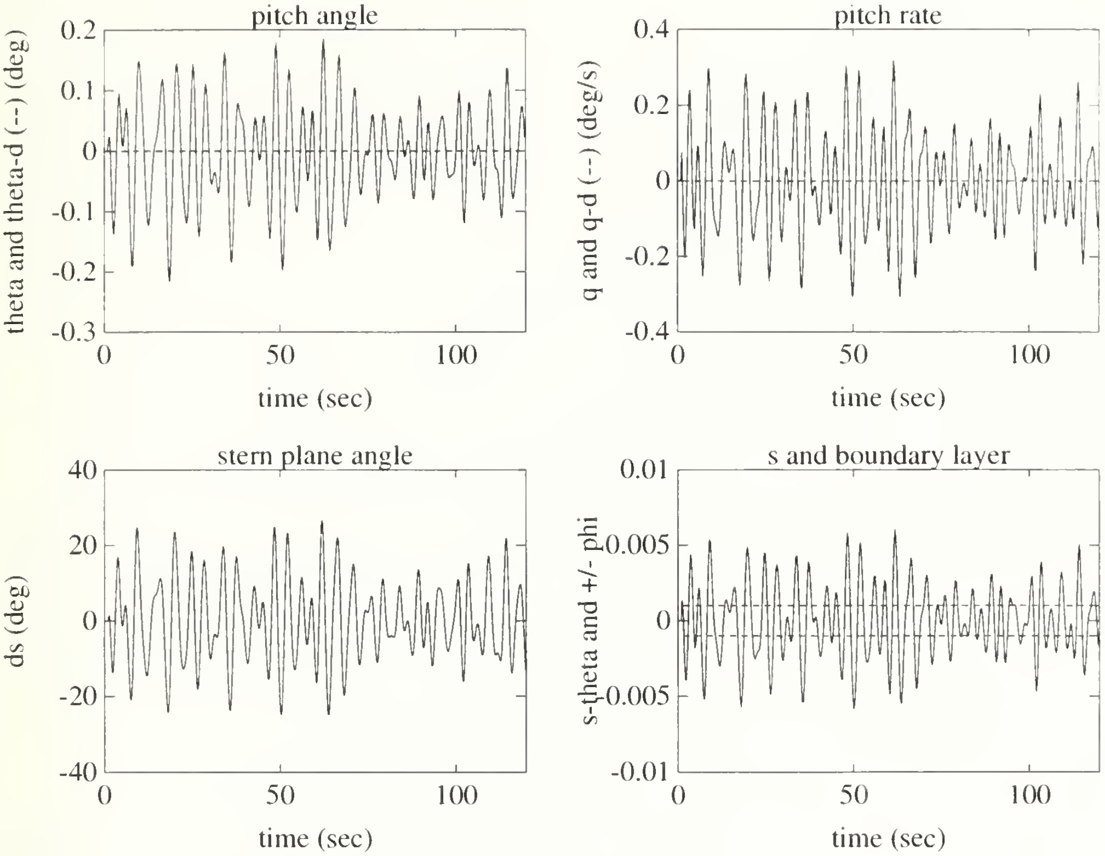

Figure 5.21 Adaptive Sliding Pitch Control with Stochastic Disturbance. Here, $\Gamma = \Gamma_0$, $k_\theta = 200$ and $\Phi_\theta = 0.001$. Pitch angle regulation is good with this high gain controller, with $|\theta| \leq 0.2°$ during the simulation. This controller performance is used to measure against the following pitch controller which adds adaptive sine and cosine disturbance cancellation terms in an attempt to partially eliminate the effect of the random wave disturbance.

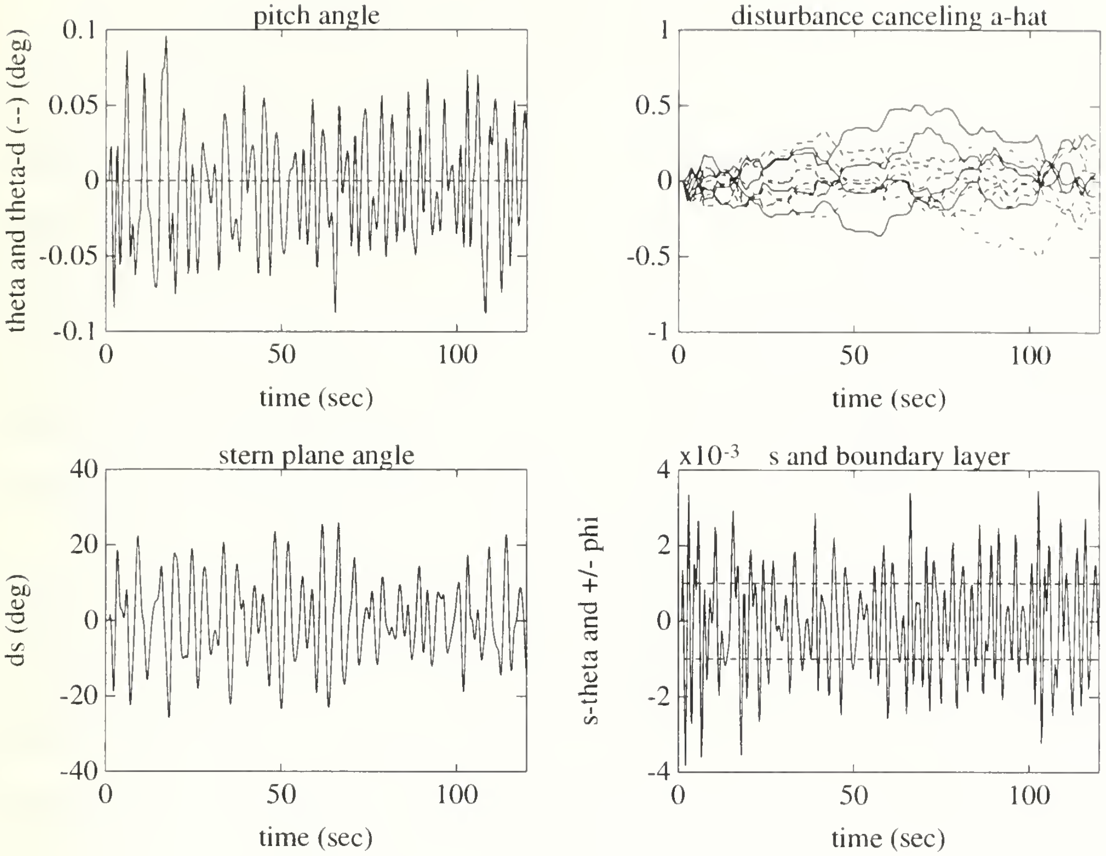

Figure 5.22 Adaptive Sliding Pitch Control with Stochastic Disturbance. As in figure 5.21, $k_\theta = 200$ and $\Phi_\theta = 0.001$, but here 14 disturbance cancellation terms are added in feedforward and adapted on-line in an attempt to partially cancel the stochastic wave disturbance, and $\Gamma = \mathrm{diag}[\Gamma_0, 100\mathbf{I}]$. The cancellation terms include a sine and cosine each at frequencies of 1.4, 1.5, 1.6, 1.7, 1.8, 1.9, and 2.0 rad/sec. The coefficients of the 14 disturbance cancellation terms are plotted in the upper right. It is seen that steady state is not reached for the 14 coefficients, nor is it expected to be reached because exact cancellation of the stochastic disturbance with seven sinusoids is not possible. However, pitch amplitude is reduced over the previous simulation as $|\theta| \leq 0.1°$. The improvement in pitch regulation for adaptive controllers with fewer disturbance cancellation terms, or for lower gain controllers with a larger value of Φ_θ, was not found to be nearly as pronounced.

The simulations demonstrating improvement in pitch regulation by adaptive sliding controllers with disturbance cancellation terms seen in the previous monochromatic and random disturbance cases each required higher gain controllers than the pitch controller used for depth trajectory following. In general, higher gain is less desirable because it makes a controller more susceptible to state measurement noise, and is more likely to excite unmodeled or non-ideal actuator dynamics. Particularly for the 21UUV at low forward speeds, it is apparent that a higher gain pitch controller would sooner cause sternplane saturation as wave severity increased. Simulating the 21UUV operating at 5 meters depth in sea state 2 illustrates this point.

Figure 5.23 depicts the 21UUV adaptive pitch controller ($k_\theta = 7$, $\Phi_\theta = 0.012$, and $\Gamma = \Gamma_0$) regulating AUV pitch in the presence of a wave disturbance which simulates that of the vehicle operating in sea state 2, head seas, 30 meter deep water and at a depth of 5 meters. All three coupled longitudinal plane equations are again simulated so that the coupling effects of surge and heave on pitch are present. Figure 5.24 shows the adaptive pitch controller ($k_\theta = 200$, $\Phi_\theta = 0.001$ and $\Gamma = \mathrm{diag}[\Gamma_0, 100\mathbf{I}]$) with 14 disturbance cancellation terms simulated under the same conditions. As predicted, the higher gain causes actuator saturation, and the resulting controller performance is poorer than that of the lower gain pitch controller shown in figure 5.23.

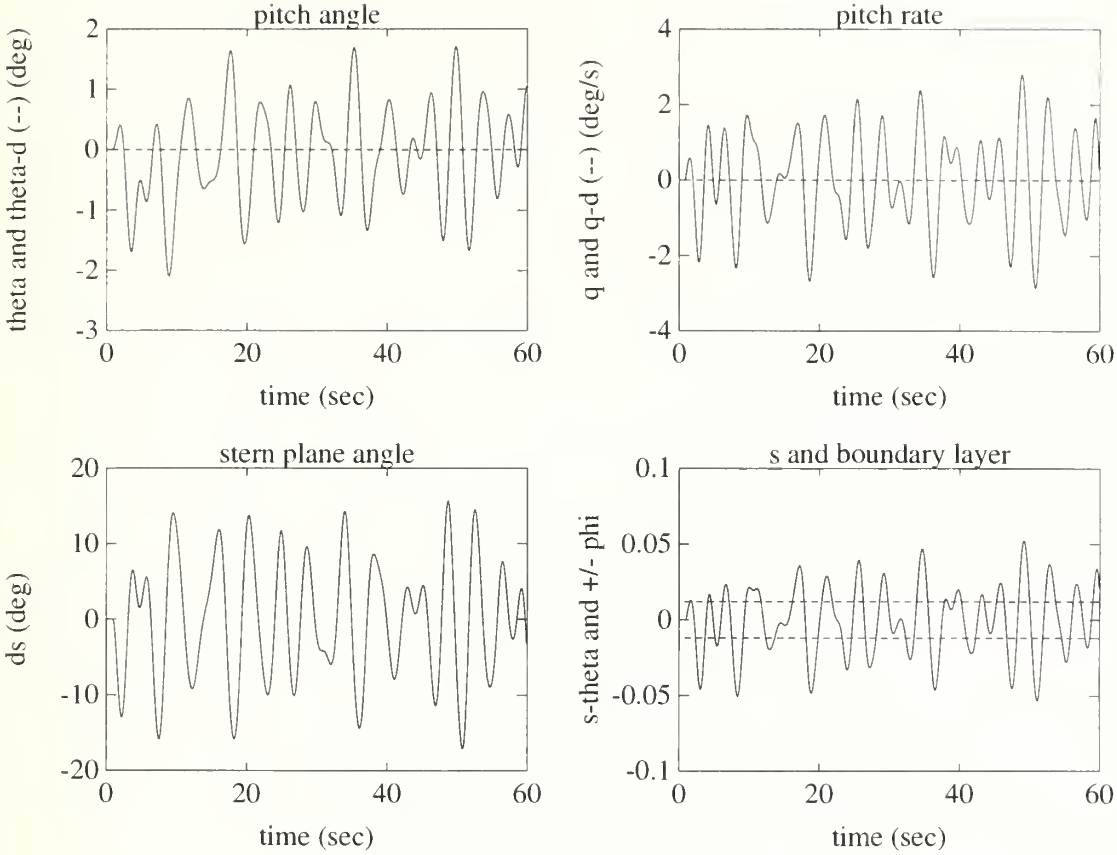

Figure 5.23 Adaptive Sliding Pitch Control with Stochastic Disturbance. No feedforward cancellation terms are used in this controller, and $\Gamma = \Gamma_0$, $k_\theta = 7$ and $\Phi_\theta = 0.012$. The simulated disturbance here is on the 5 meter deep 21UUV in sea state 2. Sternplane action is significantly less than in the following simulation which uses a higher gain pitch controller.

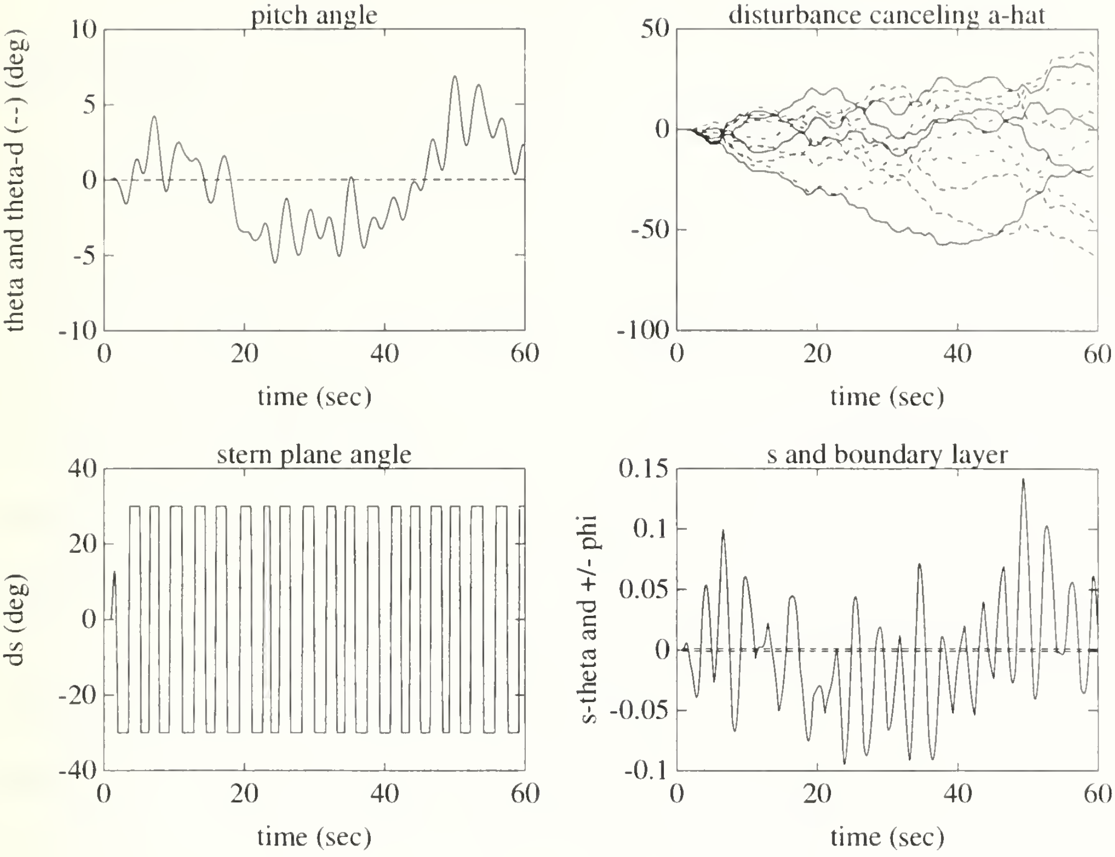

Figure 5.24 Adaptive Sliding Pitch Control with Stochastic Disturbance. This controller uses 14 terms with 7 frequencies (1.4, 1.5, 1.6, 1.7, 1.8, 1.9, and 2.0 rad/sec) in an attempt to adapt to the stochastic disturbance. Here, Γ = diag[Γ_0, 100**I**], $k_\theta = 200$ and $\Phi_\theta = 0.001$ Sternplane saturation is evident and the resulting pitch performance is much poorer than that depicted in figure 5.23 for the lower gain controller.

5.3.5 Summary

The sliding controllers developed in sections 5.1 and 5.2 for 21UUV longitudinal plane control were demonstrated here in simulation. Robust sliding control and adaptive sliding control techniques were applied to the pitch axis of the AUV, while robust sliding control laws alone were used for the depth and forward speed controllers. Development of the robust sliding control laws assumed that the hydrodynamic and body coefficients of the dynamics equations were bounded by some known, possibly time varying function, whereas the assumption implicit with the adaptive sliding control law was that the hydrodynamic and body coefficients remained constant.

21UUV pitch controller performance was shown to directly affect depth trajectory following as variations of sliding pitch control were used in the 3 axis, integrated control simulation of the 21UUV making a depth change maneuver. The effect of parametric uncertainty upon the performance of the pitch controllers was investigated, and the adaptive pitch controller was shown to provide good performance, resulting in good depth trajectory following, despite almost total hydrodynamic coefficient uncertainty.

An extension of the adaptive pitch controller was shown to adapt to and cancel a pitch disturbance simulating that of a monochromatic wave of known frequency, but of unknown magnitude and phase.

The developments of chapters 2 and 3 were used to generate a coordinated set of stochastic pitch, heave, and surge disturbances which the 21UUV might encounter in practice. The adaptive controller was again extended to include additional disturbance canceling terms in an attempt to achieve better pitch control performance. For the case presented, pitch regulation was improved by the addition of disturbance cancellation terms, though a high gain controller was needed to demonstrate this effect.

A second, more severe set of stochastic pitch, heave, and surge disturbances were then generated to demonstrate the effect of sternplane actuator saturation on the higher gain adaptive controller. When compared to the lower "bandwidth" pitch controller, the high gain controller was sooner to cause sternplane saturation with increasing disturbance severity, which resulted in its poorer performance when compared to the lower gain controller.

Chapter 6 CONCLUSIONS

6.1 Summary

Chapter 1 began with the motivation for this research work, namely to investigate the effect of water waves on a slender body, autonomous underwater vehicle operating in a region of the water column where inertia dominated wave forces dominate. The purpose of this research is not purely academic; operation in coastal waters and sea state 2 by such a vehicle, the NUWC 21UUV, is contemplated. The research objectives of this work were outlined and are consistent with a preliminary study of the problem: to develop a simple model for predicting wave disturbances; to perform tests which investigate the validity of the assumptions made in developing the model; and to use the model to demonstrate the effect of wave forces on the vehicle when controlled by a variation of its proposed controller.

Chapter 2 used existing linear wave theory, slender body strip theory, and linear time invariant systems theory to develop a method to predict the effect of wave disturbances on a stationary, slender body underwater vehicle. First, the prediction of monochromatic wave effects was addressed. These results were extended using a statistical description of waves and an assumption about the superposition of wave forces when operating in an inertia dominated wave force regime. Formulae for calculating the magnitude and phase of the transfer function from surface water waves to the disturbances on five of the six 21UUV axes were presented. Only the disturbance transfer function for the 21UUV roll axis did not lend itself to this method of

calculation, while a procedure for predicting surge, heave, sway, pitch and yaw axes disturbance transfer functions was shown.

Having a statistical description of the sea surface, and using LTI system theory with the previously developed transfer functions allowed for development of a spectral description of the wave disturbances on the AUV. By using an earlier described method to generate a time simulation of the sea surface associated with a given sea spectrum, the generation of a simulated time record of wave disturbances on the AUV was shown.

Chapter 3 described all aspects of the experimental tests which were conducted to investigate the validity of the transfer function model for wave forces on a stationary slender body vehicle. The experimental setup, consisting of a tow tank with motorized sliding carriage, the AUV tow body model, force and wave sensors, and data collection equipment were detailed. For a 1:4.188 scale model of the 21UUV, it was shown that experiments conducted in the wave tank could preserve the wavelength to vehicle length ratios expected of the full scale vehicle in sea waves. For tests entailing the towing of the 21UUV model under waves, Froude number scaling was used and full scale equivalent forward speeds up to 1.5 m/s were investigated. The trials conducted during the course of testing were outlined, and they included investigating wave forces on the model 21UUV at a variety of model depths, model speeds, wave aspects, wave amplitudes, and over a range of wave frequencies. The processing of the raw data collected during the tests was also described.

Presentation of experimental data along with the predicted results followed. Wave force and moment magnitude and phase on the AUV model were presented in a transfer function format for the tests conducted on the stationary model, and force and moment magnitude were presented for wave disturbances on the towed model.

The stationary model tests largely validated the earlier developed method of predicting wave forces and moments on the body, both in magnitude and in phase. A systematic discrepancy

in the prediction of the heave force on the model vehicle in head seas and at higher frequencies was noted. This discrepancy was seen in both heave force magnitude and phase. The transfer function description of forces and moments on the vehicle was supported by the data as it was shown that the hydrodynamic forces on the body were linearly related to the wave amplitude.

The results of the data collected on the towed AUV model showed a deviation from the stationary body theory for the surge and heave forces. Towing the model AUV at the speeds investigated had minimal effect on the pitch transfer function magnitude. This result supported using the "stationary body" method of predicting the pitch disturbance on the forward moving AUV in subsequent simulations.

Chapter 4 presented equations used to describe the motion of the 21UUV in 6 degrees of freedom. Coordinate systems, rigid body dynamics, hydrodynamic forces, and 21UUV body symmetry were addressed. The wave forces investigated earlier were included in these equations by superimposing them in an external disturbance vector. The 6 degree of freedom model was simplified to include only motion in the AUV longitudinal plane, resulting in coupled surge, heave, and pitch equations for the vehicle.

Chapter 5 presented a method of applying sliding control techniques to the 21UUV longitudinal plane equations developed in the previous chapter. The effects of parametric uncertainty and pitch controller adaptation were demonstrated. It was found that even with almost no knowledge of AUV hydrodynamic coefficients, an adaptive sliding pitch controller was able to provide good pitch control performance throughout a commanded AUV depth change. The same control law without the benefit of parameter estimate adaptation proved unstable. This finding suggests that in practice, good 21UUV controller performance could still be achieved despite numerous in-field AUV configuration changes, and without the benefit of additional hydrodynamic coefficient analysis.

Pitch control in the presence of wave disturbances was also investigated, and it was shown that an adaptive sliding pitch controller could eliminate the effect of a monochromatic pitch disturbance of known frequency, but of unknown phase and magnitude. An extension of this idea to a stochastic pitch disturbance of known frequency spectra was investigated, and could only be shown to provide significant disturbance cancellation improvement for a higher gain controller than would normally be used. The negative effect of actuator saturation on pitch control performance was shown, supporting the use of a lower "bandwidth" pitch controller when controlling AUV pitch in waves.

6.2 Future Directions

The use of nonlinear sliding control with slender body underwater vehicles has been shown to be effective in practice (Healy and Marco 1992), and is currently being tested for a precursor to the 21UUV (Hills and Yoerger 1994). The work presented here concerning wave effects on an AUV is preliminary in nature, and the problem of AUV control in the presence of wave disturbances begs further study. While a method of calculating the disturbances caused by direct head seas and beam seas was presented, the operation of an AUV in waves of arbitrary aspect is of general interest. Similarly, computer simulations in this paper were limited to the longitudinal plane alone. Full 6 degree of freedom simulations of the 21UUV will be used to investigate the coupling effects of motion in the axes ignored in this paper.

Though simulations can provide preliminary indications concerning the possible performance of an AUV's controller in the presence of waves, these simulations cannot realistically capture the full range of hydrodynamic effects and actuator and sensor performance found in practice. Ultimately, the richest method of studying the effect of wave disturbances on the 21UUV will be the full scale operation of the vehicle beneath the waves.

Bibliography

15th ITTC. Recommendations of the Seakeeping Committee, *Proceedings of the 15th International Towing Tank Conference*, Vol. II, pp. 219-220, 1978.

Berteaux, H. O. *Coastal and Oceanic Buoy Engineering,* published by the author, 1991.

Chryssostomidis, C. and Oakes, M. C. Selection of Wave Spectra for Use in Ship Design, *Proceedings of the International Symposium on Ocean Wave Measurement and Analysis*, Vol. II, pp. 217-234, 1974.

Dean, R. G., and Dalrymple, R. A. *Water Wave Mechanics for Engineers and Scientists,* Prentice Hall, Inc., Englewood Cliffs, NJ, 1984.

Faltinsen, O. M. *Sea Loads on Ships and Offshore Structures*, Cambridge University Press, NY, 1990.

Fossen, T. I. *Guidance and Control of Ocean Vehicles*, John Wiley & Sons, Ltd., NY, 1994.

Healey, A. J., and Marco D. B. Slow Speed Flight Control of Autonomous Underwater Vehicles: Experimental Results with NPS AUV II, *Proceedings of the Second (1991) International Offshore and Polar Engineering Conference*, pp. 523- 532, 1991.

Hills, S. J., and Yoerger, D. R. A Nonlinear Sliding Mode Autopilot for Unmanned Undersea Vehicles, to be published in *Oceans '94 Proceedings*, 1994.

Hoerner, S. F. *Fluid Dynamic Drag*, edited by the author, Midland Park, NJ, 1965.

Hoerner, S. F. *Fluid Dynamic Lift*, edited by the author, Brick Town, N. J. 1975.

MATLAB Users Guide, The MathWorks, Inc., Natick, MA, 1992.

Morison, J. R., O'Brien, M. P., Johnson J. W., and Schaff, S. A. The Force Exerted by Surface Waves on Piles, *Petroleum Transactions, AIME*, Vol. 189, 1950.

Narendra, K. S. and Annaswamy, A. M. *Stable Adaptive Systems,* Prentice Hall, Englewood Cliffs, NJ, 1989.

Newman, J. N. *Marine Hydrodynamics*, MIT Press, Cambridge, MA, 1977.

Papoulis, A. *Probability, Random Variables, and Stochastic Processes*, McGraw-Hill, NY, 1984.

SNAME (1950). The Society of Naval Architects and Marine Engineers. Nomenclature for Treating the Motion of a Submerged Body Through a Fluid, *Technical and Research Bulletin No 1-5.*

Sagatun, S. J., and Fossen, T. I. Lagrangian Formulation of Underwater Vehicles' Dynamics, *Proceedings of the IEEE International Conference on Systems, Man and Cybernetics*, pp. 1029-1034, 1991.

Slotine, J.-J. E, and Coetsee, J. A. Adaptive Sliding Controller Synthesis for Non-linear Systems, *Int. J. Control.*, Vol. 43, No. 6, 1986.

Slotine, J.-J. E., and Li, W. *Applied Nonlinear Control*, Prentice Hall, Englewood Cliffs, NJ, 1991.

St. Denis, M. On Wind Generated Waves, *Topics in Ocean Engineering*, Gulf Publishing Company, Houston, TX, 1969.

Woods, L. C. *The theory of subsonic plane flow*, Cambridge University Press, NY, 1961.

Yoerger, D. R., and Slotine J.-J. E. Robust Trajectory Control of Underwater Vehicles, *IEEE Journal of Oceanic Engineering*, Vol. 10, No. 4, 1985.

Yoerger, D. R., Neuman, J. B., and Slotine, J.-J. E. Supervisory Control Systems for the JASON ROV, *IEEE Journal of Oceanic Engineering*, Vol. 11, No. 3, 1986.

Author's Biographical Note

LCDR Christopher J. Willy, USNR, completed his undergraduate studies at the U. S. Naval Academy, receiving a Bachelor of Science degree in Systems Engineering and a commission in the U. S. Navy in 1981. He finished training as a naval flight officer in 1983, and was first assigned to Patrol Squadron Forty-Nine (VP-49). He has since served at Air Test and Evaluation Squadron One (VX-1), the Reserve Antisubmarine Warfare Training Center, and Patrol Squadron Sixty-Nine (VP-69) prior to his present assignment in the Massachusetts Institute of Technology and Woods Hole Oceanographic Institution Joint Program in Oceanographic Engineering.

LCDR Willy's next assignment is with Patrol Squadron Sixty-Six (VP-66) in Willow Grove, Pennsylvania.

Appendix

Below is contained the derivation of a robust adaptive sliding control law as applied to the 21UUV pitch equation. This derivation is adapted from (Slotine and Li 1991). The resulting control and parameter adaptation laws are presented in section 5.2.1.

$$a_1\ddot{\theta} + a_2 w\dot{\theta} + a_3 u\dot{\theta} + a_4 wu + a_5 \sin\theta + a_6 \cos\theta + d_1(t) = -u^2\delta_s$$

$$s_\theta = \dot{\tilde{\theta}} + \lambda_\theta\tilde{\theta} = \dot{\theta} - \dot{\theta}_r \qquad \dot{\theta}_r = \dot{\theta}_d - \lambda_\theta\tilde{\theta} \qquad \tilde{\theta} = \theta - \theta_d$$

$$s_{\theta\Delta} = s_\theta - \Phi_\theta \,\mathrm{sat}(s_\theta/\Phi_\theta)$$

$$V = \tfrac{1}{2}a_1 s_{\theta\Delta}^2 + \tfrac{1}{2}\tilde{\mathbf{a}}^T\mathbf{\Gamma}^{-1}\tilde{\mathbf{a}} > 0 \qquad a_1 > 0 \qquad \mathbf{\Gamma}^{-1} = \mathbf{\Gamma}^{-T} > \mathbf{0}$$

$$\dot{V} = s_{\theta\Delta}a_1\dot{s}_\theta + \dot{\tilde{\mathbf{a}}}^T\mathbf{\Gamma}^{-1}\tilde{\mathbf{a}} \qquad \tilde{\mathbf{a}} = \hat{\mathbf{a}} - \mathbf{a}$$

$$\dot{V} = s_{\theta\Delta}(-\mathbf{Ya} - d_1(t) - u^2\delta_s) + \dot{\tilde{\mathbf{a}}}^T\mathbf{\Gamma}^{-1}\tilde{\mathbf{a}} \qquad \left|d_1(t)\right|_{\max} < D$$

$$\mathbf{Y} = \begin{bmatrix}\ddot{\theta}_r & w\dot{\theta} & u\dot{\theta} & wu & \sin\theta & \cos\theta\end{bmatrix}$$

$$\mathbf{a} = \begin{bmatrix}a_1 & a_2 & a_3 & a_4 & a_5 & a_6\end{bmatrix}^T$$

$$-u^2\delta_s = \mathbf{Y}\hat{\mathbf{a}} - k_\theta s_\theta \qquad \Rightarrow \qquad \underline{\delta_s = u^{-2}(k_\theta s_\theta - \mathbf{Y}\hat{\mathbf{a}})} \qquad k_\theta > 0$$

$$\dot{V} = s_{\theta\Delta}(\mathbf{Y}\tilde{\mathbf{a}} - d_1(t) - ks_\theta) + \dot{\tilde{\mathbf{a}}}^T\mathbf{\Gamma}^{-1}\tilde{\mathbf{a}} \qquad \dot{\tilde{\mathbf{a}}} = \dot{\hat{\mathbf{a}}}$$

$$\dot{V} = (\dot{\hat{\mathbf{a}}}^T\mathbf{\Gamma}^{-1} + s_{\theta\Delta}\mathbf{Y})\tilde{\mathbf{a}} - s_{\theta\Delta}d_1(t) - s_{\theta\Delta}k_\theta s_\theta \qquad \Rightarrow \qquad \underline{\dot{\hat{\mathbf{a}}} = -\mathbf{\Gamma}\mathbf{Y}^T s_{\theta\Delta}}$$

$$s_{\theta\Delta}k_\theta s_\theta = k_\theta s_{\theta\Delta}^{\;2} + k_\theta\Phi_\theta\left|s_{\theta\Delta}\right|$$

$$\dot{V} = -s_{\theta\Delta}d_1(t) - k_\theta\Phi_\theta\left|s_{\theta\Delta}\right| - k_\theta s_{\theta\Delta}^2$$

$$\underline{k_\theta\Phi_\theta \ge D} \qquad \Rightarrow \qquad \dot{V} < -k_\theta s_{\theta\Delta}^2 < 0$$

It is assumed that w and u are bounded.

$V \geq 0 \qquad \dot{V} < 0 \qquad \Rightarrow \qquad V$ is bounded $\qquad \Rightarrow \qquad s_\theta, \tilde{\mathbf{a}}$ are bounded

s_θ bounded $\quad \Rightarrow \quad \tilde{\theta}, \dot{\tilde{\theta}}$ are bounded, and if $\theta_d, \dot{\theta}_d$ are bounded (assumed) $\Rightarrow \quad \theta, \dot{\theta}$ are bounded

$\tilde{\mathbf{a}}$ bounded $\quad \Rightarrow \quad \hat{\mathbf{a}}$ bounded

for u > 0, δ_s is bounded $\Rightarrow$ $\ddot{\theta}$ is bounded, and if $\ddot{\theta}_d$ is bounded (assumed) $\Rightarrow$ $\dot{s}_\theta$ is bounded

$\Rightarrow$ $\ddot{V}$ is bounded $\Rightarrow$ $\dot{V} \to 0$ by Barbalat's Lemma $\Rightarrow$ $s_{\theta\Delta} \to 0$

DUDLEY KNOX LIBRARY
NAVAL POSTGRADUATE SCHOOL
MONTEREY CA 93943-5101

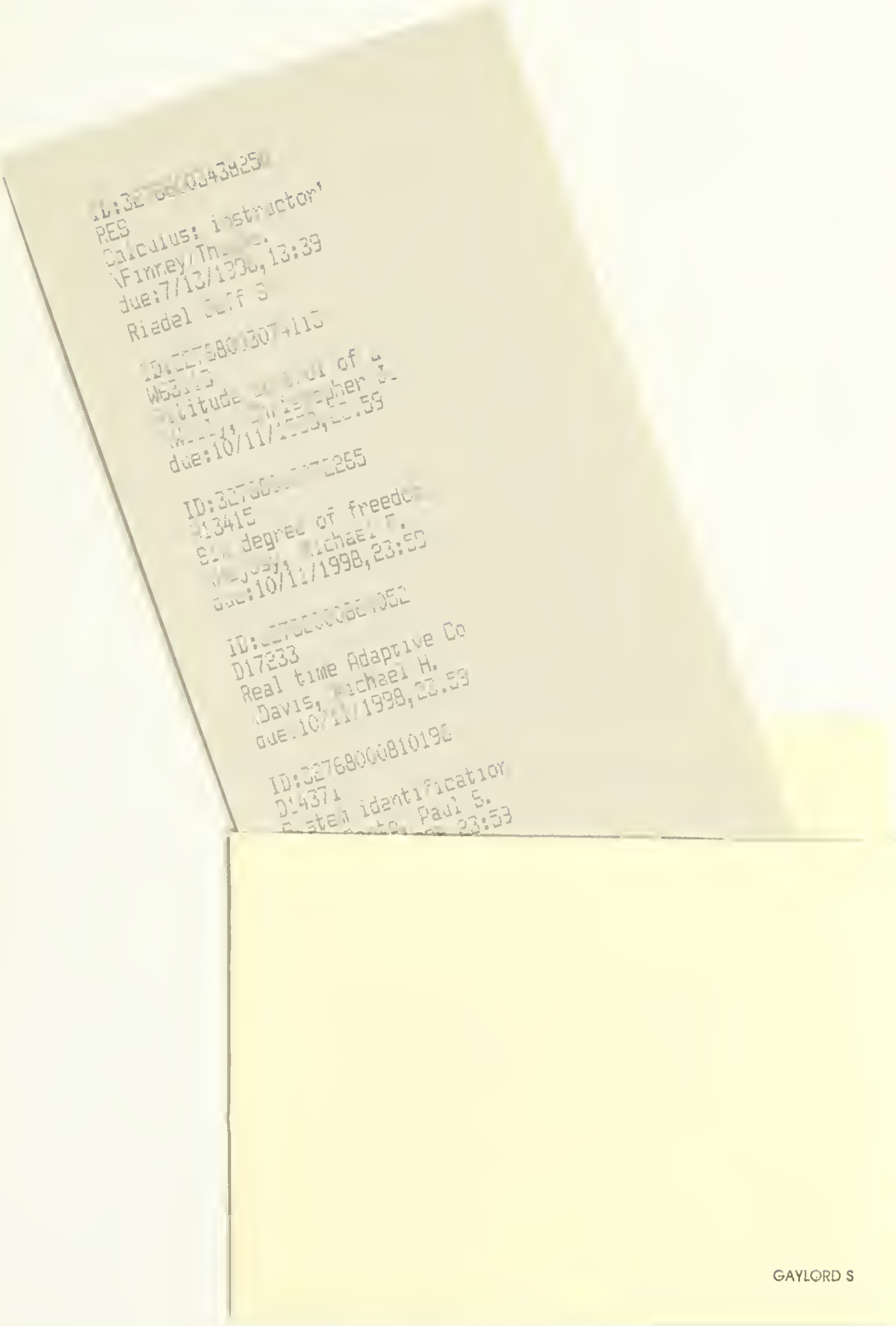

ID:32 [illegible]0343825
RES
Calculus: instructor'
\Finney/Th[illegible]
due:7/13/1998,13:39
Riedel [illegible] S

ID:[illegible]80[illegible]307+113
W63[illegible]
[illegible]titude [illegible] of [illegible]
[illegible]her [illegible]
due:10/11/[illegible],[illegible].59

ID:327[illegible]265
[illegible]13415
S[illegible] degree of freedo[illegible]
[illegible] Michael [illegible].
[illegible]:10/11/1998,23:59

ID:[illegible]052
D17233
Real time Adaptive Co
Davis, Michael H.
due.10/11/1998,23.59

ID:32768000810190
D[illegible]4371
[illegible]stem identification
[illegible] Paul S.
[illegible] 23:59

GAYLORD S

DUDLEY KNOX LIBRARY
3 2768 00307411 3